# ICE FLOW DYNAMICS OF ALASKA GLACIERS

by

Evan Windam Burgess

A dissertation submitted to the faculty of
The University of Utah
in partial fulfillment of the requirements for the degree of

Doctor of Philosophy

Department of Geography

The University of Utah

May 2013

**The University of Utah Graduate School**

## STATEMENT OF DISSERTATION APPROVAL

The dissertation of **Evan Windam Burgess**

has been approved by the following supervisory committee members:

| | | |
|---|---|---|
| **Richard R. Forster** | , Chair | **Feb 8, 2013** Date Approved |
| **Philip E. Dennison** | , Member | **Feb 8, 2013** Date Approved |
| **Kathleen Nicoll** | , Member | **Feb 8, 2013** Date Approved |
| **Ronald L. Bruhn** | , Member | **Mar 5, 2013** Date Approved |
| **Christopher F. Larsen** | , Member | **Feb 8, 2013** Date Approved |

and by **George F. Hepner**, Chair of the Department of **Geography**

and by Donna M. White, Interim Dean of The Graduate School.

# ABSTRACT

Understanding long-term ice dynamic response to climate change remains of the utmost importance with respect to constraining sea level rise (SLR) projections for 2100. SLR contributions from Alaska approximate those from Greenland and may be dominated by mass losses from changes in flow dynamics. But due to a lack of data on flow dynamics, projections for future mass change in Alaska only consider surface mass balance. Here we present the first regionally extensive dataset of mountain glacier flow velocities in Alaska—covering 28,022 $km^2$ of ice. This dataset reveals that more than 50% of the mass flux in Alaska comes from only eleven key glacier systems that have high mass fluxes due to high balance velocities and are not necessarily linked to tidewater glacier retreat. In south central Alaska, we find that the rate of mass loss from tidewater calving is equivalent to 75% of the total net mass loss annually; thus surface mass balance alone is inadequate to project future statewide mass losses. Our dataset also enables a close examination of a surge (periodic acceleration) event on Bering Glacier, the largest surging glacier in the world. There, velocities exceed quiescent speeds by 18 times over two periods lasting a total of 3 years. Results suggest that downstream propagation of the surge is closely linked to the evolution of the driving stress during the surge because driving stress appears to be tied to the spatial variability of resistive stress provided by the bed. Finally, we are able to examine regional changes in wintertime flow

velocities and find that wintertime flow speed is inversely correlated with summertime positive degree days. We propose that this relationship is the result of a negative feedback mechanism whereby increased meltwater production enlarges subglacial conduit systems that are more effective at discharging water from subglacial cavities. As cavities close during the fall, less remaining water reduces bed separation during winter and thus engenders slower sliding velocities. We find this mechanism exerts a secondary control on glacier surge triggering, encouraging/discouraging initiation after cold/warm summers. This mechanism could have important ice dynamic implications when forced by a changing climate. Increases in summertime temperatures could result in a gradual slowing of land terminating ice, thus providing a negative feedback (self correcting) mechanism that could slightly slow projected mass losses from land terminating glaciers.

I would like to dedicate my dissertation to my parents,

who are undoubtedly responsible for my interest in the workings of the world and

for my love of snow and the mountains.

*Thank you Mom and Dad,*

*I would not be here without you.*

TABLE OF CONTENTS

ABSTRACT....iii

LIST OF TABLES....viii

LIST OF FIGURES....ix

ACKNOWLEDGEMENTS....xi

INTRODUCTION....1

References....3

1 FLOW VELOCITIES OF ALASKA GLACIERS....5

1.1 Abstract....5
1.2 Introduction....6
1.3 Results....9
1.4 Discussion....13
1.5 Methods....15
1.6 Acknowledgements....20
1.7 References....29

2 SURGE DYNAMICS ON BERING GLACIER, ALASKA, IN 2008-2011....33

2.1 Abstract....33
2.2 Introduction....34
2.3 Background....37
2.4 Data and Methods....40
2.5 Results....44
2.6 Discussion....53
2.7 Conclusion....58
2.8 Acknowledgements....59
2.9 References....67

3 AN INVERSE RELATIONSHIP BETWEEN SUMMERTIME MELT AND WINTERTIME FLOW VELOCITY ON GLACIERS IN ALASKA.....71

3.1 Abstract.....71
3.2 Introduction.....72
3.3 Methods.....82
3.4 Results.....91
3.5 Discussion.....97
3.6 Conclusion.....102
3.7 Acknowledgements.....103
3.8 References.....123

CONCLUSION.....128

References.....131

LIST OF TABLES


| Table | | Page |
|---|---|---|
| 1.1 | Tidewater flux calculations by region and individual glacier | 22 |
| 2.1 | Statistics describing the 2-D distribution of measured ground displacements in ice-free terrain | 60 |
| 3.1 | Linear models for a PDD winter velocity interaction | 104 |

LIST OF FIGURES


| Figure | | Page |
|---|---|---|
| 1.1 | Glacier velocities in the Wrangell/St. Elias Mountains | 23 |
| 1.2 | Glacier velocities in the Chugach Mountains and Kenai Peninsula | 24 |
| 1.3. | Glacier velocities in the Alaska Range | 25 |
| 1.4 | Glacier velocities in the Tordrillo Range | 26 |
| 1.5 | The dates of all 60 image pairs composing the velocity maps | 27 |
| 1.6 | Estimated uncertainties for all 60 image pairs | 28 |
| 2.1 | Composite velocity map of the BGS and Tana Glacier in Winter 2010 | 61 |
| 2.2 | Bering Glacier System longitudinal velocity profile | 62 |
| 2.3 | High-resolution velocity field during second phase | 63 |
| 2.4 | West Bagley longitudinal velocity profile | 64 |
| 2.5 | Results from airborne altimetry on the BGS profile | 65 |
| 2.6 | Results from airborne altimetry on the BGS profile, cont'd | 66 |
| 3.1 | Study area including189 glacier profiles shown as blue lines | 105 |
| 3.2 | Temporal Distribution of ALOS PALSAR pairs used | 106 |
| 3.3 | Yakutat Climatology | 107 |
| 3.4 | Estimated uncertainty in range and azimuth directions | 108 |
| 3.5 | Comparison of PDD model with in situ observations from meteorological station data at PAYA | 109 |

3.6 Comparison of PDD model with in situ observations from meteorological station data at HDRA2.....110

3.7 Comparison of PDD model with in situ observations from meteorological station data at PAZK.....111

3.8 Comparison of PDD model with in situ observations from meteorological station data at TKLA2.....112

3.9 The standard deviation of velocity from all available winter data.....113

3.10 Rate of change in velocity between observations for hydrologic years.....114

3.11 Velocity anomaly map for the 2007 hydrologic year.....115

3.12 Velocity anomaly map for the 2008 hydrologic year.....116

3.13 Velocity anomaly map for the 2009 hydrologic year.....117

3.14 Velocity anomaly map for the 2010 hydrologic year.....118

3.15 Velocity anomaly map for the 2011 hydrologic year.....119

3.16 Scatterplot of velocity anomalies and PDD anomalies.....120

3.17 Scatterplot of velocity anomalies and PDD anomalies: Surging vs. not surging.....121

3.18 Scatterplot of velocity anomalies and PDD anomalies: Termination Type.....122

# ACKNOWLEDGEMENTS

I would like to thank my advisor Rick Forster for his guidance, expertise and thoughtfulness and for providing me with so many opportunities to grow as an academic and professional. I would like to thank Chris Larsen for his expertise and guidance as well as his kindness in providing me a career path that I am truly thrilled about. I thank Ron Bruhn for countless inquisitive discussions that have opened my mind to concepts beyond my realms. Thanks for the help and ideas from others in my committee, Phil Dennison and Kathleen Nicole. Also, Matthias Braun, Batuhan Osmanoglu, Greg West, Neil Lareau, Simon Brewer, Sebastian Hock, Shad O'Neel, Clement Miege, Leah Campbell, Bob McNabb, Tim Bartholomaus, Michelle Cotton, Rachel Headley, and many others whose expertise and ideas have helped me along the way. I would like to thank my family and friends for their support and company, here in Utah. Finally, for my wife-to-be Annie, who has given me countless ideas and suggestions, and unconditional support along the way.

# INTRODUCTION

Sea-level rise (SLR) is perhaps one of the most important societal and scientific problems facing the world today. Of the new water added to the oceans each year, about half comes from mountain glacier mass losses and half comes from mass losses in Greenland and Antarctica (Meier et al. 2007). The mass budgets of glaciers and ice sheets (and consequently, the rate of new-water sea-level rise) are controlled by two broad processes: surface mass balance (SMB) and ice dynamics. SMB includes the exchange of mass through snow accumulation, surficial melting, deposition and sublimation. Ice dynamics involve the mechanisms that control the rate ice flow, which affects the rate of ice delivery to environments with more SMB mass losses and to ocean/lake margins where ice can be lost to calving. Despite the obvious link between increasing melt rates and a warming climate, it is ice dynamic processes that will likely contribute the most to SLR in the future (Rignot et al. 2011). It is thus problematic that we have a relatively poor understanding of ice dynamics and as a result our largest uncertainties in sea-level rise projections come from unknown ice dynamic responses to climate change (Solomon et al. 2007), in particular for tidewater (ocean calving) glaciers.

Tidewater glaciers originating from ice sheets have been closely monitored for many years (Rignot and Kanagaratnam 2006; Howat, Joughin, and Scambos 2007; Rignot et al. 2011, 2008); this has led to better understanding of tidewater dynamics on the ice sheets

and provided accurate measures of current SLR contributions from ice sheet calving. But mountain tidewater glaciers are not widely monitored like they are for the ice sheets and consequently our future projections for mountain glacier mass loss are based only on SMB losses (Radić and Hock 2011). This presents a problem because our best estimates suggest that roughly 35% of mountain glacier mass loss is coming from tidewater calving of icebergs (Solomon et al. 2007). Thus a large portion of the new-water SLR expected over the next hundred years may come from mountain glacier ice dynamics, a term which is completely unconstrained and unincorporated into projections (Radić and Hock 2011; Solomon et al. 2007)

Alaska glaciers may contribute as much to SLR as the Greenland Ice Sheet and 57% more than the Antarctic Ice Sheet (Wu et al. 2010). Alaska has more tidewater glaciers at lower latitudes than any other region in the world and has already shown some of the most drastic examples of glacier flow acceleration leading to rapid tidewater retreat (Porter 1989; Krimmel 2001; Arendt et al. 2002; O'Neel et al. 2005). Tidewater mass losses from ice dynamics likely exceed 60% of the net mass loss statewide (Larsen et al. 2007; Berthier et al. 2010; Burgess, Forster, and Larsen 2013). Consequently, changes in Alaska ice dynamics must be constrained to reduce uncertainties in SLR projections.

The sliding velocity of a glacier or ice sheet is controlled by the balance of forces between the driving stress (downslope component of gravitational pull) and resistive forces that include frictional shear stress exerted on the glacier bed and sidewalls, and internal stresses within the ice. In most mountain glacier environments shear stress exerted on the glacier bed opposes the majority of the driving stress. But the glacier bed is susceptible to changes in its shear strength due to a variety of mechanisms to be

discussed in later chapters. If shear strength of the bed is reduced, a glacier will accelerate until additional resistive stresses bring the glacier back into force balance at a higher steady-state velocity. Rapid changes in the shear strength of the bed are modulated by the existence of pressurized subglacial water. The work described herein is directed at improving our understanding of the how climate and other factors affect glacier sliding velocity and thus ultimately affect the rate of SLR in a changing climate.

## References

Arendt, A. A., K. A. Echelmeyer, W. D. Harrison, C. S. Lingle, and V. B. Valentine. 2002. Rapid wastage of Alaska glaciers and their contribution to rising sea level. *Science* 297 (5580):382–386.

Berthier, E., E. Schiefer, G. K. C. Clarke, B. Menounos, and F. Rémy. 2010. Contribution of Alaskan glaciers to sea-level rise derived from satellite imagery. *Nature Geoscience* 3 (2):92–95.

Burgess, E. W., R. R. Forster, and C. F. Larsen. 2013. Flow velocities of Alaska glaciers. *Nature Communications*.

Howat, I. M., I. Joughin, and T. A. Scambos. 2007. Rapid Changes in Ice Discharge from Greenland Outlet Glaciers. *Science* 315 (5818):1559–1561.

Krimmel, R. M. 2001. *Photogrammetric data set, 1957-2000, and bathymetric measurements for Columbia Glacier, Alaska*. Tacoma, Wash.: U.S. Geological Survey ;

Larsen, Christopher F., R. J. Motyka, A. A. Arendt, K. A. Echelmeyer, and P. E. Geissler. 2007. Glacier changes in southeast Alaska and northwest British Columbia and contribution to sea level rise. *Journal of Geophysical Research: Earth Surface* 112 (F1).

Meier, M. F., M. B. Dyurgerov, U. K. Rick, Shad O'Neel, W. Tad Pfeffer, R. S. Anderson, S. P. Anderson, and A. F. Glazovsky. 2007. Glaciers dominate eustatic sea-level rise in the 21st century. *Science* 317 (5841):1064–1067.

O'Neel, S., W.T. Pfeffer, R. Krimmel, and M. Meier. 2005. Evolving force balance at Columbia Glacier, Alaska, during its rapid retreat. *Journal of Geophysical Research F: Earth Surface* 110 (3).

Porter, S. C. 1989. Late Holocene Fluctuations of the Fiord Glacier System in Icy Bay, Alaska, U.S.A. *Arctic and Alpine Research* 21 (4):364–379.

Radić, V., and R. Hock. 2011. Regionally differentiated contribution of mountain glaciers and ice caps to future sea-level rise. *Nature Geoscience* 4 (2):91–94.

Rignot, E., J. E. Box, E. Burgess, and E. Hanna. 2008. Mass balance of the Greenland ice sheet from 1958 to 2007. *Geophysical Research Letters* 35 (20).

Rignot, E., and P. Kanagaratnam. 2006. Changes in the velocity structure of the Greenland Ice Sheet. *Science* 311 (5763):986–990.

Rignot, E., I. Velicogna, M. R. Van Den Broeke, A. Monaghan, and J. Lenaerts. 2011. Acceleration of the contribution of the Greenland and Antarctic ice sheets to sea level rise. *Geophysical Research Letters* 38 (5).

Solomon, S., D. Qin, M. Manning, Z. Chen, M. Marquis, K. B. Averyt, M. Tignor, and H. L. Miller. 2007. *Contribution of Working Group I to the Fourth Assessment Report of the Intergovernmental Panel on Climate Change*. Cambridge: Cambridge University Press.

Wu, X., M. B. Heflin, H. Schotman, B. L. A. Vermeersen, D. Dong, R. S. Gross, E. R. Ivins, A. W. Moore, and S. E. Owen. 2010. Simultaneous estimation of global present-day water transport and glacial isostatic adjustment. *Nature Geoscience* 3 (9):642–646.

# CHAPTER 1

# FLOW VELOCITIES OF ALASKA GLACIERS

## 1.1 Abstract

Our poor understanding of tidewater glacier dynamics remains the primary source of uncertainty in sea level rise projections. On the ice sheets, mass lost from tidewater calving exceeds the amount lost from melting. In Alaska, the magnitude of calving mass loss remains unconstrained, yet immense calving losses have been observed. With 20% of the global new-water SLR coming from Alaska, constraints on dynamic mass loss in Alaska are needed to improve SLR projections. Here we present the first regionally comprehensive map of glacier flow velocities in Central Alaska. These data reveal that the majority of the regional downstream mass flux is constrained to only a few coastal glaciers. We find regional calving losses are 17.1 Gt $a^{-1}$ or approximately, 35% of the net mass loss throughout Central Alaska. Thus, a large proportion of Alaska's SLR contribution is coming from tidewater dynamic processes that are unconstrained over the next century.

## 1.2 Introduction

Mountain glaciers are significant contributors to current and future sea level rise (SLR). Worldwide, mountain glaciers contribute to about half of the new-water SLR from land ice[1]; but the proportion of mass lost due to changing ice flow dynamics is unknown and likely large[1]. In southeastern Alaska and northwest British Columbia, up to 66% of the mass loss may be a consequence of accelerating ice flow and resultant calving into tidewater or lake environments[2]. Immense lake and tidewater dynamic mass losses[2–5] have been observed elsewhere in Alaska as well. Such mass losses are a consequence of a positive feedback mechanism that accelerates ice flow and calving rate[6]. This feedback is typically triggered through a reduction in resistive back stress that can come from submarine melting[7,8], changes in front position[9,10], and/or a reduction in ice front mélange concentration[11]. These mechanisms can often lead to seasonal oscillations in iceberg calving with peak calving rates in spring and early summer[7,11]. In mountain glacier environments, errors in surface mass balance (SMB) projections are constrained using physically grounded models[12]. But projections of total mass loss from mountain glaciers are forced to use simple linear extrapolations[1] largely because the proportion of tidewater dynamic mass loss is still not known. Thus direct estimates of regional mountain glacier calving loss are needed to parse total mass loss and uncertainty sources in mountain glacier environments.

Ice dynamics may also affect mass balance on land terminating glaciers[13]. Meltwater induced basal lubrication can cause brief acceleration, particularly in spring[14–16]. Warmer summers have also been shown to cause slower flow in late summer[17]. But these dynamics are poorly understood; in particular, we lack understanding of how the

responsible mechanisms may evolve in a changing climate. In western Greenland and in some mountain glacier areas[18,19], flow velocities have slowed over long periods but elsewhere changes are not known due to a lack of velocity data.

Ice dynamics on surge-type glaciers also likely have an impact on mass balance, though these links are poorly understood. Surge-type glaciers undergo periodic accelerations of 10-100 times normal velocities[20,21]; this dynamic redistributes mass to lower elevations and thus increases SMB mass losses. Surging can also increase ablation rates by exposing greater surface area through crevassing[22]. Given that surge-type glaciers never flow in equilibrium with climate[21], their dynamic response to climate change and mass loss will likely be different from responses from other glaciers. Alaska has the highest concentration of surge-type glaciers in the world[23] and while the surge cycle has been studied thoroughly on a few glaciers[20,21,24,25], nearly 200 surge-type glaciers in Alaska are devoid of observation[23]. Therefore, regional observations of velocities on surge-type glaciers, both during surge and quiescent (slow) phases are needed to address regional dynamics on these unique systems. Surging and tidewater related mass loss also has important tectonic implications in the St. Elias Mountains by affecting fault stability in areas capable of generating large magnitude earthquakes[26,27].

Mapping mountain glacier velocities on regional scales has different impediments than doing so on the ice sheets. Mountain glaciers are often in extremely cloudy, wet and maritime environments that conceal the glacier surface from optical satellites and change surface conditions rapidly. Southern Alaska typifies this environment with up to 5 m.w.e. of snowfall and 12 m.w.e. of melt annually[28]. In these environments, synthetic aperture radar (SAR) satellite platforms have distinct advantages and disadvantages over optical

sensors. SAR penetrates cloud cover and is able to track velocities in featureless accumulation zones. But SAR is sensitive to water, thus rain and summertime melt will confound results. On the ice sheets, velocity mapping has largely been completed using SAR interferometry but this method is extremely vulnerable to changing surface conditions. Therefore, we use a more robust method—offset tracking, which uses two images acquired at different times to find the horizontal displacement of pixel patterns using cross correlation[29–31]. Offset tracking is effective using both optical and SAR platforms and has produced velocity results in many mountain glacier regions[32–35], including Alaska[19]. But assessing ice dynamic SLR contribution from mountain glaciers requires more comprehensive studies.

We expand upon this work spatially and target areas that are likely to have large mass losses due to ice dynamics. We tested a full suite of SAR platforms that include a variety of wavelengths, orbit repeats, resolutions and polarizations, which greatly affect the quality of results. We processed 344 SAR image pairs and selected the best data, which were acquired between 2007 and 2010, to produce mosaicked velocity maps. See Methods section for specifics.

The velocity map includes flow velocity data at or near 20 tidewater and 16 lacustrine glacier termini, thus enabling a regional estimate of calving flux. We establish flux gates as close to termini as possible, and integrate flow across each gate. We estimate volumetric flux using a crude thickness estimate based on a simple relationship between glacier length and thickness[36] (see Methods). While this method is simplified, more sophisticated methods still contain large biases compared to volume/area scaling in

Alaska[37] and are otherwise not validated. Limited opportunities to validate our thickness estimates are available on a few glaciers (see Methods).

## 1.3 Results

Surface velocities are available for 28,022 $km^2$, which includes almost all major glaciers in Alaska west of 138° W; expanding these data east will follow in later papers. Our uncertainties are quantified using a robust equivalent to a 1-sigma uncertainty and are 0.02 m $d^{-1}$ (see Methods section). We derive mosaicked velocity maps for the Wrangell-St.Elias Mountains (Fig. 1.1), the Chugach Mountains/Kenai Peninsula (Fig. 1.2), the Alaska Range (Fig. 1.3), and the Tordrillo Range (Fig. 1.4). These maps resolve mean velocities over 46-day orbit intervals. Of the 60 pairs used for the map, 56 were acquired in January and February (Fig. 1.5). Though annual average velocities would be ideal, shorter repeats allow for less de-correlation and are necessary for the spatial coverage we have achieved. Nonetheless, wintertime velocities can still be considered representative of mean annual velocities because faster flow in spring is typically offset by slower flow in fall[17]. Wintertime velocities are also the most constant[38] and thus the most likely to provide consistency in observations. Still, many glaciers underwent significant inter-annual velocity variability over the observation interval and only one velocity snapshot is included in this map (Figs. 1.1, 1.2, 1.3, 1.4).

### 1.3.1 Spatial Structure of Velocity

The regional spatial structure of flow velocity conforms to our understanding of glacier balance velocities (a flow speed that compensates for accumulated mass

upstream) and surge dynamics. Flow velocities generally increase from continental climes towards the maritime coast. In particular, there are twelve glacier systems that have exceptionally high velocities (>1 m $d^{-1}$) over much of their length. The fast velocities are not necessarily linked to tidewater dynamics—these twelve glaciers include land-terminating glaciers in addition to calving glaciers in retreat and advance: Hubbard, Seward, Agassiz, Yahtse, Guyot, Tsaa, Stellar, Bering, Columbia, Harvard, Yale, and Knik Glaciers. Rather, these twelve glaciers all have high elevation, coastal accumulation zones and are consequently positioned to receive the highest specific mass balances throughout Alaska. Thus, these glaciers would require large fluxes to balance accumulation.

We provide a crude estimate of total downstream ice flux by spatially integrating the velocity field within individual glacier basins to obtain a total surface area flux per glacier (units: $km^2$ m $d^{-1}$). This analysis is not a volumetric flux and does not account for missing data. Nonetheless, we find that Seward, Bering, Hubbard, Yahtse, Guyot, and Tsaa Glaciers account for ~50% of the total flux throughout the dataset. If data coverage were better, we expect Columbia, Harvard, Yale and Knik would take on similar importance (our patchy results indicate high velocities on these glaciers as well).

### 1.3.2 Surge Type Glaciers

The velocity maps also include flow speeds on more surge-type glaciers than ever compiled previously. During the observation period (2007-2011), temporal velocity variability was observed on many surge-type glaciers. However, out of 22 large surge-type glaciers, surges (defined as variations in velocity >10x observed slow values) were

only observed on Bering, Lowell, and Ottawa (Fig. 1.1); and only Bering is in surge phase in the maps presented (due to data availability). Given that surge intervals in Alaska are between 18 to 75 years[25,39], we would expect to see somewhere between 11 to 3 surges for maritime and continental climates, respectively. Given that most of the surge type glaciers are in continental climates, long term regional mean fluxes from surge-type glaciers are likely underestimated in this map, but not massively.

Flow speeds of surge type glaciers[23] in quiescence are almost always flowing slower than neighboring glaciers that are not surge-type. Most surge-type glaciers have expansive areas of stagnant ice at their termini and higher velocities upstream. Mapped data on Tweedsmuir Glacier (Fig. 1.1) immediately follows a surge ending in 2009; these data show stagnant ice throughout the glacier length. These configurations conform well to observations and model results on Variegated Glacier[24,40], suggesting that most surge-type glaciers are undergoing similar quiescent phase evolutions.

There are, however, a few notable exceptions (Fig. 1.1). Quiescent phase velocities on Seward Glacier exceed 5 m $d^{-1}$, which are, by far, the highest land-terminating flow speeds in the dataset. How Seward Glacier is able to maintain these velocities during quiescence may be due to its bi-modal elevation distribution. Donjek Glacier (surge-type) also has exceptionally high velocities when compared to neighboring systems in quiescence. Lowell Glacier surged in 2010; a year prior, ice velocities were relatively high near the terminus and slower upstream as shown in Figure 1.1.

1.3.3 Calving Flux

Our calving flux estimates assume a glacier mean thickness at each flux gate and a surface velocity representative of the vertically integrated flow velocity (this assumption is observed on Columbia Glacier[41]). From 20 tidewater and 16 lacustrine calving glaciers in the study area (Table S1) we obtain a total calving loss of ~9.1 Gt $a^{-1}$. This number does not include Columbia Glacier (moving too fast for our methods). If calving losses from Columbia are included[42], we find the regional calving loss to be 17.1 Gt $a^{-1}$ or 35% of the net mass loss throughout the Wrangell/St. Elias, Chugach, Kenai, Tordrillo, and Alaska Ranges (as determined from GRACE observations[43]).

1.3.4 Efficacy of SAR Offset Tracking in Alaska

The only SAR platforms with extensive geographical/temporal coverage are ALOS PALSAR, RADARSAT and ERS-1/2. Of these, only ALOS (L-Band) is robust in Alaska's maritime environment and effective in featureless accumulation zones. Given the harshness of Alaska's environment, it is likely that results of similar/improved quality can be obtained on mountain glaciers worldwide. However, none of these platforms are effective in summer because of surficial melting; none are effective at coastal low elevations due to rain; and none are effective on fast moving ice because of long-repeat times. These limitations are problematic as it is these areas that are experiencing the most rapid changes in flow velocities, typically related to tidewater dynamics. Short-repeat platforms, including TerraSAR-X and ERS Tandem/Ice Phase were found to be effective in these environments despite having shorter wavelengths that are more sensitive to water. But data acquired by these platforms are geographically/temporally limited and

have lower precision because of a necessary shorter acquisition interval. Thus, we find that the planned NASA mission DESDnyI-R, with a 12 to 16- day repeat L-Band SAR would resolve the majority of our deficiencies and would enable tracking in almost all mountain glacier environments including tidewater termini where velocities are most important to SLR contributions.

## 1.4 Discussion

The dataset presented represents the first regional map of mountain glacier flow speeds in Alaska. The velocity magnitude data will be available for public download at the Alaska Satellite Facility (http://www.asf.alaska.edu/). These maps provide wintertime flow speeds on almost every major glacier system in the Wrangell/St. Elias, Chugach, Kenai Peninsula, Alaska and Tordrillo Ranges. However, we emphasize caution when using this map to look at trends in velocity through time because inter-annual changes in velocity were found to be common throughout the image pairs processed. This variability will be discussed in a later paper.

The results presented here are critical because they enable us to place focused studies of dynamics in the broader context of 25,000+ glaciers in Alaska[44]. Many surging glaciers in the dataset appear to be undergoing similar quiescent phase velocity evolutions as observed more closely on Variegated Glacier. Other surge-type glaciers appear to be exhibiting other unresolved dynamics. Columbia contributes to 51% of the total calving flux throughout the region. Generally, flow velocities on the southern coast are far higher than areas inland.

We find that the ice flux from the twelve fast flowing glaciers mentioned, is immense with respect to Alaska as a whole. Given that these glaciers are likely thicker than others (they are significantly larger in area than the average), it is likely that these twelve glaciers account for far more than half of the volumetric flux throughout Alaska. In other glaciated regions, anomalously large fluxes are typically the result of lake/tidewater retreat[45]. But in Alaska, extremely large gradients in snow accumulation rates force anomalously high balance velocities on glaciers with high elevation coastal accumulation zones, which happens to include surging glaciers, land-terminating glaciers and lake/tidewater glaciers in retreat and advance. This does not imply that the largest mass losses are coming from these glaciers, but we suggest that dynamics on these rapid-flow systems may operate differently than other glaciers, because they are able to maintain higher flow speeds and higher driving stresses without losing mass. Understanding the dynamics of these twelve glacier systems is critical for future efforts to estimate dynamic mass loss in Alaska.

The key finding from this work is that calving contributes ~17.1 Gt $a^{-1}$ or 35% of the net mass loss throughout the Wrangell/St. Elias, Chugach, Kenai, Tordrillo, and Alaska Ranges. 15.8 Gt $a^{-1}$ of this calving flux comes from tidewater calving alone. This number is quite extraordinary given that tidewater glaciers included in this estimate account for only 13%[44] of glacier area within the region examined. In addition, our data were acquired in winter, thus annual mean fluxes could be higher due to seasonal speedup[11]. Given that lake and tidewater calving losses in Southeast Alaska are likely of comparable importance[2], we find that a large percentage of Alaska's current mass loss is coming from tidewater calving. Given that Alaska is contributing 20% of the current

SLR[1], calving represents a large SLR component that has few constraints on its evolution in a changing climate. Thus, it is of critical importance to reconsider how well Alaska mass loss is constrained. In particular, it will be necessary to estimate the total potential tidewater dynamic contribution from Alaska. Without this knowledge, the rate of future mass loss in Alaska—a considerable SLR contributor—will remain unconstrained.

## 1.5 Methods

Glacier surface velocities are derived using SAR offset tracking [29,31] with ALOS PALSAR Fine-Beam data (L-Band, HH Polarization, 46-day repeat). Repeat image pairs, acquired within one to two orbit intervals, are used to derive displacements. Raw (L0) data is processed to single-look complex (SLC) images using GAMMA® software. Ground offsets are calculated from the slant-range SLCs using intensity cross-correlation optimization offset tracking[30]. SLCs are oversampled by a factor of two and all offsets with signal-to-noise ratios[30] below 5.0 are eliminated. A broad range of window sizes was tested; the chosen window size was 45 x 90 pixels (nominally, 337 m x 283 m). Wider windows tend to obtain more results, but are too large for use on small glaciers. Offsets are calculated at intervals of 20 x 40 pixels.

Once offsets are calculated, they are geocoded, topographically corrected, and corrected for image co-registration. These procedures require an elevation model. We choose the ASTER-GDEM 2.0[46] because it extends throughout Alaska and is derived from comparatively recent data (1999 – 2011). Other elevation models are either dated (NED-DEM), limited to south of 60° latitude (SRTM-DEM), or unavailable at reasonable cost (SPOT-DEM). The ASTER-GDEM does have significant problems with artifacts

and abrupt changes in elevation due to image saturation and changing surface heights over time; implications of these artifacts are discussed below.

Offsets are geocoded using the GDEM and satellite geometry. Any offset estimate located on a DEM artifact will inherit a small error in that offset's geo-location. Given that artifacts are relatively sparse and the final gridded dataset is a smoothed interpolation from many offset estimates, the artifacts have little or no effect on the final map.

Topographic correction is performed using concepts of radargrammetry[47], where the corrected range offset,

$$O_{corr} = O_{rng} - h \cdot (\cot\theta_{slav} - \cot\theta_{mast}), \qquad (1.1)$$

is a function of the measured offset, the elevation (obtained from the ASTER-GDEM), and the slave and master look angles. This approach is insensitive to errors in the GDEM; an error in the GDEM of 100 m, typically results in a range displacement error of $<$ 0.005 m $d^{-1}$. We correct for image co-registration by using the Randolph Glacier Inventory (RGI1.0)[44] and ASTER-GDEM to identify offsets that exist on stable ground (off-glacier and above 0 m elevation). The stable ground offsets are modeled using a second-order polynomial function fit using an iterative least squares method. Residuals from each iterative fit are used to identify and eliminate outlying offsets and sequentially improve the model. Threshold residuals for exclusion from the fit are 3, 2.5 and 2 sigma values. The final polynomial is subtracted from all offsets to provide ice displacements on glaciers and uncertainty estimates off glacier.

Offset tracking creates many erroneous offset vectors, which are eliminated using a highly effective culling routine[48]. The routine filters vectors by comparing their orientation and magnitude to neighboring vectors; it removes better than >99% of

erroneous vectors and removes <0.1% false negatives. Each scene is also manually inspected for other problems, including removing any remaining offset vectors that aren't pointing in the direction of flow or are anomalously high/low.

A total of 624 frames are processed into 344 image pairs that encompass the Wrangell-St. Elias Mountains, the Chugach, Kenai Peninsula, Alaska Range and Tordrillo Range. Then, custom software is used to manually identify which frames can best represent each glacier and then mosaic chosen offset vector fields from multiple frames.

Temporal changes in flow velocity complicate the mosaicking process. The primary protocols for mosaicking include: 1) avoid breaking up a glacier system between two different acquisition time periods to assure continuity for each glacier basin, for example, joining frames along ice divides or ridges rather than across a glacier. 2) If protocol 1 is not possible given available data, frames are chosen that have the most comparable velocities at the seam. Overall, continuity within each glacier basin is prioritized above optimal spatial coverage. In total, 60 frames were chosen to produce the final maps. The dates of these image pairs are shown in Figure 1.3.

The mosaicked vector field for each mountain range is interpolated onto 90m UTM grids using a second order polynomial regression with a search radius of 900 m. A minimum of 6 values must exist within at least 4 of 8 radial sectors surrounding a grid point to obtain an interpolated value. This method is effective at smoothing out minute differences in neighboring vectors. Since the mosaic contains data from different dates, and processing configurations, the pedigree of each individual vector is stored and interpolated onto the same UTM grid using nearest neighbor interpolation.

### 1.5.1 Uncertainty Estimation

We provide an estimate of uncertainty by examining the distribution of offset vectors obtained on stable ground (off-glacier). Stable ground offset vectors are obtained by masking each offset field with the RGI1.0[44] dataset and the ASTER GDEM 2.0[46] (eliminating ocean). Calculated offsets on stable ground have nonzero magnitudes due to erroneous correlation matches, errors in image co-registration and ambiguities in the location of the correlation peak. Erroneous correlation matches give the stable ground offset fields a non-normal distribution (extremely large tails). Thus we describe their distribution using robust, nonparametric statistics including median and normalized median absolute deviation (MADn, robust equivalent to standard deviation)[49].

Estimated uncertainties for each image pair are displayed in Figure 1.6. Median values of off-glacier vectors (representing overall directional bias) are $<0.003$ m $d^{-1}$. Overall, the MADn values of off-glacier vectors averages 0.02 m $d^{-1}$ in range and azimuth directions; in all cases the MADn is $<0.06$ m $d^{-1}$.

### 1.5.2 Tidewater Calving Fluxes

Tidewater calving fluxes are estimated by evaluating the perpendicular component of surface velocity across flux gates. Established flux gates are stationary, thus we do not take into account retreating/advancing termini. Any missing data along the flux gate is interpolated using a spline interpolation that forces the velocity to zero at the glacier edge. Flow velocity perpendicular to the gate is integrated over the glacier width, yielding an areal surface flux (Table 1.1).

While effort was made to establish gates as close to termini as possible, our lack of data near some tidewater termini forces gates well upstream. Our methods do not correct for any difference in flux between the gate and the terminus; therefore any mass lost between the flux gate and the terminus through surface mass balance will result in an overestimation of calving flux. The median distance from each terminus to gate is 1.5 km. This is, on average, about 11% up the total glacier length (Table 1.1). The mean gate elevation is 410 m. This is considerably lower than typical coastal Alaska equilibrium lines, which are at around ~1000 m.

Thickness observations are unavailable at the flux gates in this study, thus we obtain a rough thickness estimate using a well-established[36] square-root relationship between glacier length ($L$) and mean thickness ($H_m$),

$$H_m = \alpha_m \sqrt{L}\,, \qquad \text{(S1)}$$

where $\alpha_m$ is a constant we will assign a value of 2 (following ref 35). Given that our flux gates are roughly halfway between the equilibrium line and the terminus, we suggest that this mean glacier thickness is a reasonable value to use at each flux gate. But given the uncertainties in ice thickness and uncertainties in basal motion, we derive a best and lowball volumetric flux estimate (Supplementary Table S1). Our best estimate assumes the mean glacier thickness from equation S1 at the flux gate and assumes the vertically integrated flow velocity is equivalent to the surface velocity (basal sliding usually dominates ice motion near tidewater termini as observed on Columbia Glacier[41]). Our lowball estimate assumes half of the mean glacier thickness at the flux gate and a vertically integrated flow velocity equivalent to 80% of the surface velocity (this is assuming perfect plasticity and no basal sliding[50]). There are limited opportunities to

validate this method. Thickness observations from airborne low-frequency radar surveys on Seward and Bering Glaciers[51] conform well to mean thicknesses of 690 and 800 m derived from the method used here. However, mean thickness on Columbia Glacier[41] (determined from continuity modeling) is far lower than the mean thickness estimated by methods described here (145 m and 440 m, respectively). The Columbia is in a unique and rapid retreat, having lost 50% of its volume in 50 years[41]; thus it may not be a representative case. Nonetheless this highlights the large uncertainties in glacier thickness estimates in Alaska.

In total, we estimate calving fluxes from the 20 tidewater and 16 lacustrine glaciers in Supplementary Table S1 to be 9.1 Gt $a^{-1}$ and not lower than 3.7 Gt $a^{-1}$. This estimate does not include ten small tidewater glaciers and many small lacustrine glaciers within the study area. There are 18 tidewater glaciers in Southeast Alaska as well as many lacustrine glaciers that are also unaccounted for in this study. Columbia glacier is also not included, which had calving losses of about 8 Gt $a^{-1}$ over a similar period of study[42]. Still, the total calving loss represents ~35% of the total net mass loss throughout the Kenai, Chugach, and Wrangell/St. Elias regions as determined by the Gravity Recovery and Climate Experiment satellite.[43]

## 1.6 Acknowledgements

Thanks to Batuhan Osmanoglu, Matthias Braun for their insightful ideas and discussion. E. Burgess was funded under the NASA Earth Science Space Fellowship. R. Forster and the velocity work were funded by NASA Grants NNX08AP27G and

NNX08AX88G. C. Larsen was supported by NASA's Operation Ice Bridge Grant NNH09ZDA001N. The Alaska Satellite Facility provided ALOS and ERS data.

Table 1.1: Tidewater flux calculations by region and individual glacier.

| Tidewater Glaciers | | Length km | Thickness m | Gate dist. from terminus km | Gate elev. m | Surface flux $km^2$ / yr | Volumetric flux $km^3$ / yr * best | low |
|---|---|---|---|---|---|---|---|---|
| **Kenai** | Aialik | 15.1 | 245 | 4.8 | 938 | 1.34 | 0.33 | 0.13 |
| | Blackstone | 10.1 | 200 | 1.1 | 423 | 0.46 | 0.09 | 0.04 |
| | Chenega | 24.6 | 313 | 1.7 | 335 | 1.29 | 0.41 | 0.16 |
| | McCarty | 17.5 | 264 | 2.3 | 395 | 0.49 | 0.13 | 0.05 |
| | Nellie Juan | 14.1 | 237 | 2.1 | 329 | 0.34 | 0.08 | 0.03 |
| | Northwestern | 6.9 | 166 | 2.9 | 905 | 0.42 | 0.07 | 0.03 |
| | Tiger | 10 | 199 | 3.9 | 707 | 0.44 | 0.09 | 0.03 |
| **Chugach** | Barry | 24.5 | 313 | 5.5 | 494 | 0.57 | 0.18 | 0.07 |
| | Harriman | 12.5 | 223 | 0.6 | 149 | 0.18 | 0.04 | 0.02 |
| | Harvard | 38.4 | 392 | 1.9 | 167 | 1.37 | 0.54 | 0.22 |
| | Surprise | 15.6 | 250 | 1.3 | 264 | 0.39 | 0.1 | 0.04 |
| | Yale | 31.5 | 355 | 1.9 | 556 | 0.82 | 0.29 | 0.12 |
| **St. Elias** | Guyot | 23.7 | 307 | 7.8 | 1027 | 4.22 | 1.3 | 0.52 |
| | Tsaa | 22.8 | 301 | 4.2 | 703 | 2.76 | 0.83 | 0.33 |
| | Turner | 29.5 | 343 | 1.4 | 205 | 0.15 | 0.05 | 0.02 |
| | Tyndall | 21.6 | 293 | 3.9 | 578 | 0.42 | 0.12 | 0.05 |
| | Grotto | 7.7 | 175 | 1.7 | 287 | 0.25 | 0.04 | 0.02 |
| Hubbard w/o Valerie | | 123.3 | 702 | 26.2 | 1115 | 3.52 | 2.48 | 0.99 |
| | Valerie | 41.6 | 407 | 6.5 | 281 | 0.54 | 0.22 | 0.09 |
| | Yahtse | 61.1 | 494 | 6.6 | 799 | 2.23 | 1.1 | 0.44 |
| | | | | **Tidewater Totals*** | | **22.2** | **8.5** | **3.4** |
| **Lacustrine Glaciers** | | | | | | | | |
| **Kenai** | Bear | 29.0 | 340 | 1.4 | 59 | 0.26 | 0.09 | 0.03 |
| | Excelsior | 19.0 | 275 | 1.5 | 276 | 0.12 | 0.03 | 0.01 |
| | Ellsworth | 22.7 | 301 | 0.6 | 38 | 0.11 | 0.03 | 0.01 |
| **Chugach** | Allen | 28.7 | 338 | 1.0 | 142 | 0.08 | 0.03 | 0.01 |
| | Childs | 18.1 | 269 | 0.4 | 139 | 0.30 | 0.08 | 0.03 |
| | Colony | 26.1 | 322 | 1.2 | 167 | 1.01 | 0.33 | 0.13 |
| | Lake George | 21.3 | 292 | 0.9 | 162 | 0.06 | 0.02 | 0.01 |
| | Schwan | 23.7 | 307 | 0.5 | 124 | 0.03 | 0.01 | 0.00 |
| | Sheridan | 24.6 | 313 | 0.5 | 45 | 0.22 | 0.07 | 0.03 |
| | Shoup | 25.6 | 320 | 3.2 | 430 | 0.14 | 0.05 | 0.02 |
| | Woodworth | 24.1 | 310 | 0.3 | 223 | 0.02 | 0.00 | 0.00 |
| | Valdez | 31.9 | 357 | 0.1 | 65 | 0.03 | 0.01 | 0.00 |
| **St. Elias** | Lowell | 59.5 | 487 | 0.2 | 553 | 0.28 | 0.14 | 0.06 |
| | Miles | 53.6 | 462 | 0.6 | 133 | 0.47 | 0.22 | 0.09 |
| | Russell | 30.3 | 348 | 0.5 | 1392 | 0.18 | 0.06 | 0.02 |
| | Stellar | 58.36 | 483 | 0.8 | 181 | 0.62 | 0.30 | 0.12 |
| | | | | **Lacustrine Totals*** | | **3.9** | **1.5** | **0.6** |
| | | | | **Total Calving Flux*** | | **26.1** | **10.0** | **4.0** |
| | | | | **Water Volume Gt / yr **** | | | | |
| | | | | **Tidewater Totals** | | **20.4** | **7.8** | **3.1** |
| | | | | **Lacustrine Totals** | | **3.6** | **1.3** | **0.5** |
| | | | | **Total Calving Flux** | | **24.0** | **9.1** | **3.7** |

** Expressed as ice volume*

*** Assuming an ice density of 917 kg $m^3$*

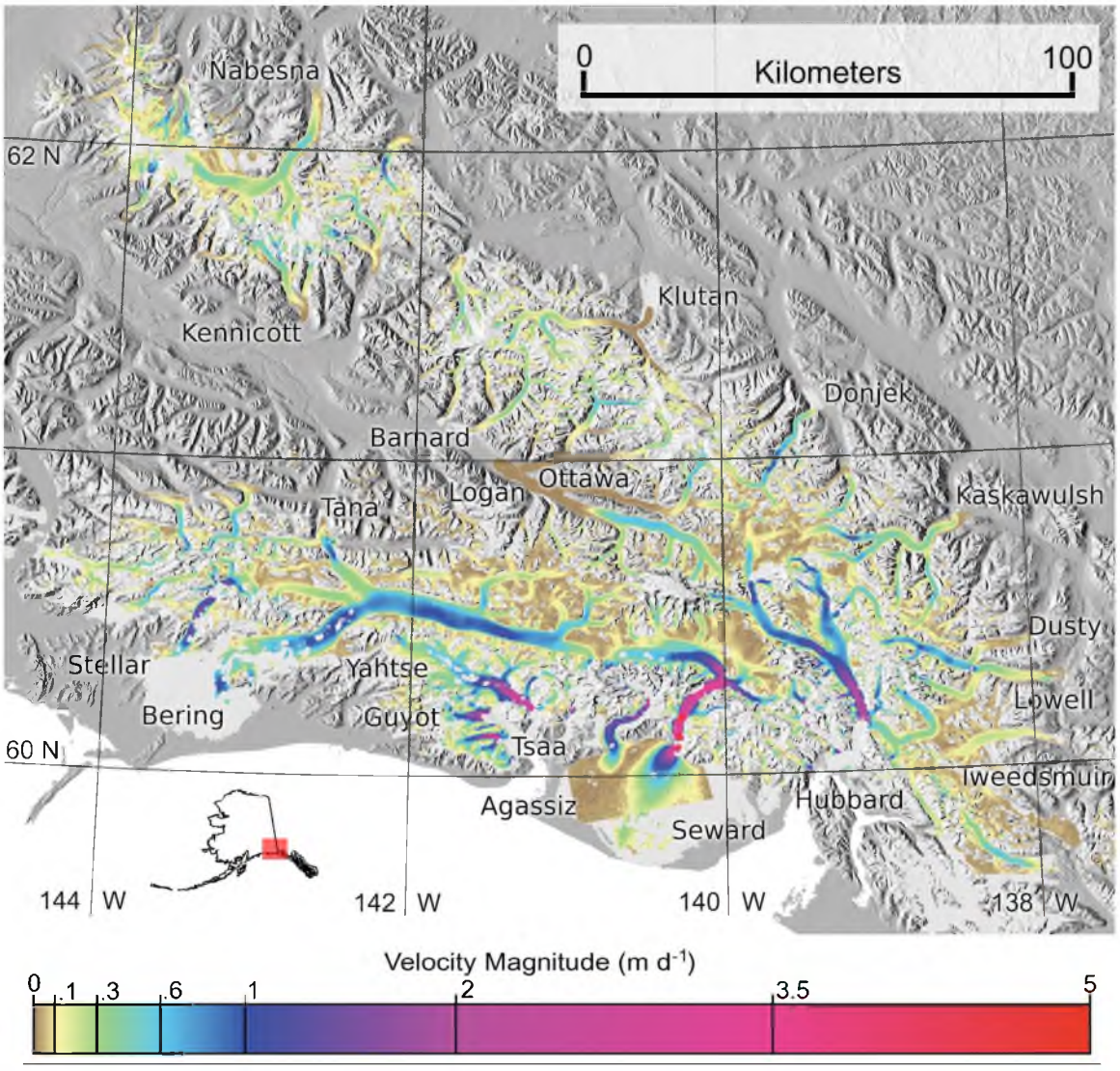


Figure 1.1. Glacier velocities in the Wrangell/St. Elias Mountains.

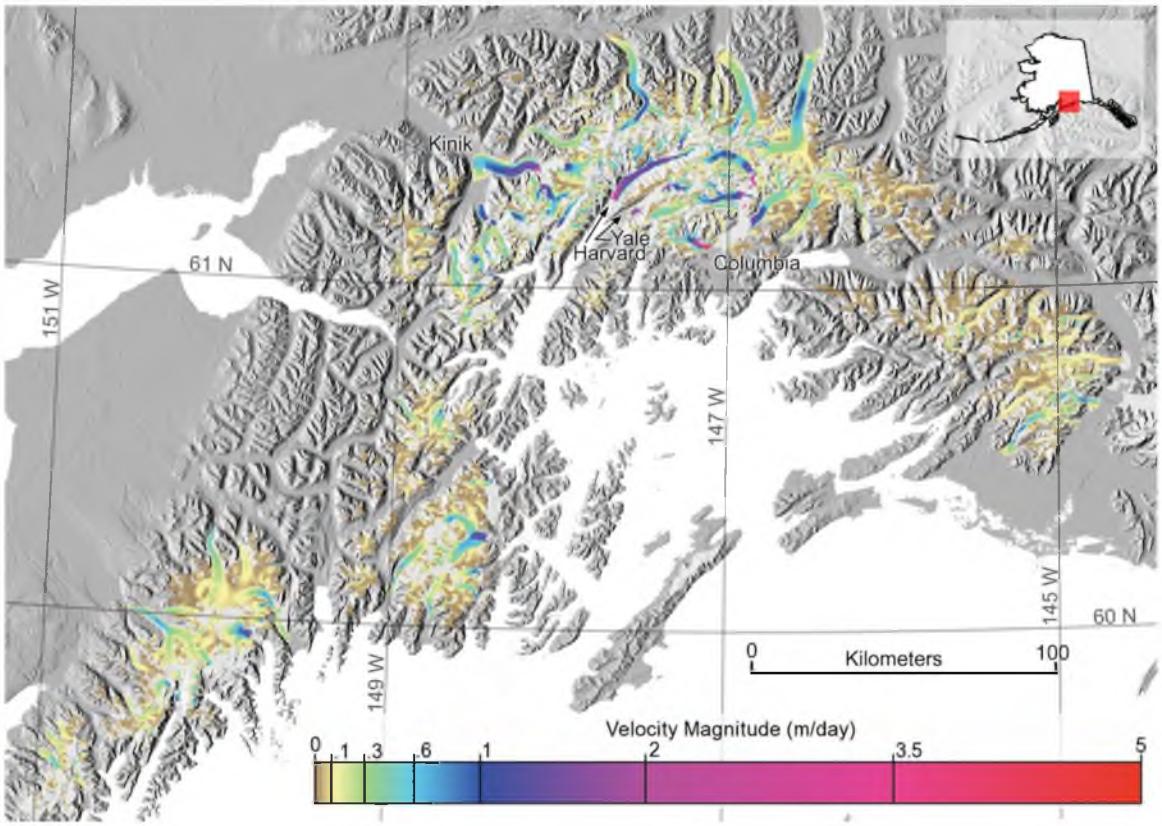


Figure 1.2. Glacier velocities in the Chugach Mountains and Kenai Peninsula.

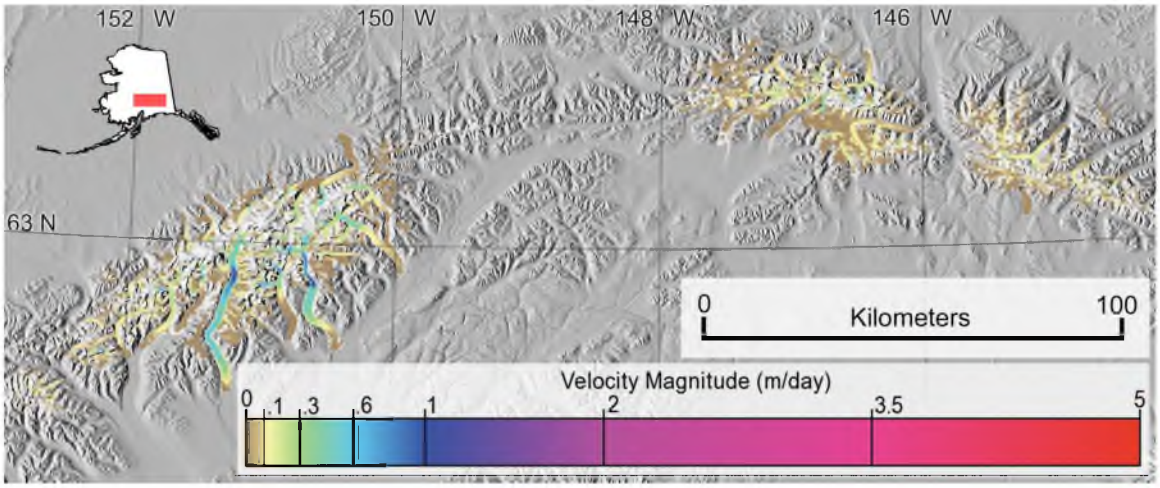


Figure 1.3. Glacier velocities in the Alaska Range.

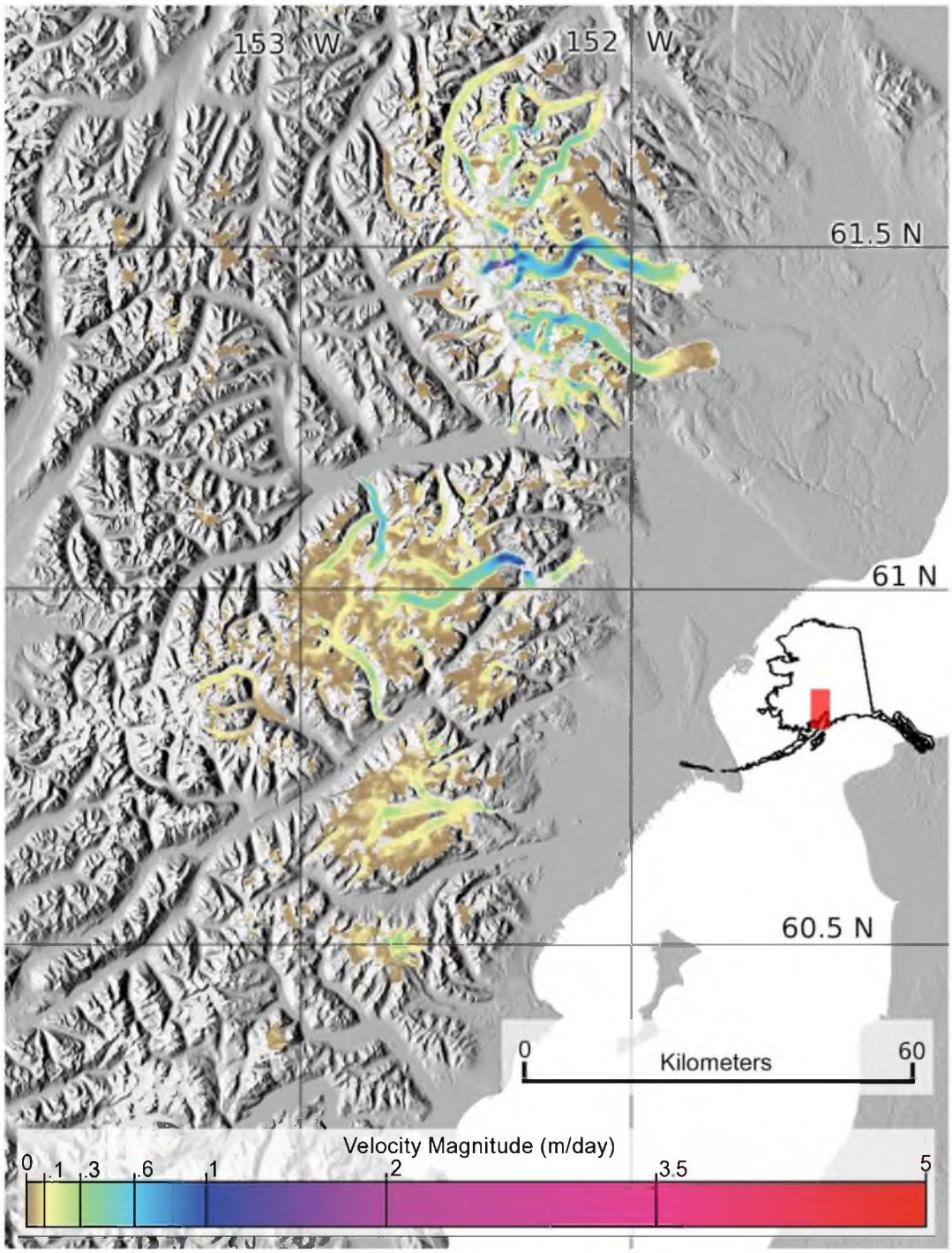


Figure 1.4. Glacier velocities in the Tordrillo Range.

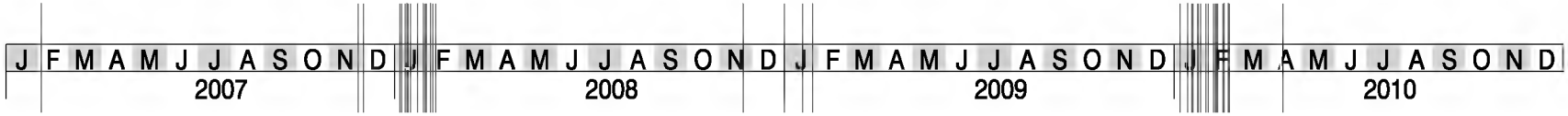


Figure 1.5. The dates of all 60 image pairs composing the velocity maps. Each line represents the mean day between a 46-day acquisition interval.

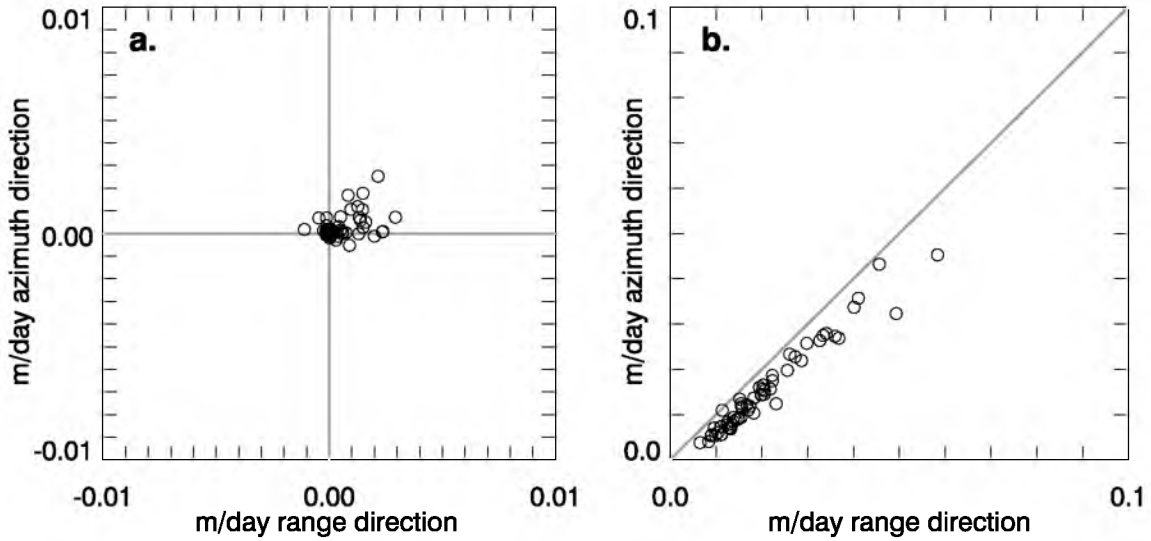


Figure 1.6. Estimated uncertainties for all 60 image pairs. **a.** Median values of all stable-ground offset vectors. **b.** Mean normalized median absolute deviation (robust equivalent to standard deviation) of all stable-ground offset vectors within each image pair, 1:1 line shown.

## 1.7 References


1. Meier, M. F. *et al.* Glaciers dominate eustatic sea-level rise in the 21st century. *Science* **317,** 1064–1067 (2007).

2. Larsen, C. F., Motyka, R. J., Arendt, A. A., Echelmeyer, K. A. & Geissler, P. E. Glacier changes in southeast Alaska and northwest British Columbia and contribution to sea level rise. *J. Geophys. Res.* (2007).

3. Arendt, A. *et al.* Updated estimates of glacier volume changes in the western Chugach Mountains, Alaska, and a comparison of regional extrapolation methods. *J. Geophys. Res.* **111,** (2006).

4. O'Neel, S., Pfeffer, W. T., Krimmel, R. & Meier, M. Evolving force balance at Columbia Glacier, Alaska, during its rapid retreat. *J. Geophys. Res.-Earth* **110,** (2005).

5. Berthier, E., Schiefer, E., Clarke, G. K. C., Menounos, B. & Rémy, F. Contribution of Alaskan glaciers to sea-level rise derived from satellite imagery. *Nat. Geosci.* **3,** 92–95 (2010).

6. Pfeffer, W. T. A simple mechanism for irreversible tidewater glacier retreat. *Journal of Geophysical Research F: Earth Surface* **112,** (2007).

7. Ritchie, J. B., Lingle, C. S., Motyka, R. J. & Truffer, M. Seasonal fluctuations in the advance of a tidewater glacier and potential causes: Hubbard Glacier, Alaska, USA. *Journal of Glaciology* **54,** 401–411 (2008).

8. Motyka, R. J., Hunter, L., Echelmeyer, K. A. & Connor, C. Submarine melting at the terminus of a temperate tidewater glacier, LeConte Glacier, Alaska, U.S.A. *Annals of Glaciology* **36,** 57–65 (2003).

9. Howat, I. M., Joughin, I., Fahnestock, M., Smith, B. E. & Scambos, T. A. Synchronous retreat and acceleration of southeast Greenland outlet glaciers 200006: ice dynamics and coupling to climate. *Journal of Glaciology* **54,** 646–660 (2008).

10. Joughin, I. *et al.* Ice-front variation and tidewater behavior on Helheim and Kangerdlugssuaq Glaciers, Greenland. *Journal of Geophysical Research: Earth Surface* **113,** 0–11 (2008).

11. Howat, I. M., Box, J. E., Ahn, Y., Herrington, A. & McFadden, E. M. Seasonal variability in the dynamics of marine-terminating outlet glaciers in Greenland. *Journal of Glaciology* **56,** 601–613 (2010).

12. Radić, V. & Hock, R. Regionally differentiated contribution of mountain glaciers and ice caps to future sea-level rise. *Nature Geoscience* **4,** 91–94 (2011).

13. Parizek, B. R. & Alley, R. B. Implications of increased Greenland surface melt under global-warming scenarios: ice-sheet simulations. *Quaternary Sci. Rev.* **23,** 1013–1027 (2004).

14. Iken, A. & Bindschadler, R. Combined measurements of subglacial water pressure and surface velocity of Findelengletscher, Switzerland: Conclusions about drainage system and sliding mechanism. *J. Glaciol.* 101–119 (1986).

15. Macgregor, K. R., Riihimaki, C. A. & Anderson, R. S. Spatial and temporal evolution of rapid basal sliding on Bench Glacier, Alaska, USA. *J. Glacio.* **51,** 49–63 (2005).

16. Bartholomaus, T. C., Anderson, R. S. & Anderson, S. P. Response of glacier basal motion to transient water storage. *Nat. Geosci.* **1,** 33–37 (2008).

17. Sundal, A. V. *et al.* Melt-induced speed-up of Greenland ice sheet offset by efficient subglacial drainage. *Nature* **469,** 521–524 (2011).

18. Van de Wal, R. S. W. *et al.* Large and rapid melt-induced velocity changes in the ablation zone of the Greenland Ice Sheet. *Science* **321,** 111–113 (2008).

19. Heid, T. & Kääb, A. Worldwide widespread decadal-scale decrease of glacier speed revealed using repeat optical satellite images. *The Cryosphere Discussions* **5,** 3025–3051 (2011).

20. Meier, M. F. & Post, A. What are glacier surges? *Can. J. Earth Sci.* **6,** 807–817 (1969).

21. Raymond, C. F. How do glaciers surge? A review. *J. Geophys. Res.* **92,** 9121–9134 (1987).

22. Muskett, R. R., Lingle, C. S., Tangborn, W. V. & Rabus, B. T. Multi-decadal elevation changes on Bagley Ice Valley and Malaspina Glacier, Alaska. *Geophys. Res. Lett.* **30,** (2003).

23. Post, A. Distribution of surging glaciers in western North America. *J. Glaciol.* **5,** 229–240 (1969).

24. Raymond, C. F. & Harrison, W. D. Evolution of Variegated Glacier, Alaska, U.S.A Prior to its surge. *J. Glaciol.* **34,** 154–169 (1988).

25. Heinrichs, T. A., Mayo, L. R., Echelmeyer, K. A. & Harrison, W. D. Quiescent-phase evolution of a surge-type glacier: Black Rapids Glacier, Alaska, U.S.A. *J. Glaciol.* **42,** 110–122 (1996).

26. Sauber, J. M. & Ruppert, N. in *Active Tectonics and Seismic Potential of Alaska* **179,** (American Geophysical Union, 2008).

27. Bruhn, R. L. *et al.* Plate margin deformation and active tectonics along the northern edge of the Yakutat Terrane in the Saint Elias orogen, Alaska and Yukon, Canada. *Geosphere,* **8,** 1384-1407, (2012)

28. Pelto, M. S. *et al.* The equilibrium flow and mass balance of the Taku Glacier, Alaska 1950-2006. *The Cryosphere Discuss.* **2,** 275–298 (2008).

29. Gray, A. L. *et al.* InSAR results from the RADARSAT Antarctic mapping mission data: estimation of glacier motion using a simple registration procedure. in *International Geoscience and Remote Sensing Symposium (IGARSS)* **3,** 1638–1640 (1998).

30. Strozzi, T., Luckman, A., Murray, T., Wegmuller, U. & Werner, C. L. Glacier motion estimation using SAR offset-tracking procedures. *Geoscience and Remote Sensing, IEEE Transactions on* **40,** 2384–2391 (2002).

31. Michel, R. & Rignot, E. Flow of Glaciar Moreno, Argentina, from repeat-pass Shuttle Imaging Radar images: Comparison of the phase correlation method with radar interferometry. *Journal of Glaciology* **45,** 93–100 (1999).

32. Copland, L. *et al.* Glacier velocities across the central Karakoram. *Annals of Glaciology* **50,** 41–49 (2009).

33. Quincey, D. J. *et al.* Karakoram glacier surge dynamics. *Geophys. Res. Lett.* **38,** 6 PP. (2011).

34. Kääb, A. Combination of SRTM3 and repeat ASTER data for deriving alpine glacier flow velocities in the Bhutan Himalaya. *Remote Sensing of Environment* **94,** 463–474 (2005).

35. Osmanoglu, B., Braun, M., Hock, R. & Navarro, F. J. Surface velocity and ice discharge of the ice cap on King George Island, Antarctica. *J. Glaciol.* **54,** 111–119 (2013).

36. Oerlemans, J. & Nick, F. M. A minimal model of a tidewater glacier. *Ann. Glaciol.* **42,** 1–6 (2005).

37. Huss, M. & Farinotti, D. Distributed ice thickness and volume of all glaciers around the globe. *Journal of Geophysical Research: Earth Surface* **117,** n/a–n/a (2012).

38. Zwally, H. J. *et al.* Surface melt-induced acceleration of Greenland ice-sheet flow. *Science* **297,** 218–222 (2002).

39. Eisen, O., Harrison, W. D. & Raymond, C. F. The surges of Variegated Glacier, Alaska, U.S.A., and their connection to climate and mass balance. *Journal of Glaciology* **47,** 351–358 (2001).

40. Bindschadler, R. A numerical model of temperate glacier flow applied to the quiescent phase of a surge-type glacier. *J. Glaciol.* **28,** 239–265 (1982).

41. Mcnabb, R. W. *et al.* Using surface velocities to calculate ice thickness and bed topography: a case study at Columbia Glacier, Alaska, USA. *Journal of Glaciology* **58,** 1151–1164 (2012).

42. Rasmussen, L. A., Conway, H., Krimmel, R. M. & Hock, R. Surface mass balance, thinning and iceberg production, Columbia Glacier, Alaska, 1948-2007. *J. Glaciol.* **57,** 431–440 (2011).

43. Luthcke, S. B., Arendt, A. A., Rowlands, D. D., McCarthy, J. J. & Larsen, C. F. Recent glacier mass changes in the Gulf of Alaska region from GRACE mascon solutions. *J. Glaciol.* **54,** 767–777 (2008).

44. Arendt, A. A. *et al.* Randolph Glacier Inventory [v2.0]: A Dataset of Global Glacier Outlines. (2012).

45. Joughin, I., Smith, B. E., Howat, I. M., Scambos, T. & Moon, T. Greenland flow variability from ice-sheet-wide velocity mapping. *Journal of Glaciology* **56,** 415–430 (2010).

46. METI and NASA. ASTER GDEM 2.0. (2011).

47. Balz, T., He, X., Zhang, L. & Liao, Mingsheng. TerraSAR-X stereo radargrammetry for precise DEM generation in South-East Asia. in *Change Monitoring and Detection* (2009).

48. Burgess, E. W., Forster, R. R., Larsen, C. F. & Braun, M. Surge dynamics on Bering Glacier, Alaska, in 2008–2011. *The Cryosphere* **6,** 1251–1262 (2012).

49. Maronna, R. A. *Robust Statistics: Theory and Methods*. (J. Wiley, 2006).

50. Cuffey, K. M. & Paterson, W. S. B. *The Physics of Glaciers, Fourth Edition*. (Academic Press, 2010).

51. Conway, H. *et al.* A low-frequency ice-penetrating radar system adapted for use from an airplane: Test results from Bering and Malaspina Glaciers, Alaska, USA. *Annals of Glaciology* **50,** 93–97 (2009).

# CHAPTER 2[1]

# SURGE DYNAMICS ON BERING GLACIER, ALASKA, IN 2008-2011

## 2.1 Abstract

A surge cycle of the Bering Glacier System, Alaska is examined using observations of surface velocity obtained using synthetic aperture radar (SAR) offset tracking, and elevation data obtained from the University of Alaska Fairbanks LiDAR altimetry program. After 13 years of quiescence, the Bering Glacier System began to surge in May 2008 and had two stages of accelerated flow. During the first stage, flow accelerated progressively for at least 10 months and reached peak observed velocities of ~7 m $d^{-1}$. The second stage likely began in 2010. By 2011 velocities exceeded 9 m $d^{-1}$ or ~18 times quiescent velocities. Fast flow continued into July 2011. Surface morphology indicated slowing by fall 2011; however, it is not entirely clear if the surge is yet over.

The quiescent phase was characterized by small-scale acceleration events that increased driving stresses up to 70%. When the surge initiated, synchronous acceleration occurred throughout much of the glacier length. Results suggest that downstream propagation of the surge is closely linked to the evolution of the driving stress during the

[1] Chapter 2 is reprinted from Burgess et al., (2012). Under the License and Copyright Agreement for articles published in *The Cryosphere*, "Copyright on any article is retained by the authors."

surge because driving stress appears to be tied to the amount of resistive stress provided by the bed. In contrast, upstream acceleration and upstream surge propagation isn't dependent on driving stress evolution.

## 2.2 Introduction

Glacier surging is a unique glacier dynamic behavior, in which, glacier flow speeds oscillate between two phases: a quiescent phase, characterized by slow flow that steepens glacier geometry, and a surge phase, characterized by extremely fast flow that flattens the geometry. Surge events exhibit flow speeds 10-100 times quiescent flow; they are relatively short, lasting from months to years, and can initiate and terminate rapidly (Cuffey and Patterson, 2010). The quiescent phase lasts decades, over which, the glacier develops a steeper geometry that triggers another surge event. The time required for the glacier geometry to steepen during quiescence dictates the duration of the quiescent phase and the surge cycle overall (Meier and Post, 1969; Raymond, 1987; Harrison and Post, 2003). Though there have been many studies focused on glacier surge dynamics, most of what is known about surging comes from observations on a few small glaciers over only 1-2 surge cycles (Meier and Post, 1969; Raymond, 1987; Raymond and Harrison, 1998; Bindschadler, 1982; Heinrichs et al., 1996).

Quiescent flow velocities are, on average, slower than balance velocities; thus surface mass balance causes thickening in the accumulation zone, thinning in the ablation zone, and a steepening glacier geometry overall. Such an evolution has been closely observed on Variegated Glacier during quiescent phase (Raymond and Harrison, 1988). However, during quiescence, some surge type glaciers have small acceleration events that

redistribute thickening and thinning along the glacier profile (Meier and Post, 1969; Raymond, 1987; Harrison and Post, 2003; Raymond and Harrison, 1988; Heinrichs et al., 1996). Ultimately, the quiescent phase develops a region of thickening called the reservoir zone, which forms upstream of a thinned receiving zone. The surge phase, theoretically, reverses this process, thickening the receiving zone and thinning the reservoir zone and returns the glacier geometry to where it was at the end of the previous surge. The boundary between the reservoir and receiving zones is termed the dynamic balance line (DBL) (Raymond, 1987).

The location of the DBL is no coincidence. The DBL is a surface expression of key changes in bed conditions that ultimately control the surge onset and surge progression. At the DBL, upstream thickening and downstream thinning steepens the glacier, which increases local driving stresses. This increase in local driving stress creates a trigger point for surge initiation by changing fundamental dynamics in the basal hydrologic system.

For most glaciers in Alaska, warm summer temperatures supply the bed with vast amounts of water. During quiescent phases, the basal hydrologic system has the ability to generate a channelized drainage system that can evacuate water inputs efficiently and prevent hydrologic pressurization of the bed (Rothlisberger, 1972). If water inputs increase rapidly, such as in spring or during rain events, the bed will pressurize, but only temporarily, while the channels expand to accommodate the additional flux.

The surge phase is thought to begin when the increased driving stress at the DBL prevents the glacier from attaining an efficient channelized drainage system. Rather, the high driving stresses promote and maintain a distributed subglacial hydrologic system that can only increase flux by increasing basal hydrologic pressure (Kamb, 1987). As a

result, basal water pressures remain extremely high, sometimes within a few bars of ice overburden pressure (Raymond, 1987). The high water pressure reduces the amount of shear stress the bed can support and the glacier accelerates until it is able to attain force balance. The stability of the distributed drainage system is thus a key parameter. In a distributed system model, Kamb (1987) defines such a variable called the melt stability parameter that is dependent on the basal shear stress and the smoothness of the bed.

The outstanding questions in understanding surge processes involve understanding exactly how the increased driving stress causes a discrete shift from a basal hydrologic system capable of channelization (quiescent phase), to a resilient distributed system (surge phase) before abruptly reverting back. The problem is we know little about actual conditions at the bed as they very difficult to observe. Most surge type glaciers are believed to have deformable sediment beds (Raymond, 1987) that can deform rapidly once the driving stress exceeds the yield stress of the sediment. Once the bed begins to deform, faster sliding velocities have little affect on the basal shear stress, therefore, the glacier can accelerate until lateral or longitudinal resistive stresses are able to attain force balance (Cuffey and Patterson, 2010). A key remaining question is how distributed/channelized systems evolve in subglacial systems with deformable or mixed beds.

Another outstanding problem is surges have been found to propagate downstream and upstream from their trigger point (Raymond, 1987). This propagation presumably is a consequence of reduced basal shear stress requiring increases in longitudinal or transverse stresses to maintain force balance. But exactly how this propagation evolves at the bed is not well understood.

The primary reason why these questions still stand is glacier beds are nearly impossible to observe over areas larger than a borehole. Thus, understanding how these processes evolve over large areas will require us to use readily observable surface expressions of bed dynamics to infer bed conditions. Here we examine the most recent surge cycle on the Bering Glacier System that initiated in May 2008 and is believed to have terminated in Summer 2011. We use altimetry data acquired between 1995 and 2011 and surface velocity data from 2007 to 2011 to examine the evolution of flow speed and driving stress during quiescent and surge phases.

## 2.3 Background

### 2.3.1 The Bering Glacier System (BGS)

The BGS is the largest surging glacier outside of the ice sheets (Molnia, 2008), covering 4,373 $km^2$ (Beedle et al., 2008) and accounting for 4% of the ice area in Alaska (Beedle et al., 2008; Berthier et al., 2010) and 6% of the mass loss (Arendt et al., 2002). It extends from ~100 m to 3000 m elevation with an equilibrium line at approximately 1000 m (Molnia, 2008). The BGS has a broad piedmont lobe that calves into Vitus Lake to the south and abuts the Stellar Lobe to the west. It is situated in coastal southern Alaska, in a maritime climate and has a high rate of mass turnover.

The geography and nomenclature of the BGS is rather complex (Figure 2.1). The BGS drains most of the westward flowing Bagley Ice Valley (BIV) and eastward flowing West Bagley (WB) (Figure 2.1). Ice from the BIV and WB converge at 30 km on the WB profile in Figure 2.1. There, the majority of the ice diverges south to form Bering Glacier. Ice on the northern edge of the WB and BIV are diverted north to form, the

smaller, Tana Glacier – this ice is not considered part of the BGS. The Jefferies and Quintino Sella Glaciers are tributaries of the BIV. The majority of the Jefferies ice flows north into the Tana and thus is not part of the BGS, while all of the Quintino Sella ice flows into the Bering and is part of the BGS. We herein refer to Bering Glacier as the portion of the BGS profile in Figure 2.1 from 85 km to the terminus and the BIV as the portion from 0 – 85 km. Otherwise, references to locations will refer to kilometer distances along the BGS or WB profiles as indicated in Figure 2.1.

### 2.3.2 BGS Surge History

The BGS has been steadily retreating over the past 100 years despite episodic advances during surge events in 1900, 1920, 1938 – 40, 1957 – 1960, 1965 – 1967 and 1993 – 1995 (Post, 1972; Molnia, 2008). Retreat rates between 1967 and 1993 were 0.04-1.0 km $yr^{-1}$ (Molnia and Post, 1995). Both the '65 – '67 and '93 – '95 surge events can be characterized as multistaged events, beginning with a high velocity event, followed by a period of near stagnant ice, followed by another high velocity event (Harrison and Post, 2003; Molnia, 2008; Roush et al., 2003; Fatland and Lingle, 2002).

The '93 – '95 event is the only BGS surge with quantified flow velocities; these results are worthy of summary to place the current surge in context. Surge onset occurred at approximately BGS-135 (Roush, 2003) (Fig. 2.1). The fastest velocity recorded was 59 m $d^{-1}$ near the terminus (Roush, 2003). More generally, flow velocities were 10 – 20 m $d^{-1}$ near the terminus (Roush, 2003) and up to 5 m $d^{-1}$ in the lower BIV (Fatland and Lingle, 2002). Both of these areas had velocities < 1 m $d^{-1}$ during quiescence (Post, 1972; Fatland and Lingle, 2002)). Velocity data were unable to confirm the existence of an organized

surge front propagating upstream or downstream from the onset location. A leading surface undulation propagated downstream from BGS-135 to the terminus at ~100 m $d^{-1}$ (Roush et al., 2003). Upstream propagation was less clear. Fatland and Lingle (1998) found a delay between surge onset on the Bering (~BGS-135 km) and a subsequent acceleration of the WB (Fig. 2.1), which lies ~60 km upstream. Assuming that the delay was due an upstream propagation front originating from the surge onset location, Fatland and Lingle (1998) estimated the upstream propagation velocity was 200 – 500 m $d^{-1}$. Fatland and Lingle (1998) also considered the possibility that the WB accelerated because of a linked subglacial hydrologic system and may not have been a classic propagating surge front as observed on the Variegated Glacier (Kamb et al., 1985; Raymond, 1987).

During the '93 – '95 surge, Fatland and Lingle (2002) found a distinct longitudinal change in ice dynamical behavior at a point just downstream of the Jeffries Glacier confluence, at BGS-45 (Fig. 2.1). Upstream this point in 1994, acceleration rates were temporally uniform and velocities were relatively similar to quiescent velocities. Downstream of this point, acceleration rates fluctuated rapidly (on 3-day timescales) and velocities increased dramatically in the downstream direction where uniform velocities existed prior to the surge. Short-term surface elevation changes, possibly indicative of transient subglacial water, were also more abundant downstream of this point during the '93 – '95 surge (Fatland and Lingle, 2002).

## 2.4 Data and Methods

### 4.2.1 SAR Offset Tracking

We use L, C and X band SAR platforms to generate ice displacement fields via offset/speckle tracking methods (Strozzi et al., 2002; Gray et al., 1998; Michel and Rignot, 1999). We use PALSAR ALOS Fine Beam (46-day repeat), RADARSAT Fine Beam (24-day repeat) ERS Ice Phases (3-day repeat) and TerraSAR-X StripMap (11-day repeat) data. Acquisitions are screened to obtain pairs with temporal baselines of 1 or 2 orbit intervals and perpendicular baselines <400 m for RADARSAT and ERS, <1000 m for PALSAR and <20 m for TerraSAR-X. We obtained a total of 77 frames, providing 40 pairs acquired between 2006 and 2010. For the final analysis, we use 21 PALSAR pairs, one TerraSAR-X pair acquired in 2011, and 2 ERS pairs acquired during the '93 – '95 surge (same data as used by Fatland and Lingle (1998, 2002)). The dates for these pairs are indicated on the timeline in Figure 2.2. Pairs could not be obtained at regular intervals due to poor data availability. Summer pairs were generally not utilized because SAR offset tracking was found to be ineffective during extensive melt, though two summer PALSAR pairs did yield usable displacement fields. The single July TerraSAR-X pair, with an 11-day repeat, also produced good results.

Single look complex (SLC) pairs are coregistered using spatial domain, normalized crosscorrelation optimization offset tracking within GAMMA® software (Strozzi et al., 2002). This method quantifies the displacement (offset) of pixel patterns between the two images. For each image pair, we derived offsets on stable ground adjacent to glaciers and assumed the offset vector field represents image coregistration. A polynomial function was fit to this offset field and then subtracted from the offsets observed on glaciers in the

same image pair. The BGS and surrounding ice is extensive enough to cover most of a single SAR frame (~70 km x 80 km); in these cases, glaciated ridgelines were allowed into the image coregistration in order to obtain an accurate offset polynomial. Related errors are discussed in Section 3.3.

Ice displacements were generated from the SLCs using the same intensity cross-correlation offset tracking method used for the initial coregistration, but with smaller window sizes. No terrain correction was applied, as resultant uncertainties were small (Section 3.3). SLCs were oversampled by a factor of two and all offsets with signal to noise ratios (Strozzi et al., 2002) below 6.0 were eliminated. We identified optimum search window sizes by testing throughout the parameter space; optimum sizes were 96 x 156 pixels (nominally, 721 m x 726 m in range and azimuth) and 100 x 200 pixels (nominally, 748 m x 629 m), for RADARSAT and PALSAR respectively. For TerraSAR-X, we use a window size of 256 x 256 pixels (232 m x 474 m).

In a few cases, slightly larger windows were used to improve results in areas of poor correlation. Results were not dependent on window size as long as the window was not large enough to extend through shear zones or onto stable ground. Shear zones on Bering Glacier are generally wider than 1.5 km (Fatland and Lingle, 2002).

Erroneous offsets were eliminated with a highly effective culling routine. The routine first uses a preliminary version of the Randolph Glacier Inventory 1.0 (nearly identical to RGI1.0) (Arendt, et al., 2012) to remove all off ice offset vectors. Next, offset vectors $\boldsymbol{v}$, are filtered by orientation. We define a median vector $\tilde{\boldsymbol{v}}_{i,j}^{w}$ which has the value of the median range and azimuth components of all vectors within a moving window with a center at location $i,j$ and width $w$. The angle between $\boldsymbol{v}_{i,j}$ and $\tilde{\boldsymbol{v}}_{i,j}^{w}$ can be defined as,

$$\theta = \frac{\cos^{-1}\left(v_{i,j} \cdot \tilde{v}_{i,j}^{w}\right)}{|v_{i,j}|\left|\tilde{v}_{i,j}^{w}\right|}. \quad (2.1)$$

If $\theta$ exceeds a threshold value, $\boldsymbol{v}_{i,j}$ is removed. The orientation filter is run iteratively with threshold values of 24,18 and 12 degrees. Finally, remaining vectors are filtered by direction and magnitude where $\left|\boldsymbol{v}_{i,j} - \tilde{\boldsymbol{v}}_{i,j}^{w}\right|$ must not exceed a threshold value. This routine removes better than 99% of erroneous vectors and removes very few false negatives. Finally, each scene is manually inspected to remove any remaining erroneous vectors and inspected for other problems.

Displacements were geocoded using the ASTER GDEM (METI and NASA, 2011) and SAR imaging geometry. The GDEM is generated through automated processing of many stereo pairs acquired between 1999 and 2011. The GDEM is the most up to date DEM available but is of poor quality, having many artifacts on the BGS. Since the geocoding was performed after offset derivation, the DEM artifacts don't affect the calculated velocities and only induce negligible errors in the geolocation process. All geocoded displacements were gridded onto the same 30 m UTM grid for comparison. Strain rates were computed following Nye (1959) and Bindschadler et al. (1996). Ice displacements were extracted along longitudinal profiles shown in Figure 2.1 for the BGS, WB and Jefferies/Tana glaciers (profile not shown). For purposes of clarity, we divert the BGS profile off the centerline from BGS-115 to BGS-140 to circumvent data voids (Fig. 2.1). Centerline velocities were higher, but extremely patchy results prohibit us from knowing by how much.

We estimate our velocity uncertainty for each image pair by using the same offset tracking method (Strozzi et al., 2002) on stable ground where offsets are assumed to be zero and any measured offset represents an error. Suitable areas for uncertainty estimates were manually delineated in each pair. Areas with steep topography or visible geometric distortion (foreshortening, layover, or shadowing) in the SAR images were excluded. These uncertainty estimates address errors associated with image coregistration, the lack of terrain correction, and the signal to noise ratio accepted in the offset tracking routine.

### 2.4.2 Airborne Altimetry

The University of Alaska Fairbanks (UAF) Laser Altimetry Program has flown repeat centerline surface elevation profiles on over 200 glaciers across Alaska and adjoining Canada since 1993 (Echelmeyer et al., 1996; Arendt et al., 2002, 2006). Centerline profiles of the BGS were flown in June '95 and '00, in August '00, '03, '07, in September '08 and in August '09, '10, and '11. These surveys used two different techniques: a nadir pointing laser (1995 – June 2009) and, more recently, a swath mapping LiDAR as part of NASA's Operation IceBridge (Aug 2009 – 2011) (Koenig et al., 2010).

The nadir pointing laser system results in a single track of surveyed points along the flight path, spaced roughly 1.0 to 1.5 m apart, whereas the LiDAR system results in a 500 m wide swath with roughly one surveyed point per square meter. Vertical accuracy of the surveyed points ranges from ±0.1 m to ±0.3 m and is dependent largely upon the quality of the trajectory solution for the aircraft (position and orientation from GPS and inertial measurement unit onboard the aircraft). To calculate changes in elevation between nadir

pointing laser surveys, we followed techniques and error estimations as described by Arendt et al. (2008). Calculating elevation changes between nadir laser surveys and LiDAR surveys, and between LiDAR to LiDAR surveys is done by interpolating the later survey onto a 5 m gridded surface, then sampling that surface at the earlier survey's points. In both of these cases, the inherent ambiguity between local slope (from the old point to the new point) and elevation changes is greatly mitigated relative to comparing two single tracks of points. To minimize seasonal effects on elevation changes, each interval was flown within 8 days of the date of the previous survey, with the exception of 39 days (late) in 2008.

## 2.5 Results

### 2.5.1 Efficacy of PALSAR in Maritime Climates

Not all SAR pairs produced useable offset results; the climate in Southeast Alaska rarely leaves a glacier surface unaffected by heavy snowfall or significant melt over a ~1 month interval. We find that, in this environment, temporal decorrelation is event (storm) based, rather than a gradual process, thus avoiding orbit intervals that span extreme storms or melt events can increase chances of obtaining good velocity results. In this climate, C band and X band sensors generally require surface definition such as crevassing and cannot track speckle alone (ERS ice phases with shorter repeats excluded), which limits spatial coverage significantly. In contrast, L band was extremely robust and able to track speckle reliably in this climate despite PALSAR's longer 46-day orbit interval. This strength is due to the longer wavelength providing deeper penetration and more stable scattering from subsurface snow and firn. TerraSAR-X was also

effective because of the extremely short orbit interval (11 days) and high spatial resolution. However, it may be limited in observing slower moving ice. X band decorrelates relatively quickly, thus requiring shorter intervals, which reduces accuracy.

### 2.5.2 Offset Tracking Uncertainties

We calculated uncertainty offset fields for 28 PALSAR pairs and 13 RADARSAT pairs. An average of 5030 offset values were calculated per image pair. The stable ground offsets/errors are not normally distributed, primarily because of extreme outliers. Thus, we use robust statistics including the median, interquartile range (IQR) and normalized median absolute deviation (MADn, a robust equivalent to standard deviation) (Maronna, 2006) to describe stable ground offset fields (Table 2.1). Dispersion metrics quantify stochastic uncertainty, while the mean absolute median provides an estimate of bias.

Both platforms have mean absolute median values $<0.01$ m $d^{-1}$ in both range and azimuth directions; random errors are larger (Table 2.1). PALSAR has larger stochastic errors in the range direction than in azimuth, whereas RADARSAT has isotropic stochastic error. PALSAR also has significantly larger perpendicular baselines than RADARSAT, thus it is likely that the larger errors in the range direction are a consequence of our lack of topographic corrections. This uncertainty is still too small to affect results.

During the surge, there is extreme velocity variability that has the appearance of noise in longitudinal profiles (visible in Fig. 2.2). Visual inspection of the velocity maps used to generate the profiles, suggests that much of the spatial variability is indeed real and not noisy results. However, rapid changes in surface conditions during the surge lead to a few

errant velocity vectors that appear as noise in the profiles. Surge phase image pairs do not have unusually high calculated uncertainties. We assume that these additional errors are stochastic and should not affect our conclusions.

### 2.5.3 Surge Dynamics

#### 2.5.3.1 Velocity Results

Between November 2007 and early March 2008, BGS velocities were consistently ~1 m $d^{-1}$ (Fig. 2.2) from BGS-30 – BGS-110. In late March – April 2008, flow velocities accelerated 20%, to 1.2 m $d^{-1}$ (at least between BGS-100 – BGS-130). This acceleration is confirmed by a concurrent increase in the number of ice quakes observed by a seismic array placed on the BGS at 110 km (LeBlanc, 2009). Offset tracking results were unavailable for late spring and summer 2008, but the same seismic array (LeBlanc, 2009) found the number of ice quakes increased by an order of magnitude in the first two weeks of May, indicating an onset of activity much greater than the previous year's spring speed up. Between September 2008 and February 2009 the BGS accelerated progressively from BGS-80 – BGS-135. Maximum observed velocities for the first stage were ~7 m $d^{-1}$. Actual peak velocities were likely higher, as this maximum velocity was observed in a side shear zone where data was unavailable at the glacier centerline (BGS-130). In January – April 2010 surface velocities from BGS-110 – BGS-140 slowed to quiescent speeds and velocities in the lower BIV (near BGS-90) were ~ 2 m $d^{-1}$. At the terminus, a narrow velocity peak at BGS-150 accelerated ~0.4 m $d^{-1}$ between March and April 2010 (Fig. 2.2).

Unfortunately no SAR data was obtainable between May 2010 and July 2011. During this period, aerial observations found decreasing crevassing until Jan – Feb 2011 when classic surge morphology (Herzfeld and Mayer, 1997) appeared again on the BGS (Larsen, 2011; Molnia and Angeli, 2011). These observations would suggest slower velocities throughout the summer and fall 2010 and a second high velocity stage beginning in Jan – Feb 2011 (Larsen, 2011; Molnia and Angeli, 2011).

The only velocity data obtained during the second high velocity stage was a single TerraSAR-X pair, obtained on July $5^{th}$ – $16^{th}$ 2011, which captured an 11-day interval of velocities from BGS-80 – BGS-123 (Fig. 2.3). The high resolution of TerrSAR-X reveals multiple arcuate propagation fronts on the glacier surface (Fig. 2.3) with velocities exceeding 9 m $d^{-1}$. Calculated longitudinal strain rates across the fronts exceed 6 $a^{-1}$ but are likely much higher in reality due to smoothing effects of the offset tracking routine.

These propagation fronts appear as extreme variability in the longitudinal profiles (Fig. 2.2). While these smaller fronts are quite evident, the velocity data do not show evidence of a uniform propagation front moving across the length of the BGS. Such a front would show a temporal delay in acceleration as one moves upstream. If we examine the period of acceleration between January 2008 and February 2009 at two locations (the lower BIV (80-90 km) and the BGS piedmont (110-130 km)) we see that the BIV reaches 45% and 86% of its peak velocity at the same time that the BGS piedmont reaches 33% and 70% of its peak velocity, respectively (Fig. 2.2). Therefore, the BIV reached a higher percentage of its total acceleration earlier than the BGS piedmont. Given the variability within the velocity data, we interpret this to imply that the BIV accelerated at least in unison with the Bering, if not before.

We cannot make the same comparison with the WB due to lack of data. However, the WB accelerated in unison with the BGS in February 2008—measurable acceleration (up to 26%) extended 20 km upstream of the confluence (Fig. 2.2, 2.4). The WB was back to quiescent velocities in November 2008, at the same time the BGS was accelerating rapidly. It accelerated again January 2009 when the BGS was flowing 7 m $d^{-1}$. By 2010, BGS velocities had slowed but the WB continued to accelerate.

Surge morphology was visible on Bering Glacier through summer 2011. A timelapse camera placed in the Grindle Hills (Burgess, unpublished data, 2011) looking in a northwesterly direction (location in Figure 2.1) between July 21$^{st}$ and September 15$^{th}$ captured little ice movement (exact velocities haven't been calculated). By fall 2011, continued aerial observations found the glacier surface had smoothed out significantly but no velocity data is available to confirm the surge termination.

2.5.3.2 Changes in Surface Elevation and Driving Stress

Altimetry data extends back to the end of the previous surge in 1995, with intervals of 5, 3 and 4 years during the quiescent phase and 1-year intervals during the surge. Figure 2.5a/b present the rate of surface elevation change and cumulative elevation change (from 1995) over each observation interval during the quiescent phase. Figure 2.6a/b presents the same for the surge phase.

In addition to surface elevation profiles, we provide a crude approximation of driving stress at the end of each interval in Figures 2.5c and 2.6c (quiescent and surge phases, respectively). For a rough approximation, thicknesses were assumed to be the surface elevation from the terminus to the equilibrium line (bed surface is close to sea level,

Conway et al., 2009). Above the equilibrium line, we assume a linear decrease in thickness to zero at the divide. Slope angles were derived from the ASTER GDEM (METI and NASA, 2011), using 6 km boxcar smooth to remove small scale variation and data artifacts. We assume that this DEM represents the glacier surface in 1995, and sequentially adjust the geometry with the surface elevation change data provided by altimetry. Driving stress is then calculated simply as $\rho g h \sin \alpha$ where $\rho$ is the density of ice, h is the ice thickness and $\alpha$ is the slope angle. Our crude assumptions on ice thickness and slope from the DEM will not affect our conclusions. This is because temporal changes in driving stress are sensitive primarily to the changes geometry, which are derived from precise and high resolution altimetry data.

2.5.3.2.1 Quiescent Phase

During the quiescent phase, a series of acceleration events set up the BGS geometry with a dynamic balance line and a trigger point at the approximate location of the '93 – '95 surge initiation. Between 1995 and 2000, a small acceleration event caused ~10 m of drawdown near BGS-80 and 5 m of thickening near BGS-97 (Fig. 2.5a, b). Between 2003 and 2007, another, larger acceleration event occurred, which drew down the reservoir zone by up to 20 m at BGS-60 and thickened Bering Glacier by up to 35 m near BGS-110. These two events were discrete in time, but both had a DBL at about the same location (BGS-90). Furthermore, both events steepened the glacier geometry and consequently, increased driving stresses at BGS-120 – BGS-130 (Fig. 2.5b, c).

Over the quiescent phase, the DBL migrated downstream as seen on Variegated and Medvezhiy Glaciers (Raymond, 1987), and eventually set up at BGS-123 in 2007.

However, all new/added mass from the accumulation zone was redistributed to a confined reservoir zone between BGS-85 and the DBL. Driving stresses throughout most of the BGS were unchanged from the end of the previous surge to the start of the recent surge.

However, driving stresses near the DBL (BGS-120 to BGS-130) increased up to 70% (or ~50 kPa) during the quiescent phase. Upon surge onset, this region had the strongest acceleration and fastest velocities, which caused a clear switch in longitudinal stress (Fig. 2.2, 2.5d). Thus, we can consider this region, between BGS-120 to BGS-130, to be the trigger zone for the first stage of the surge (grey highlight in Figs. 2.2, 2.5, 2.6). The DBL during the first phase of the surge ('07 – '09) was at BGS-122—only 1 km from the DBL during quiescence (Fig. 2.5d). Again, this was also the approximate location that the 1993 – 1995 surge is thought to have initiated (Roush, 2003).

2.5.3.2.2 Surge Phase

The altimetry data shows a distinct difference between the first and second stages of the surge. Note the location of the DBL during the surge (Fig. 2.6a). The two intervals from 2007 to 2009 cover the first stage and have a DBL at BGS-122—precisely where it was during quiescence. Then, during the intervals from 2009-2011, the DBL makes a discrete shift downstream to BGS-147. An explanation for this downstream shift is readily available, but requires a closer look at the first stage.

During the initial acceleration of the first stage ('07-'08), a peak in thickening formed at BGS-130. Over the following year, this peak reoccurred, but a much higher peak also formed downstream at BGS-142. These two thickening peaks have important

consequences with respect to the driving stress. The upstream side of the peak at BGS-130 reduced the driving stress at the DBL (BGS-123), creating a minimum approximately equivalent to what it was in 1995. The thickening peak at BGS-142 thickened and steepened the geometry from BGS-140 – BGS-153. This change in geometry during the first stage, nearly doubled the driving stress at BGS-147 (Fig. 2.6c) and, subsequently, was the DBL during the second stage.

The 2009 – 2010 altimetry interval is unique. Sharp thickening is confined to a small area around BGS-150. A very subdued bulge occurs between BGS-90 – BGS-120 and drawdown extends further upglacier than in any other interval. Interpreting what happened over the 2009-2010 altimetry interval can be eased through comparison with the 2010 velocity profiles in Figure 2.2 (green lines). Note the two velocity peaks at BGS-90 and BGS-150 fit well with the altimetry. The peak at BGS-90 is very broad, extends well up into the BIV and shows little month to month velocity change in 2010. The peak at BGS-150 is sharp and accelerates 0.4 m $d^{-1}$ in less than 1 month. The morphological differences between the upstream and downstream velocities lead us to speculate that the broad accelerated velocities and drawdown in the BIV are a remnant of the first stage, while the sharp acceleration in April 2010 and thickening over the 2009-2010 interval represent the onset of the second stage.

Over the 2010 – 2011 altimetry interval we see the main part of the second stage. During this period, the surge reached the terminus and advanced the terminus 2-4 km (Turrin et al., 2011). Like the first stage, the DBL didn't move throughout the entire stage, but thickening moved downstream. Drawdown during the first and second stages was remarkably similar in extent, magnitude and shape (compare '08-'09 and '10-'11

intervals in Figure 2.6a) with the exception that the reservoir zone extended further downstream during the second stage.

The second stage did little to subdue the large undulations in driving stress and topography created by the first stage (between BGS-125 and BGS-145). Rather, the drawdown was more or less uniform from BGS-80 – BGS-140. However, upon close examination of the '10-'11 interval in Figure 2.6a, one will see an extremely subdued undulation in the drawdown that matches the '08-'09 profile. This key point suggests that the mechanisms that created the two peaked thickening during the first stage, still existed in the second stage but were massively diminished.

2.5.3.3 A confined active surge zone in the BIV

During 2008 – 2010 and 1993 – 1995, there was a key shift in ice dynamics at BGS-45 (Fig. 2.2). Upstream of BGS-45, surge velocities remained close to quiescent velocities. Downstream of BGS-45, velocities increased rapidly in a step like fashion. Strain rates (not shown) indicate the peak at BGS-80 (Fig. 2.2) is caused by longitudinal compression as the BIV joins with the WB. The cause of the deceleration at BGS-65 is less clear but is probably due to bed topography. At this point, there is extensional lateral strain as ice spreads northward and compresses ice on the north side of the BIV.

The north side of the BIV receives its ice from the Jefferies Glacier, which eventually flows into the Tana (Fig. 2.1). This ice accelerated very little—from 0.5 to 0.7 m $d^{-1}$—during the BGS surge. A wider shear zone on the north side of the BIV is visible in Fig. 2.1. Also notable, the longitudinal step like accelerations seen on the BGS portion of the BIV, didn't occur on ice originating from the Jefferies Glacier (Fig. 2.1, 2.2). Rather,

velocities were relatively uniform from the Jefferies to the Tana. The Bagley fault runs along the BIV and possibly forms a longitudinal ridge structure that separates BGS ice and the Tana Glacier ice. This structure likely extends towards the north edge of the West Bagley and diverts the majority of the ice southward into Bering Glacier (Plafker, 1987; Bruhn et al., 2004; Bruhn et al., in press). Flow velocities on the Tana Glacier changed by only ~0.1 m $d^{-1}$ throughout the '08 – '11 BGS surge; the highest velocities were actually prior to the surge, in 2007.

## 2.6 Discussion

After a 13 year quiescent phase, the BGS began a full scale surge in May 2008 that appears to have ended in Summer 2011 (uncertainty on termination will be addressed later in this section). While we do not have any data on bed conditions during the surge, close examination of the velocity and altimetry data allow us to make inferences about the relative amount of drag provided by the bed. Most importantly, we can reach conclusions about the basal hydrology by examining the persistency of basal drag features during surge evolution.

During the quiescent phase, small scale acceleration events occurred that relocated any new mass in the accumulation zone to a small reservoir zone just downstream of the BIV/WB confluence at BGS-85 – BGS-123. The fact that large acceleration events did not occur between '00 and '03 suggests that these acceleration events are not purely a consequence of increases in deformational velocity; rather, basal sliding likely plays a role. Such events are similar to events observed on Medvezhiy and Black Rapids Glaciers, acknowledging key differences in geometry and size (Dolgushin and Osipova,

1978; Raymond, 1987; Heinrichs et al., 1996). One consequence of the quiescent acceleration events was, when the surge began, the entire BIV was at the exact same level as it was at the end of the previous surge—driving stresses were unchanged as well. Thickening from both quiescent phase acceleration events stopped abruptly at the DBL; consequently, driving stresses increased by 70%. This area represents a key transition in longitudinal stress and can be considered the trigger zone for the first stage.

During the surge, the DBL remained stationary during each stage but made a discrete downstream shift between the two stages (Fig. 2.6a). We hypothesize that this downstream shift is a consequence of driving stress evolution during the first stage. During the first stage, thickening occurred at two peaks at BGS-130 and BGS-142; both of which are upstream of the DBL for the second stage. Downstream of the second peak, thickening and steepening around BGS-145 increased local driving stresses and created a new trigger point and DBL for the second stage.

The two thickening peaks are the result of compressive longitudinal strain as the high flow speeds decline in the downstream direction. This reduction in flow speed and thickening is likely due to an area of relatively higher basal drag that resists rapid flow from upstream. The second peak had provided drag to stop the entire surge and prevent any thickening downstream of BGS-150.

During the second stage, the two points of relatively high drag largely disappeared. Thinning and extensional flow persisted past these points and allowed the surge to extend to, and advance the terminus in 2011. This progression is very similar to that of the 1982 surge of Variegated Glacier (Raymond, 1987; Kamb et al., 1985). Thickening and compressional flow during the second stage occurred downstream of a new DBL at BGS-

142—immediately downstream of where driving stresses were elevated by the first stage. Note that the second stage did little to subdue the two thickening peaks from the first stage; rather it drew down the BGS uniformly, from BGS-65 to BGS-142. Without knowledge of the bed conditions we can only speculate as to what reduced the basal drag at these two sticky points during the second stage.

One speculative explanation lies in the driving stress and is qualitatively supported by conclusions by Kamb (1987). Throughout the quiescent and surge phases we see a reoccurring process. Areas with low driving stresses provide drag that causes ice to pile up behind the drag feature and consequently increase driving stresses at the drag feature. In winter, the channelized system is destroyed and if local driving stresses are elevated to a threshold, the elevated driving stress helps to promote and maintain a distributed hydrologic system and prevent channelization (Kamb, 1987). Low effective pressures can thus be maintained for extended periods of time. The shear stress on the bed is reduced and the ice is able to accelerate further downstream until it reaches another high drag location.

The existence of these high drag spots does not appear to be entirely a function of driving stress. The small undulations in thinning rate between BGS-120 – BGS-150 on the '10-'11 altimetry interval suggest that there are features on the bed that continue to provide additional drag despite the collapse of the channelized system. Thus these areas at BGS-130 and BGS-142 could have some combination of higher surface roughness features and/or more hard beds, though this is highly speculative.

There is an obvious hitch with this hypothesis. The driving stress in 2011, after what is believed to be surge termination (Fig. 2.6c), is still elevated at sticky spot locations.

This would imply that either: 1) our explanation is missing a key component, or 2) the BGS is still not in a stable geometry and the surge is not yet over. We have no velocity data after our TerraSAR-X pair acquired in July 2011. Aerial observations have seen moderate crevassing in 2012 and previous surges terminated with a large outburst flood (Molnia, 2008), which has not yet been observed with the recent surge.

The issue of surge propagation was only loosely observed during the previous surge and our observations for the recent surge indicate a different picture. At the onset of the first stage, velocities didn't only accelerate near the trigger zone; rather the majority of the BGS between BGS-50 and BGS-140, and the WB, all accelerated at the same time. Thus, the initial acceleration can't be due to kinematic wave propagation and must be to hydrologic pressurization of most of the BGS in May 2008. If one looks at the four altimetry intervals during the surge, drawdown follows a consistent curve and eventually stops at about BGS-75, except for the '09 – '10 interval. Thus for the majority of the first stage and the second stage, we see no large scale upstream propagation at all. In '09 – '10, drawdown did extend further up into the BIV but this drawdown and acceleration occurred with a slight decrease in local driving stress. Throughout the entire surge, driving stresses upstream of the DBL barely changed at all.

Therefore, we conclude that the extensive thinning from BGS-45 to the DBL is purely a consequence of elevated hydrologic pressures at the bed, not due to evolving driving stress from kinematic wave propagation. Areas closer to the trigger zone accelerated more, perhaps simply due to higher basal water pressures, thus creating extensional flow upstream of the trigger zone and thinning. Downstream propagation however, appears to be closely linked to changes in the driving stress. At persistent sticky points, elevated

driving stress appears reduce basal drag and allow high flow velocities to continue further downstream.

Why there does not appear to be high drag areas above BGS-123 is an interesting question. One simple explanation could be that the bed conditions are simply different above BGS-123 and are more amenable to maintaining pressurized distributed systems and low basal shear stresses. Another explanation could be that the bed upstream of BGS-123 is not significantly different from the bed downstream, and instead, the reason why there are not sticky spots above BGS-123 is because of higher driving stresses. If we consider the distribution of driving stress throughout the BGS length, the region between BGS-80 to the BGS-123 has significantly higher driving stresses than elsewhere—near 100 kPa. This area is also the reservoir area for the surge, and the area where rapid acceleration is seen at surge onset. Upstream of BGS-45, where driving stresses are low, ice may accelerate slightly due to kinematics, but surge velocities ('93 – '95 and '08 – '10) and quiescent velocities (2007) vary by little (<0.35 m $d^{-1}$). During the previous surge, Faltland and Lingle (2002) noticed little short term acceleration in velocity upstream of BGS-45. Thus, these data suggest that much of the BGS system requires a critical basal shear stress (80-100 kPa) to facilitate rapid sliding. Given our crude driving stress model, this interpretation is qualitative and the magnitude of the driving stress should not be taken exactly.

We have little evidence to address the question of why the surge evolves in two stages. The '93 – '95 surge had two phases that both began in winter and terminated in summer (Molnia, 2008). In the recent surge, the first stage began in spring and the second began in winter. Termination dates are unknown with certainty but could be in

summer, in particular for the second stage. One explanation (Kamb, 1987; Eisen et al. 2005) is high ablation rates during summer can force the glacier to return to a channelized drainage system, increasing the effective pressure and basal shear stress. Over the course of fall and winter, the drainage system is able to close and revert back to a high pressure distributed system, thus allowing the second phase to initiate.

In the case of the recent BGS surge, it is interesting that the first acceleration period lasted at least ten months (May 2008 – Feb 2009) and took place primarily in fall but also in summer. The 2008 summer however was exceptionally cold (Alaska Climate Research Center, 2012) thus likely produced relatively little melt water input to the bed and could have allowed the distributed system to persist into fall. The first stage terminated sometime during 2009, and velocity increased again the following winter. Thus, the BGS two stage cycle could be explained by this theory as well.

## 2.7 Conclusion

Surface velocity data, altimetry and calculated driving stresses reveal glacier dynamics throughout a complete surge cycle of the Bering Glacier System. Dynamics throughout this cycle show distinct similarities to surge cycles observed on much smaller glacier systems, which suggests consistency in mechanism despite a huge difference in size. We find that areas capable of rapid acceleration are confined to areas of relatively high driving stresses. Since driving stresses decline closer to the terminus due to thinning ice, periodic acceleration in the area of high driving stress causes longitudinal compression and thickening/steepening geometry. This thickening/steepening effectively expands the area of high driving stress and allows rapid flow to advance further

downstream. However, as the driving stress evolves during each stage, the basal drag doesn't dynamically adjust to the evolving driving stress. Rather, we find that the rapid flow must shut down and reset for another stage before the DBL can move downstream. We suggest that high driving stresses are maintaining an existing distributed system that forms over a winter season but can't initiate a transition from a channelized system to a distributed system given additional driving stresses. These conclusions are still highly speculative as no data on basal water pressures are available. Further analysis and modeling could provide more insight into the bed mechanisms responsible for these observed dynamics.

## 2.8 Acknowledgements

We thank Ron Bruhn, Jeanne Sauber, Michelle Cotton for their insightful ideas and discussion. E. Burgess is funded under the NASA Earth Science Space Fellowship. R. Forster and the velocity work were funded by NASA Grants NNX08AP27G and NNX08AX88G. C. Larsen and UAF LiDAR altimetry program were funded by NASA's Operation Ice Bridge Grant NNH09ZDA001N (2010), NASA Grant NNX09AP54G (2009), NSF ARC-0612537 (2008), and NASA Grant NNH07ZDA001N-CRYO (2007). M. Braun was supported by NASA Grant NNX11AF41G and TerraSAR-X data was provided under DLR AO LAN_0164. The Alaska Satellite Facility provided ALOS and ERS data.

**Table 2.1.** Statistics describing the 2-D distribution of measured ground displacements in ice free terrain (units in m $d^{-1}$)

| | RADARSAT | | PALSAR | |
|---|---|---|---|---|
| | Range | Azimuth | Range | Azimuth |
| Mean STDEV | 0.251 | 0.259 | 0.094 | 0.081 |
| Mean MADn | 0.033 | 0.033 | 0.024 | 0.013 |
| Mean IQR | 0.045 | 0.045 | 0.033 | 0.017 |
| Mean Absolute MEDIAN | 0.005 | 0.009 | 0.006 | 0.002 |

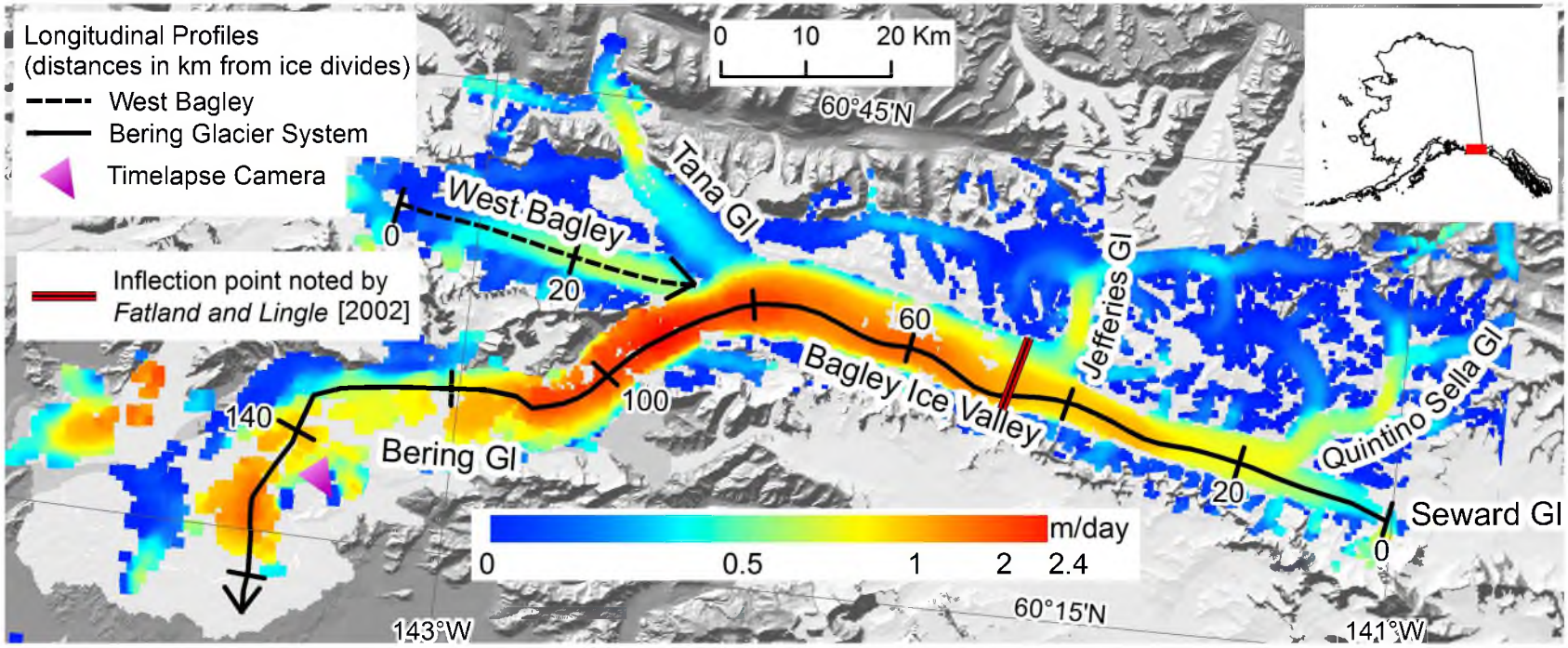


Figure 2.1. Composite velocity map of the BGS and Tana Glaciers in Winter 2010. The BGS and WB longitudinal profiles apply to Figures 2.2 and 2.4, respectively. Profiles begin at ice divides and distances increase in the direction of flow. White glacier outline provided by Armstrong et al., (2005).

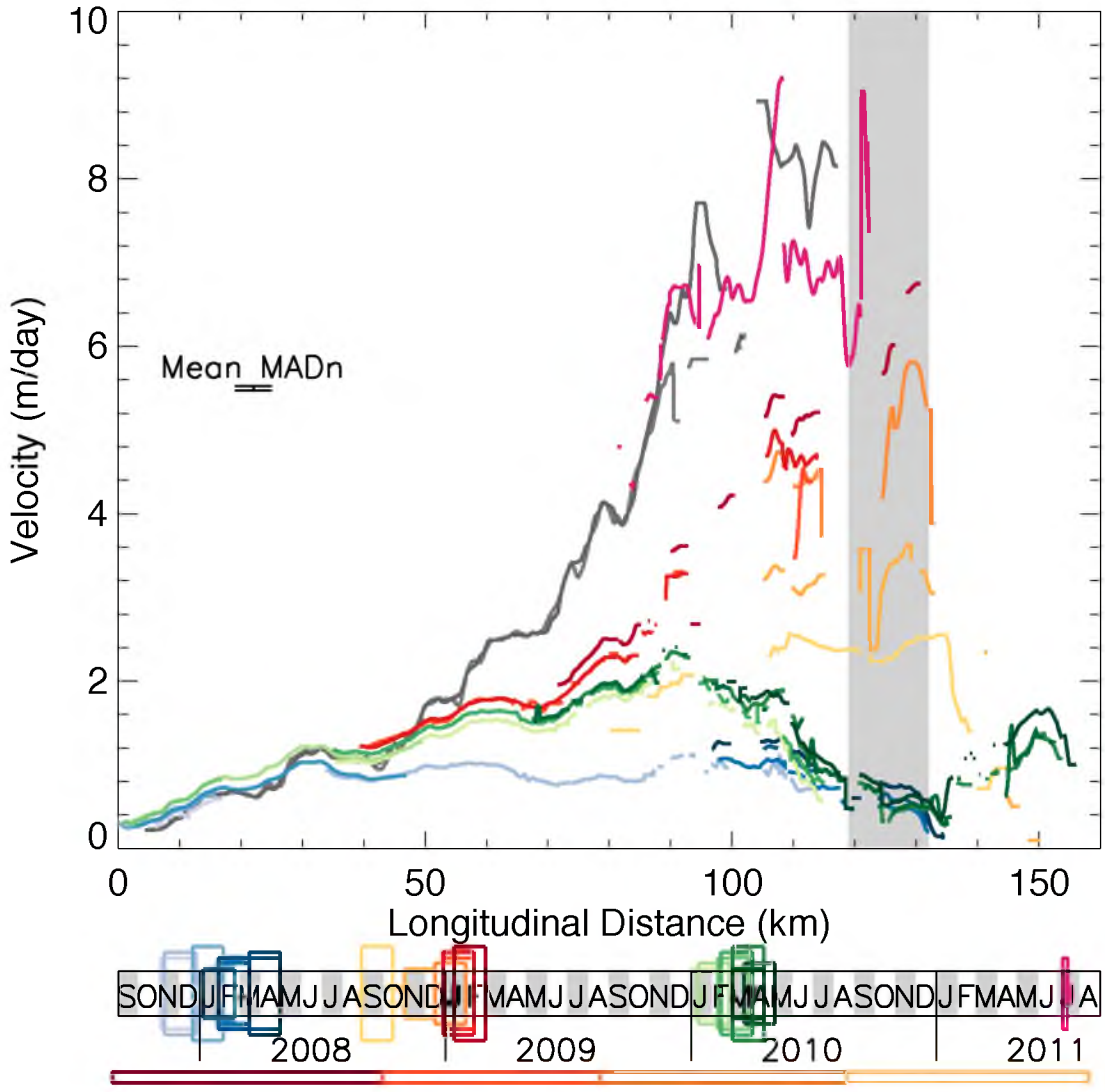


Figure 2.2. Bering Glacier System longitudinal velocity profile (location in Figure 2.1). Dates of image pairs are denoted by the colored boxes in the timeline. The width of each box indicates the length of the interval; heights of the boxes are for visual clarity only. Colors gradually darken as time moves forward each winter. Thin colored boxes below the timeline show dates of altimetry intervals in Figures 2.5 and 2.6. BGS velocities in January 1994, during previous surge are shown as grey data line. The location of the trigger zone for first stage is indicated by the grey box.

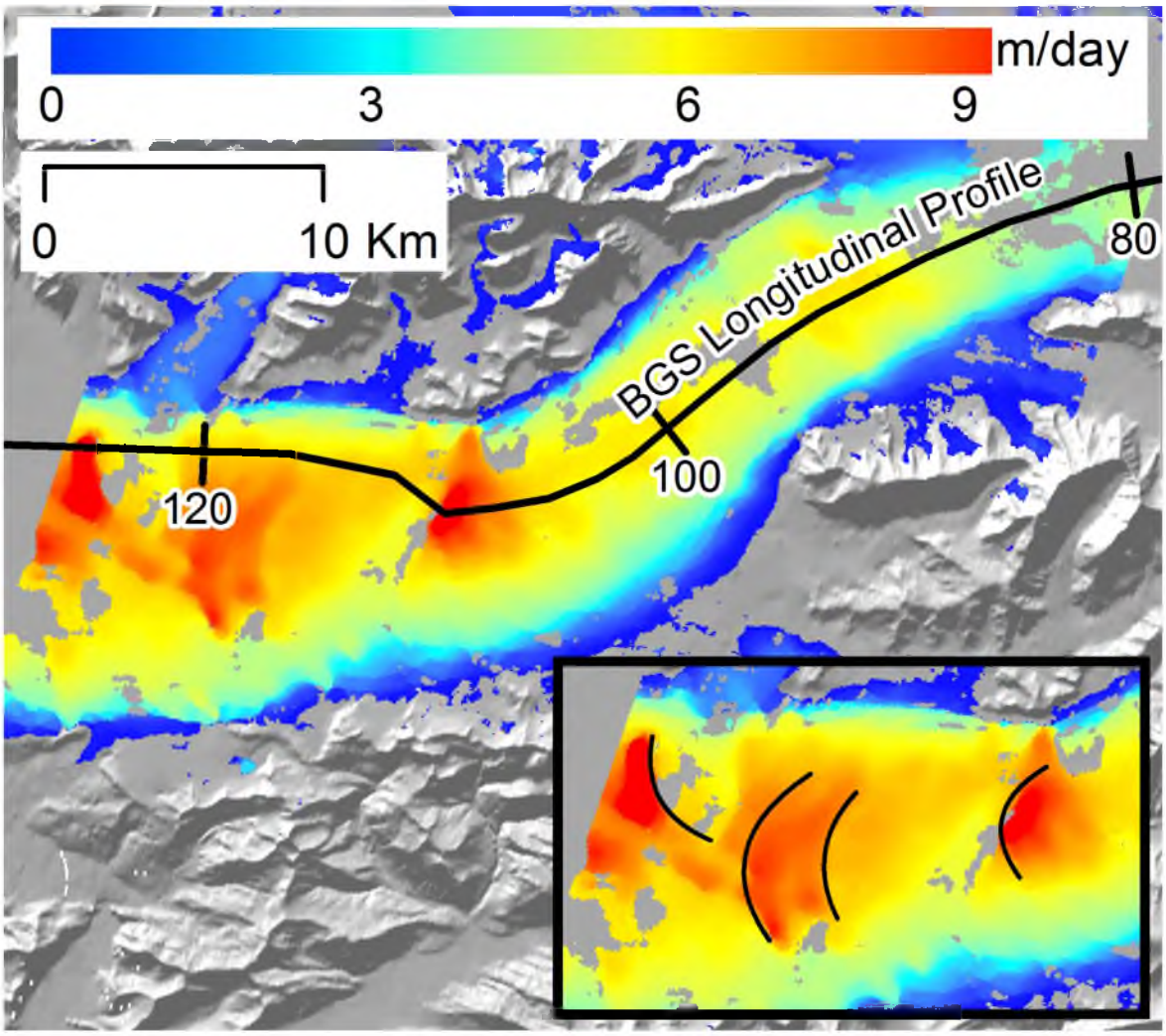


Figure 2.3. High-resolution velocity field during second phase of the surge over 11-day interval (5 -16 July 2011) from TerraSAR-X. Location of propagation fronts marked in inset map.

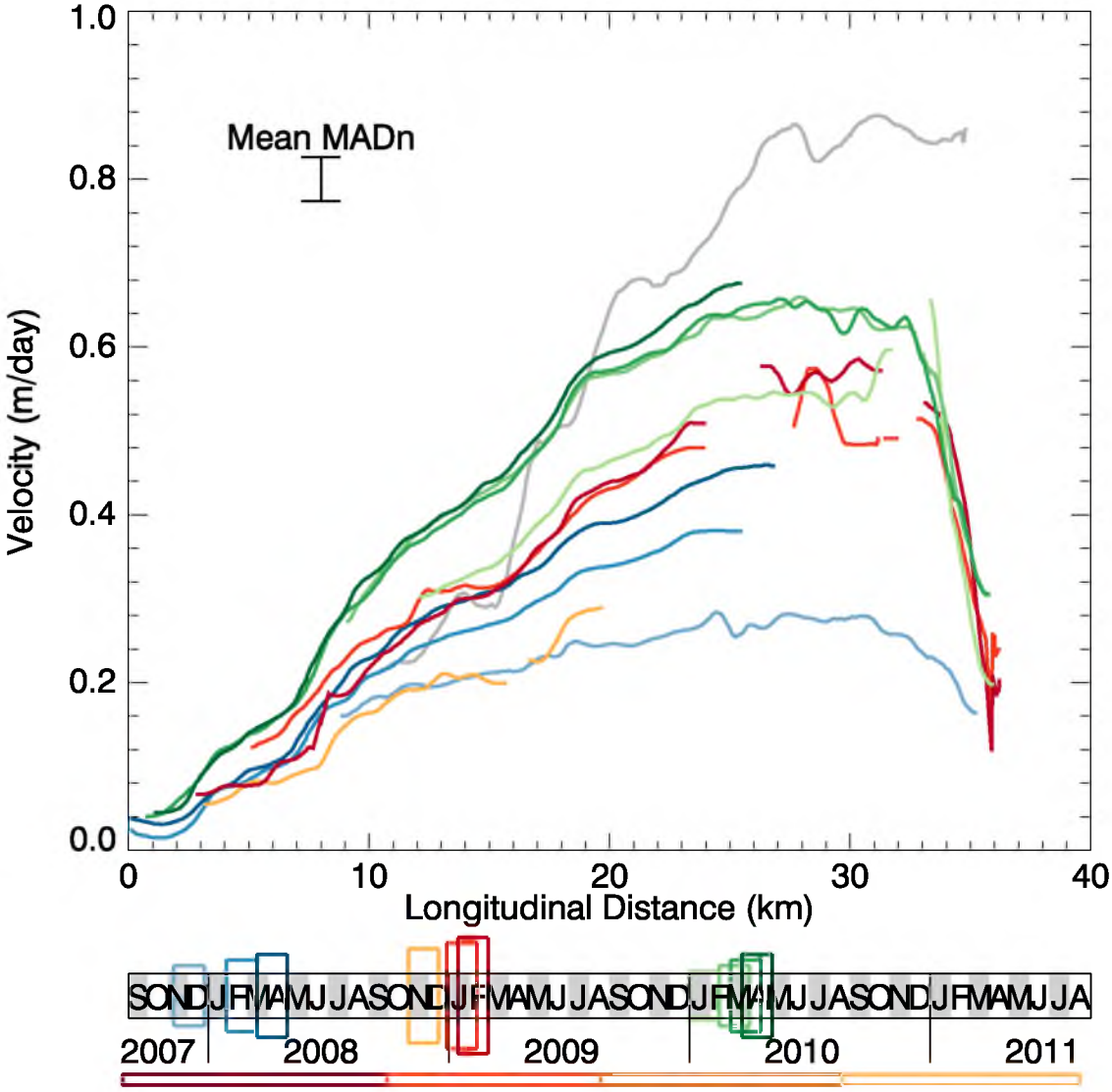


Figure 2.4. West Bagley longitudinal velocity profile (location in Figure 2.1). Dates of each image pair are denoted in the timeline below as in Figure 2.2. Colors gradually darken as time moves forward each winter. The grey data line shows WB velocities in January 1994. Note scales are different than Figure 2.2.

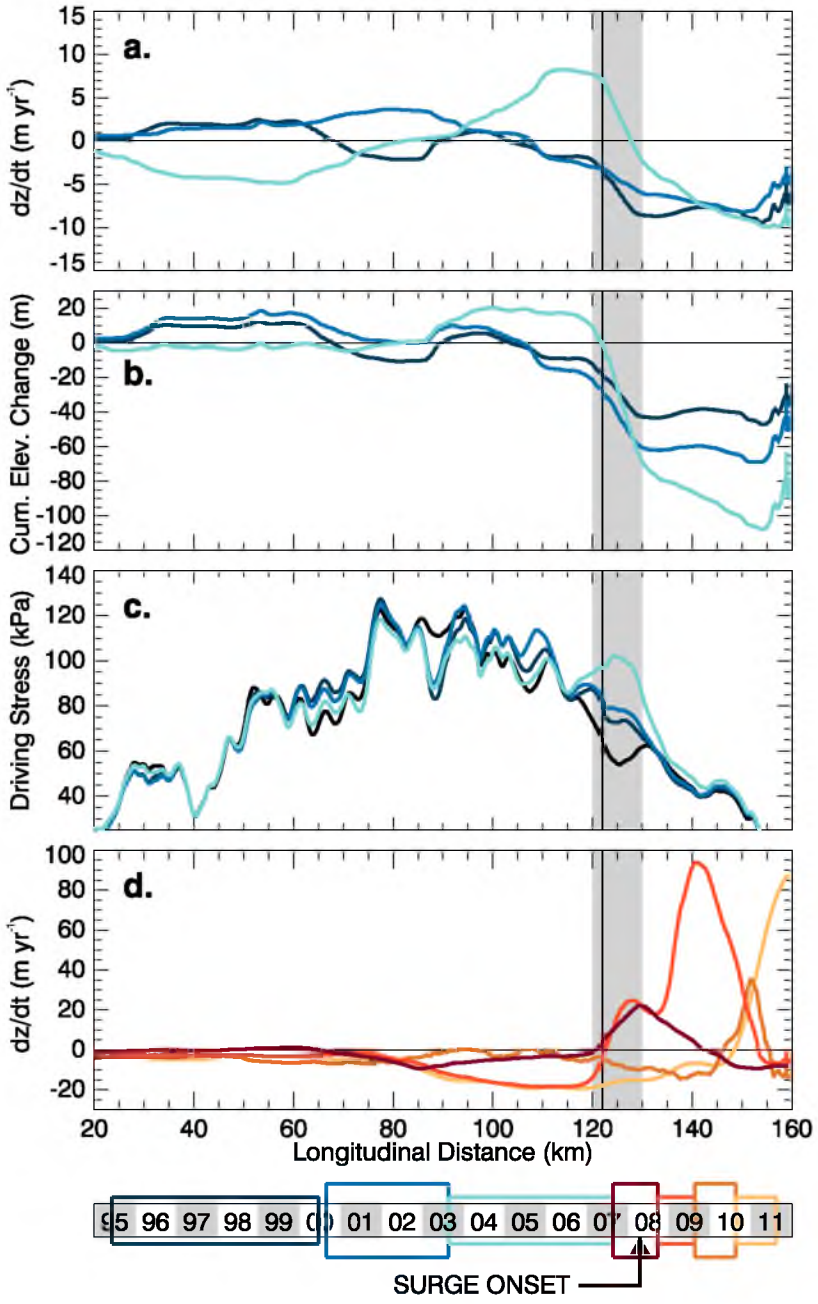


Figure 2.5. Results from airborne altimetry on the BGS profile. Flight intervals are indicated on the timeline at the bottom. Blue and red hues correspond to quiescent and surge phases, respectively. Colors lighten though time. Grey box and vertical line marks the trigger zone and DBL for the first stage, respectively. Figure 2.5a. Surface elevation change rate during quiescence. b. Cumulative elevation change from 1995. Colors correspond to the surface profile at the end of each interval. c. Calculated driving stresses. Black line represents driving stress in 1995. Colors correspond to the driving stress at the end of each interval. d. Surface elevation change rate during the surge phase (same as Figure 2.6a).

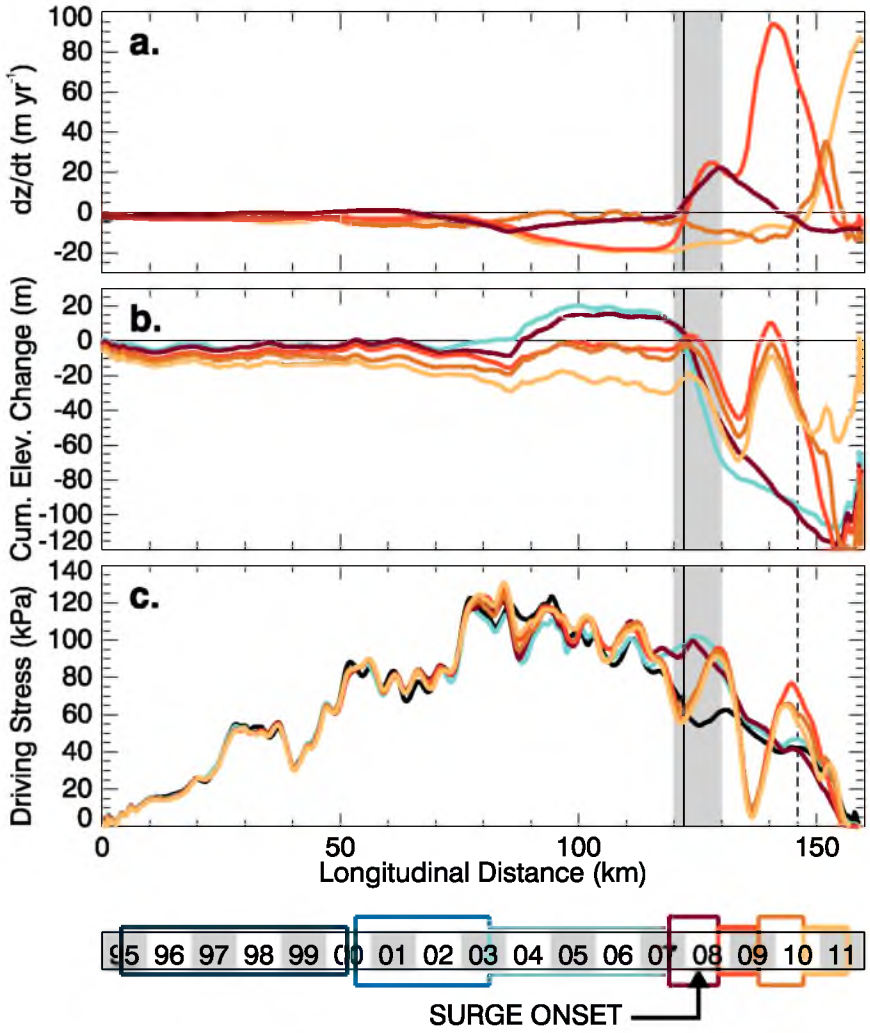


Figure 2.6. Results from airborne altimetry on the BGS profile, cont'd. Colors, intervals and notation represented as in Figure 2.5. Dotted line represents DBL for the second stage. Figure 2.6a. Surface elevation change rate during the surge phase (same as Figure 2.5d, provided for comparison). b. Cumulative elevation change from 1995. Colors correspond to the surface profile at the end of each interval. c. Calculated driving stresses. Black line represents driving stress in 1995. Colors correspond to the driving stress at the end of each interval.

## 2.9 References

Alaska Climatology: Alaska Climate Research Center, http://climate.gi.alaska.edu/Climate/index.html, last access: 15 Aug 2012.

Arendt, A. A., Echelmeyer, K. A., Harrison, W. D., Lingle, C. S. and Valentine, V. B.: Rapid wastage of Alaska glaciers and their contribution to rising sea level, science, 297(5580), 382–386, doi:10.1126/science.1072497, 2002.

Arendt, A., Echelmeyer, K., Harrison, W., Lingle, C., Zirnheld, S., Valentine, V., Ritchie, B. and Druckenmiller, M.: Updated estimates of glacier volume changes in the western Chugach Mountains, Alaska, and a comparison of regional extrapolation methods, J. Geophys. Res., 111(F3), doi:10.1029/2005JF000436, 2006.

Arendt, A. A., Luthcke, S. B., Larsen, C. F., Abdalati, W., Krabill, W. B. and Beedle, M. J.: Validation of high-resolution GRACE mascon estimates of glacier mass changes in the St. Elias Mountains, Alaska, USA, using aircraft laser altimetry, Journal of Glaciology, 54(188), 778–787, doi:10.3189/002214308787780067, 2008.

Arendt, A., T. Bolch, J.G. Cogley, A. Gardner, J.-O. Hagen, R. Hock, G. Kaser, W.T. Pfeffer, G. Moholdt, F. Paul, V. Radić, L. Andreassen, S. Bajracharya, M. Beedle, E. Berthier, R. Bhambri, A. Bliss, I. Brown, E. Burgess, D. Burgess, F. Cawkwell, T. Chinn, L. Copland, B. Davies, H. de Angelis, E. Dolgova, K. Filbert, R. Forester, A. Fountain, H. Frey, B. Giffen, N. Glasser, S. Gurney, W. Hagg, D. Hall, U.K. Haritashya, G. Hartmann, C. Helm, S. Herreid, I. Howat, G. Kapustin, T. Khromova, C. Kienholz, M. Koenig, J. Kohler, D. Kriegel, S. Kutuzov, I. Lavrentiev, R. LeBris, J. Lund, W. Manley, C. Mayer, E. Miles, X. Li, B. Menounos, A. Mercer, N. Moelg, P. Mool, G. Nosenko, A. Negrete, C. Nuth, R. Pettersson, A. Racoviteanu, R. Ranzi, P. Rastner, F. Rau, J. Rich, H. Rott, C. Schneider, Y. Seliverstov, M. Sharp, O. Sigurðsson, C. Stokes, R. Wheate, S. Winsvold, G. Wolken, F. Wyatt, N. Zheltyhina.: Randolph glacier inventory [v2.0]: A Dataset of Global Glacier Outlines, Global Land Ice Measurements from Space, Boulder Colorado, USA, 2012.

Beedle, M. J., Dyurgerov, M., Tangborn, W., Khalsa, S. J. S., Helm, C., Raup, B., Armstrong, R. and Barry, R. G.: Improving estimation of glacier volume change: a GLIMS case study of Bering Glacier System, Alaska, The Cryosphere, 2(1), 33–51, doi:10.5194/tc-2-33-2008, 2008.

Berthier, E., Schiefer, E., Clarke, G. K. C., Menounos, B. and Rémy, F.: Contribution of Alaskan glaciers to sea-level rise derived from satellite imagery, Nature Geoscience, 3(2), 92–95, 2010.

Bindschadler, R.: A numerical model of temperate glacier flow applied to the quiescent phase of a surge-type glacier., Journal of Glaciology, 28(99), 239–265, 1982.

Bindschadler, R., Vornberger, P., Blankenship, D., Scambos, T. and Jacobel, R.: Surface velocity and mass balance of ice streams D and E, West Antarctica, Journal of Glaciology, 42(142), 461–475, 1996.

Bruhn, R. L., Pavlis, T. L., Plafker, G. and Serpa, L.: Deformation during terrane accretion in the Saint Elias orogen, Alaska, Bulletin of the Geological Society of America, 116(7-8), 771–787, 2004.

Bruhn, R.L., J. Sauber, M.M. Cotton, T.L. Pavlis, T.L., E. Burgess, N. Ruppert, R.R. Foster. (2012), Plate margin deformation and active tectonics along the northern edge of the Yakutat Terrane in the Saint Elias Orogen, Alaska and Yukon, Canada, Geosphere, in press.

Chris Larsen Photography - Bering Glacier - April 4, 2011: http://www.gps.alaska.edu/chris/images/Bering_2011.4.11/index.html, last access: 17 January 2012.

Cuffey, K. M. and Paterson, W. S. B.: The physics of glaciers, fourth edition, 4th ed., Academic Press., 2010.

Dolgushin, L. D. and Osipova, G. B.: Balance of a surging glacier as the basis for forecasting its periodic advances, Mater. Glyatsiologicheskikh Issled. Khronica Obsuzhdeniya, 32, 260–265, 1978.

Echelmeyer, K. A., Harrison, W. D., Larsen, C. F., Sapiano, J., Mitchell, J. E., Demallie, J., Rabus, B., Adalgeirsdóttir, G. and Sombardier, L.: Airborne surface profiling of glaciers: A case-study in Alaska, Journal of Glaciology, 42(142), 538–547, 1996.

Fatland, D. R. and Lingle, C. S.: Analysis of the 1993-95 Bering Glacier (Alaska) surge using differential SAR interferometry, Journal of Glaciology, 44(148), 532–546, 1998.

Fatland, D. R. and Lingle, C. S.: InSAR observations of the 1993-95 Bering Glacier (Alaska, U. S. A.) surge and a surge hypothesis, Journal of Glaciology, 48, 439–451, doi:10.3189/172756502781831296, 2002.

Gray, A. L., Mattar, K. E., Vachon, P. W., Bindschadler, R., Jezek, K. C., Forster, R. and Crawford, J. P.: InSAR results from the RADARSAT Antarctic mapping mission data: estimation of glacier motion using a simple registration procedure, in International Geoscience and Remote Sensing Symposium (IGARSS), vol. 3, pp. 1638–1640, 1998.

Harrison, W. D. and Post, A. S.: How much do we really know about glacier surging?, Annals of Glaciology, 36, 1–6, 2003.

Heinrichs, T. A., Mayo, L. R., Echelmeyer, K. A. and Harrison, W. D.: Quiescent-phase evolution of a surge-type glacier: Black Rapids Glacier, Alaska, U.S.A, Journal of Glaciology, 42, 110–122, 1996.

Herzfeld, U. C. and Mayer, H.: Surge of Bering Glacier and Bagley Ice Field, Alaska: an up date to August 1995 and an interpretation of brittle deformation patterns, J. Glacio., 43(145), 427–434, 1997.

Kamb, B.: Glacier surge mechanism based on linked cavity configuration of the basal water conduit system, Journal of Geophysical Research, 92(B9), 9083–9100, doi:10.1029/JB092iB09p09083, 1987.

Kamb, B., Raymond, C. F., Harrison, W. D., Engelhardt, H., Echelmeyer, K. A., Humphrey, N., Brugman, M. M. and Pfeffer, T.: Glacier surge mechanism: 1982-1983 surge of Variegated Glacier, Alaska, Science, 227(4686), 469–479, doi:10.1126/science.227.4686.469, 1985.

Koenig, L., Martin, S., Studinger, M. and Sonntag, J.: Polar Airborne Observations fill gap in satellite data, Eos Trans. AGU, 91(38), PAGE 333, doi:201010.1029/2010EO380002, 2010.

LeBlanc, L.: Icequakes and Ice Motion: A time-series analysis of the dynamics of the Bering Glacier, Alaska, M.S. thesis, Geophysical Institute, University of Alaska Fairbanks, Fairbanks, Alaska, 2009.

Maronna, R. A.: Robust statistics: theory and methods, J. Wiley, Chichester, England, 2006.

METI and NASA: ASTER GDEM 2.0, Pasadena, CA, 2011.

Michel, R. and Rignot, E.: Flow of Glaciar Moreno, Argentina, from repeat-pass Shuttle Imaging Radar images: Comparison of the phase correlation method with radar interferometry, Journal of Glaciology, 45(149), 93–100, 1999.

Meier, M. F. and Post, A. S.: What are glacier surges?, Can. J. Earth Sci., 6(4), 807–817, 1969.

Molnia, B.: Glaciers of North America -- Glaciers of Alaska, in: Satellite image atlas of glaciers of the world, U.S. Geological Survey Professional Paper 1386-K, edited by R. S. Williams and J. G. Ferrigno, p. 525, 2008.

Molnia, B. and Post, A.: Holocene history of Bering Glacier, Alaska: a prelude to the 1993–1994 surge: Physical Geography, vol. 16, pp. 87–117, 1995.

Molnia, B. and Angeli, K.: Comparison of the 2008-2011 and 1993-1995 Surges of Bering Glacier, Alaska, AGU Fall Meeting, San Francisco, CA, C11B-0675, 2011.

Nye, J. F.: A method of determining the strain-rate tensor at the surface of a glacier, J. Glacio., 3(25), 409–419, 1959.

Plafker, G.: Regional geology and petroleum potential of the northern Gulf of Alaska continental margin, in Regional geology and petroleum potential of the northern Gulf of Alaska continental margin, edited by D. W. Scholl, A. Grantz, and J. G. Vedder, pp. 229–268, Circum-Pacific Council for Energy and Mineral Resources, Houston, TX, 1987.

Post, A.: Periodic surge origin of folded medial moraines on Bering piedmont glacier, Alaska, Journal of Glaciology, 11(62), 219–226, 1972.

Raymond, C. F.: How do glaciers surge? A Review, J. Geophys. Res., 92(B9), 9121–9134, 1987.

Raymond, C. F. and Harrison, W. D.: Evolution of Variegated Glacier, Alaska, U.S.A Prior to its surge, J. Glacio., 34(117), 154–169, 1988.

Röthlisberger, H.: Water pressure in intra- and subglacial channels, Journal of Glaciology, 11, 177–203, 1972.

Roush, J. J., Lingle, C. S., Guritz, R. M., Fatland, D. R. and Voronina, V. A.: Surge-front propagation and velocities during the early-199395 surge of Bering Glacier, Alaska, U.S.A., from sequential SAR imagery, Annals of Glaciology, 36, 37–44, doi:10.3189/172756403781816266, 2003.

Strozzi, T., Luckman, A., Murray, T., Wegmuller, U. and Werner, C. L.: Glacier motion estimation using SAR offset-tracking procedures, Geoscience and Remote Sensing, IEEE Transactions on, 40(11), 2384–2391, doi:10.1109/TGRS.2002.805079, 2002.

Turrin, J., Forster, R., Bruhn, R. L. and Sauber, J. M.: Velocity, slope change, and structural control of the 2008-2011 surge of Bering Glacier, Alaska, from a time-series of Landsat-7 ETM+ imagery, San Francisco, CA., C53B-0671, 2011.

# CHAPTER 3[2]

# AN INVERSE RELATIONSHIP BETWEEN SUMMERTIME MELT AND WINTERTIME FLOW VELOCITY ON GLACIERS IN ALASKA

## 3.1 Abstract

Understanding long-term ice dynamic response to climate change remains of the utmost importance with respect to constraining sea level rise estimates for 2100. Spring and summertime melt rates have been found to exert significant impacts on flow velocity while, wintertime velocities have been assumed to represent unvarying background flow speeds. Here we show that wintertime flow velocities of glaciers in Alaska are not only variable but are inversely correlated with preceding summertime positive degree days. We propose that this relationship is the result of a negative feedback mechanism. Increased meltwater production enlarges subglacial conduit systems that are more effective at discharging water from subglacial cavities. As cavities close in the fall, less remaining water reduces bed separation during winter and thus engenders slower sliding velocities. This mechanism exerts a secondary control on glacier surging; anomalously

[2] Chapter 3 is a manuscript in revision stage for publication in Nature Communications. As stated in the Nature journals policy on duplicate publication, "The Nature journals are happy to consider submissions containing material that has previously formed part of a PhD or other academic thesis."

warm summers could lead to longer intervals between surge events. Also, this mechanism likely acts in other mountain glacier regions and in Greenland and thus could have significant implications with regards to ice dynamic changes in a changing climate. If this stabilizing mechanism persists, increases in summertime temperatures could result in a gradual slowing of land terminating ice, thus providing a mechanism that could slightly slow projected mass loss from land terminating ice on mountain glaciers and in Greenland.

## 3.2 Introduction

Variations in glacier sliding velocities are modulated by the existence of pressurized subglacial water, which reduces the shear strength of the glacier bed (Lliboutry 1968). In temperate glacier environments, subglacial water comes primarily from surface melt that penetrates the full glacier thickness through vertical pathways and is eventually discharged out the glacier terminus by moving along the ice/bed interface. The extent to which this water can increase sliding velocity depends on whether the discharge capacity of the subglacial drainage system is able to accommodate incoming meltwater, thus preventing backup of water in the vertical pathways and pressurization of water throughout the glacier bed surface (Bartholomaus, Anderson, and Anderson 2008; Bartholomaus, Anderson, and Anderson 2011). The discharge capacity of subglacial drainage system changes rapidly due to complex interactions between the closure of pathways due to ice creep, water pressure, and heat dissipation from the water (Kamb 1987). In general, the subglacial system will adjust – over time – to accommodate the incoming water but not more. Hence, rapid increases in water input due to summertime

diurnal temperature changes, rainfall, and synoptic weather patterns leads to backup of water within the subglacial drainage system, pressurization and acceleration of basal sliding. An important implication of these dynamics – still under question (Sundal et al. 2011; Truffer, Harrison, and March 2005; Van de Wal et al. 2008) – is whether a gradually warming climate would increase basal sliding velocities over the long term. Higher spring/summertime flow velocities in Greenland have been shown to scale with higher spring/summertime positive degree days (PDDs) on interannual timecales (Zwally et al. 2002) and on shorter timescales (Joughin et al. 2008). When this positive relationship between summer melt and sliding velocity is incorporated into a parameterized sliding law in a flow model, the increase in sliding leads to a 10 – 25% increase in Greenland's mass loss by 2100 (Parizek and Alley 2004). But since the subglacial system can adjust to accommodate more water over time, it is unclear if this mechanism would lead to long-term increases in sliding velocities. Long-term analyses of changes in flow velocities have actually indicated a slight slowing of velocities in Greenland (Van de Wal et al. 2008) and in mountain glaciers (Heid and Kääb 2011).

Slowing velocities could be a consequence of thinning and reduction in driving stress (Heid and Kääb 2011) but there is another potential mechanism at play—a negative feedback between winter velocities and summertime melt. This mechanism was first proposed by Truffer et al., (2005) who found lower mean annual velocity in years of high summertime runoff on Gulkana Glacier, Alaska. They suggested that more summertime runoff could produce a more efficient drainage system that is more effective at evacuating water from the subglacial system in the fall. As a result, when the drainage system begins to seal off in the fall, less water remains stuck at the bed and thus more of

the ice is able to come in contact with the bed by winter, and hence slower fall and winter velocities ensue.

This dynamic, however, has not yet been observed elsewhere and if it is common, it could provide a negative feedback with climate warming (slower winter velocities with more melt) that would oppose potential acceleration in spring and summer. Herein, we aim to investigate this possibility in Alaska, by comparing regional wintertime glacier velocities to interannual changes in preceding summertime temperatures.

### 3.2.1 Geographic Setting

Alaska glaciers are contributing as much to sea level rise (SLR) as Greenland – accounting for 20% of the new water SLR worldwide (Meier et al. 2007). In south central Alaska, tidewater dynamic mass losses are contributing a volume loss that is ~75% of the net mass loss (Burgess, Forster, and Larsen 2013). Dynamic processes in lake terminating glaciers are also important. In southeast Alaska, mass losses from lake terminating glaciers actually exceeded rates from tidewater glaciers (Larsen et al. 2007). Here we examine glaciers in the Wrangell, St. Elias, Chugach, Kenai and Central Alaska ranges, which include about 56,000 $km^2$ of glacier ice (61% of the greater Alaska area) (Arendt et al. 2012) (Fig. 3.1). Throughout this region, the climate varies greatly due to large gradients in continentality. An extremely wet maritime climate dominates in the Kenai mountains as well as the south side of the Chugach and St. Elias Ranges. There, accumulation rates can exceed ~5 m. w. eq. $a^{-1}$, ablation rates can reach ~12 m. w. eq. $a^{-1}$ (Pelto et al. 2008) and rainfall occurs at low elevations even in winter. On the north side of the Chugach and St. Elias Mountains the climate becomes increasingly continental,

with greater seasonal and diurnal temperature variability and lower accumulation rates (Heinrichs et al. 1996). This trend continues northward to the Wrangell Mountains and Alaska Range. As a result, glaciers closer to the southern coast require higher balance velocities to offset higher specific mass balances; this pattern is observed (Burgess, Forster, and Larsen 2013). In fact, more than half of the total downstream ice flux throughout our study region comes from only 12 glaciers that all have high elevation accumulation zones in proximity to the southern coast (Burgess, Forster, and Larsen 2013).

Glaciers in the study area exhibit an extraordinary spectrum of interesting ice dynamic behaviors. Some of the largest examples of catastrophic tidewater retreat occurred here, including Columbia Glacier (Krimmel 2001; O'Neel et al. 2005) and Icy Bay (Porter 1989). This region also has the highest concentration of surge type glaciers in the world – over 200 (Post 1969); including some of the most studied, such as Variegated Glacier, Bering Glacier, and Black Rapids Glacier (Burgess, Forster, Larsen, and Braun 2012; Fatland and Lingle 2002; Heinrichs et al. 1996; B. Kamb et al. 1985; Raymond and Harrison 1988). The most likely explanation for the high concentration of surge type glaciers is the majority of the glaciers are situated on faulted and/or highly friable bed surfaces (Post 1969). As a result, glacier erosion rates in the Wrangell/St. Elias mountains are an order of magnitude higher than most other regions world wide (5-60 mm $yr^{-1}$) (Hallet, Hunter, and Bogen 1996). Thus, glaciers in the Wrangell/St. Elias mountains likely have an unusually large supply of deformable sediment at the bed, which can facilitate rapid basal sliding (Cuffey and Paterson 2010). Here, we examine the collective velocity variations along 189 glacier profiles shown in Figure 3.1.

### 3.2.2 Glacier Sliding Background

Rapid changes in flow velocity are the result complex dynamics occurring at the glacier bed surface. A brief review of these mechanisms is necessary as is discussion of how such mechanisms may vary in time and space. Flow velocity is controlled by the speed at which the glacier is able to maintain force balance between the driving stress (the downstream component of gravitational pull) and resistive stresses including shear stress supported on the bed and sidewalls and internal stresses within the ice. Glaciers flow through a combination of internal deformation of ice and basal sliding. For temperate ice (dominant in Alaska), the rate of internal deformation does not change appreciably over the timescales addressed in this study, thus will not be discussed further. The rate of basal sliding, however, can change rapidly in space and time.

The rate of basal sliding is broadly controlled by the bed surface topography, the existence/type/thickness of deformable sediment and englacial debris. These three controls are unvarying on short timescales but contribute to the differences in flow behavior on different glaciers and at different locations on the same glacier. Bed roughness provides resistance to glacier flow by inducing pressure anomalies on the stoss (upglacier) and lee sides of bedrock bumps that oppose basal shear stresses. In classic Weertman sliding, the sliding velocity varies inversely to the fourth power of bed roughness; thus rougher bed surfaces massively resist basal sliding (Weertman 1957). Englacial debris also retards basal sliding. Pure ice at the pressure melting point is generally assumed to support no local shear stresses when sitting on bedrock. But basal ice is rarely pure and is often filled with clasts of all sizes that can support considerable

shear stress when dragged across a glacier bed (Hallet 1979). The concentration of englacial clasts significantly affects sliding velocity as does the basal melt rate, which affects the contact force of clasts on the bed. In a field test, at Engabreen Glacier, Norway, a granite plate positioned at the glacier bed sustained extremely high basal shear stresses of 300 – 500 kPa due to basal melting and englacial clasts (Cohen et al. 2005; Iverson et al. 2003).

The existence of sediment under the glacier ice can add to the sliding rate though deformation and shearing within the sediment (Boulton and Jones 1979; Boulton 1979). In the absence of any bedrock at the bed, if the basal shear stress exceeds the yield stress of the sediment, the rate of sliding can increase indefinitely without any corresponding increase in resistive shear stress. As a result, sediment deformation can occur at extremely fast rates, which leads to the fast flow observed on surging glaciers and ice streams (Cuffey and Paterson 2010). However, sediment deformation only occurs if high pressure water exists in sediment pore spaces; thus subglacial water pressure is a key control on this mechanism and is highly variable in time and space.

While the rate of basal sliding is extremely sensitive to bed roughness, englacial debris and sub glacial sediment, these parameters are generally invariant on timescales shorter than hundreds of years. It is the existence of pressurized water at the glacier bed that not only makes basal sliding a highly dynamic process but connects basal sliding processes with climate. Water enters the subglacial system by descending through vertically oriented channels (moulins) from the glacier surface, if water backs up in moulins to the glacier surface, the water pressure can exceed the ice overburden pressure because it has a higher density. The term "effective pressure" refers to the difference

between the water pressure and the ice overburden pressure and is a primary control in most sub glacial dynamics. Once at the bed, pressurized water can reduce the mean shear stress that the bed is capable of supporting through a variety of mechanisms (Iken and Bindschadler 1986; Iken and Truffer 1997). This causes the glacier to accelerate until additional resistive stresses bring the glacier back into force balance. Water facilitates basal sliding in both hard bed and deformable bed environments but does so through different mechanisms.

#### 3.2.2.1 Role of Water in Basal Sliding

For the case of bedrock beds, water moves though two types of pathways: distributed drainage networks and conduits (R channels). Both pathways can exist in steadystate given specific conditions and can coexist under the same glacier. Barring any existing drainage network under a glacier, when water reaches the bed via a moulin it can spread across a glacier bed anywhere the water pressure exceeds the local normal stresses exerted by ice overburden. The pressure at which this occurs is termed the separation pressure and is variable on a rough bed surface. Areas on the lee sides of bedrock bumps have lower local normal ice overburden pressures, thus water tends to accumulate in cavities in the lees of bumps. If the cavities can be connected though narrower orifices, water can spread throughout the bed. This drainage system is termed a distributed hydrologic system. As water spreads across the bed into many cavities, the result is widespread separation of the glacier ice from the bed surface; this increases sliding rate in multiple ways. Initially, as water volume expands lee cavities, ice is displaced downstream leading directly to acceleration. This occurs only when water storage at the

bed is increasing and cavities are expanding. Acceleration also occurs because bed separation smoothens out the bed, which reduces resistive stresses that arise from pressure anomalies on stoss and lee bed slopes. Finally, acceleration also occurs because less ice contact with the bed means less area to support local shear stresses.

Connectivity between cavities in a distributed system is critical to supporting fast basal sliding. If bed separation increases in one area, isolated cavities will drop in pressure and thus will act as sticky spots that retard accelerated sliding (Iken and M. Truffer 1997). Maintenance of a widespread separated bed and accelerated velocities requires water pressures and connectivity to remain high, which means water input to the subglacial system must be able to keep up with increasing storage volume as cavities expand. Also, the volume of water exiting the subglacial system cannot exceed the amount entering, or else pressure will drop and the cavities and orifices will close rapidly.

This brings up the issue of how water input from the glacier surface is transferred through and exits the subglacial system. Water discharge though a distributed system moves though thousands of orifices whose crosssectional dimensions are small ($<<$ 1 m), hydrological gradients are low and thus water flow velocities are slow. Consequently, orifices and cavities remain open primarily through high water pressure opposing creep closure of the ice. Increased water discharge through the orifices can only be attained through increasing basal water pressures and thus increasing bed separation and sliding. However, as discharge through any one pathway increases, heat produced through friction and viscous dissipation are able to melt more ice on the ceiling. Once a critical threshold is reached the melt rate can exceed the rate of creep closure and the pathway can expand (Barclay Kamb 1987), allowing greater discharge under lower water pressure.

Such a pathway is called a conduit or Röthlisberger/R channel and represents the second fundamental subglacial drainage mechanism. A critical feature of R channels is, in steady state, discharge is inversely related to pressure (Röthlisberger 1972). Therefore, large channels with high discharge can exist at low water pressures and thus will draw water away from smaller channels. Most importantly, low pressure in large channels will draw water away from distributed systems, forcing their closure, along with a decrease in bed separation and water pressure and a deceleration of basal sliding.

In soft bed environments, water drainage system dynamics are very poorly understood. In environments like Alaska, there is too much water to discharge though the intergranular pore space of till, thus larger pathways must exist. In mountain glacier environments, water probably moves through a combination of R channels, Nye Channels (channels cut into the sediment though erosion) and/or a distributed macro-porous horizon at the bed (Cuffey and Paterson 2010). If R channels do exist, they can exist at lower pressure and high discharge as they do in hard bed environments, thus they will pull water from the till pore space as with distributed drainage systems in hard bed environments. Since the shear strength of till is highly dependent on the effective pressure, R channels have a similar slowing effect in deformable bed environments.

What controls which system (R channel/distributed) exists and when and where do they exist? The first factor to consider is when water leaves either system (pressure drops to atmospheric), ice creep closes openings extremely fast if under thick ice. For example, under Glen's Law, assuming temperate ice ($A = 24\times10^{-25}$, $n = 3$), a semicircular tunnel of radius $R$ will close at rate of 4%, 34% and 100% of $R$ per day at depths of 200, 400, and 570 meters, respectively. Thus a continuous supply of water is necessary to keep cavities

and conduits open. Since little water is available during fall and winter, conduits close and cavities disconnect and close. Eventually, water trapped within isolated cavities rises to the separation pressure causing gradual and slight acceleration in late fall and winter. By spring, most conduits and orifices have closed (except where the ice is shallow), but a new influx of water from surface melt allows a distributed system to begin to expand and connectivity to increase, causing bed separation and sharp acceleration. Over the course of the spring and summer, high water inputs force expansion of the distributed system and the development of an arborescent conduit system, increasing its total throughput. Once a conduit system is established, pressure in the distributed system drops and sliding decreases. Large volumes of water can now be transferred though the system rapidly at low pressure in the conduits. The seasonal cycle repeats itself causing a seasonal cycle in sliding velocity.

How can climate control variations in velocity? Given that conduits can expand to accommodate high fluxes of water, higher average summertime temperatures do not necessarily cause acceleration (though some findings in Greenland contradict this statement (Zwally et al. 2002)). Rather, it is rapid fluctuation in water input that causes acceleration (Bartholomaus et al., 2008). Increases in water input overload the established conduits. This causes water to back up, pressurize and spread out into the distributed system temporarily while the conduit system expands. In winter, most studies have assumed that glaciers settle back to a consistent base speed, often termed "wintertime background velocity" that represents sliding velocity in the absence of water inputs. But it is likely that changes in flow velocity can happen in winter. On Gulkana Glacier, Alaska, Truffer (2005) found lower mean annual velocity in years of high

summertime runoff. He suggested that higher summertime runoff produces a more extensive conduit system that was more effective at evacuating water from the distributed system. As a result, when cavities in the distributed system begin to seal off in the fall, less water is remains stuck in the cavities, thus more of the ice is able to come in contact with the bed by winter, and hence slower fall and winter velocities ensue. It is this dynamic we aim to examine on a regional scale.

## 3.3 Methods

### 3.3.1 Temporal and Spatial Domain

We examine wintertime flow velocities throughout the life of the ALOS PALSAR (© JAXA, METI, 2012) satellite, which includes data acquired between the months of December through March, 2006 – 2011 (Fig. 3.2). We compare these velocities to preceding summertime temperatures that affect meltwater input to the bed and thus perhaps the evolution of the subglacial drainage system the following winter. We will examine both wintertime seasonal and interannual velocity change. Velocities are derived over a single ALOS repeat interval of 46 days. Many of the 46-day acquisition intervals overlap at a single location but due to irregularities with PALSAR acquisition schedules and decorrelation on the glacier surface, the exact dates of acquired velocity data acquired are irregular.

Given that our observation period is only 6 years long, it is important to place the climate during these years in the context of climate on longer scales. Meteorological station data from Yakutat is shown in Figure 3.3. The mean daily minimum/maximum temperatures are slightly lower than the 1980 – present average (0.06°C and 0.36°C

lower) but are easily within expected variability. Peak summertime temperatures and cumulative positive degree days were above the 33-year mean (1980-2013) in 2006, 2010 and 2011. 2007, 2008, and 2009 were cooler than average. 2008 was an anomalously cold summer (1980-present z-score < -1.5)

Flow velocities are examined on 189 profiles that cover 126 separate glacier systems (some glaciers have profiles on multiple tributaries) shown in Figure 3.1. These profiles cover all major glaciers in the Central Alaska Range, the Kenai Mountains, the Chugach Mountains, the St. Elias Mountains and the Wrangell Mountains. These areas account of approximately 66% of the ice area throughout the greater Alaska region. Areas not included are glaciers in the Fairweather Range and Glacier Bay, the Coastal Range and the Brooks Range. Continentality changes dramatically throughout these regions. The coastal sides of the Kenai, Chugach, St. Elias, Fairweather, and Coastal ranges are extremely maritime and change rapidly to drier continental climates as one moves inland. Maritime areas have more mild temperatures, while continental areas have higher/lower temperatures in summer/winter than maritime areas. The majority of surging glaciers in the greater Alaska region exist in the Wrangell Mountains, the St. Elias Mountains and the Alaska Range. In all this study considers 23 tidewater glaciers, 13 lake terminating glaciers and 61 surging glaciers (Post 1969). Areas excluded from this study have a large number of tidewater and lake calving glaciers and very few surging glaciers. Our sample represents a wide spectrum of climatic and geologic environments that can potentially affect ice dynamic behavior and should be representative of dynamic behaviors throughout the Alaska region.

### 3.3.2 Velocity Processing

#### 3.3.2.1 Data Processing

We derive glacier velocities using SAR offset tracking methods described at length in Burgess et al. (2013). Offset tracking uses two images acquired at separate times to find the displacement of pixel patterns within both images using cross correlation (Gray et al. 1998; Michel and Rignot 1999). Raw ALOS PALSAR FineBeam data are processed to single look complex (SLC) images using GAMMA® software. Offset tracking is performed on slant range image pairs. A displacement offset is calculated at intervals of 20 x 40 pixels using an offset tracking window size of 45 x 90 pixels (nominally, 337 m x 283 m).

Calculated displacements are geocoded, topographically corrected and corrected for image coregistration using the satellite geometry and the ASTER-GDEM 2.0 (METI and NASA 2011). The ASTER-GDEM 2.0 does have significant problems with artifacts and abrupt changes in elevation due to image saturation and changing surface heights over time. The GDEM is chosen over other DEMs because it covers all of Alaska and is derived from comparatively recent data (1999 – 2011). Other elevation models are either dated (1950s) (NED-DEM), confined to south of 60° latitude (SRTM-DEM), or are prohibitively expensive (SPOT-DEM). Offset estimates located on DEM artifacts inherit small errors in their geolocation. Given that artifacts are relatively sparse and the velocity profiles used for analysis are a smoothed interpolation from many offset estimates, the artifacts have little or no effect on our results. Topographic correction is performed using concepts of radargrammetry using a method (Burgess, Forster, and Larsen 2013) that is insensitive to errors in the GDEM. Next, we remove any erroneous offset vectors that

were generated due to false correlation peaks using a highly effective filtering routine (Burgess, Forster, Larsen, and Braun 2012). We correct image coregistration offsets using the Randolph Glacier Inventory (RGI1.0) (Arendt et al. 2012) and ASTER-GDEM to identify areas that exist on stable ground (off glacier and above 0 m elevation). The stable ground offset field is modeled using a second order polynomial function fit using an iterative least squares method. Residuals from each iterative fit with sigma values greater than 3.0, 2.5 and 2.0 are eliminated allowing the model to gradually improve. The final polynomial is subtracted from all offsets, which provides ice displacements on glacier and uncertainty estimates off glacier.

Within each image pair, the distribution of off glacier offsets has extreme outliers due to occasional erroneous correlation matches; thus we quantify our uncertainties in each image pair by calculating the mean off glacier vector and a normalized median absolute difference estimate (MADn, robust equivalent to a 1 standard deviation uncertainty). Both values are shown in Figure 3.4 for 306 image pairs. Overall, biases are generally less than 0.1-0.2 cm $day^{-1}$ and MADn values (1-$\sigma$ equivalent) below 4 cm $d^{-1}$. Since this study will be examining changes in velocity averaged along entire glaciers (including many individual offsets), our ability to detect change in velocity should lie closer to the image wide bias estimates.

Finally, to reduce uncertainties further, each scene is manually inspected and any remaining offset vectors that are not pointing in the direction of flow or are anomalously high/low are removed. Offset vectors are then gridded to a 30 m grid using a second order polynomial regression with a search radius of 900 m. We require a minimum of six values within at least four of eight radial sectors surrounding a grid point to interpolate a

value. This method is effective at smoothing out small differences in neighboring vectors.

3.3.2.2 Analytical Methods

In order to address temporal changes in flow velocity, we extract velocity data from all available grids along each manually digitized profile. For each profile, we obtain, on average, about 12 observations (ranging from ~4 – 30 due to data availability) of velocity at different times but not necessarily discrete times due to overlapping acquisitions. Velocity along each profile is extracted from the grids every 30 m using bilinear interpolation. On longitudinal profiles, we extract velocity magnitude. On lateral profiles, we extract the component of the velocity vector perpendicular to the profile; this allows for derivation of flux through a gate even if the gate is not perpendicular to the flow itself. The polynomial regression used to derive the gridded data occasionally produces spikes at the edges of data extents. These spikes are identified in each profile with a moving median filter and changed to a missing data value. Each profile is then smoothed using a Gaussian kernel with a 1-sigma width of 90 m.

In order to make velocity changes comparable between glaciers, we convert absolute velocity along each profile to velocity anomalies. This requires a "mean" or representative velocity profile, from which, each acquisition pair can be compared. However, simply calculating the mean is ineffective because occasional erroneous offsets and other unexplained anomalies on the glacier surface can result in large spikes along some profiles that affect the "mean" profile. To address this issue, we identify profiles with such problems by subtracting each profile from itself after being convolved with a

boxcar kernel. Profiles with large differences are flagged and removed and the rest of the profiles are used to derive a mean profile. This method is extremely effective except for rare cases where we have broken up and very little data on glaciers that have drastic velocity changes (e.g., Allen Glacier). But even in these few cases, these methods prove relatively robust. Velocity anomalies are then derived by dividing data from each acquisition interval by the mean profile. This results in a percent change in velocity from the mean; this value is thus comparable between large/fast and small/slow moving glaciers.

We examine seasonal variations in velocity by assigning a single midpoint date to each velocity pair, and then linearly interpolating each velocity profile through time over the winter season (time as the independent variable). The time derivative thus represents the rate of change in velocity between the midpoint dates of all image pairs processed for a single season. We use this value to examine temporal change in velocity seasonally. This method assumes that the changes in wintertime velocity within a single season are smooth between each velocity observation. In winter, this is an acceptable assumption because wintertime velocities do not change abruptly as they do in summer (Fudge et al. 2005; Harper et al. 2005; Zwally et al. 2002). Surging and tidewater dynamics do offer exceptions to this rule (Raymond 1987) and in these cases we are only able to address acceleration/deceleration over monthly or longer timescales.

Examining interannual changes requires caution because we rarely have observations of velocity at the same exact date each year. Again, wintertime velocities aren't believed to change rapidly but any observed interannual changes must be separated from seasonal differences in acquisition dates from year to year. We address this problem by only

considering velocity observations with a midpoint date within only January (for our regressions and tests of significance), thus requiring at least some overlap in dates from year to year. The velocity maps shown in the following include data from December – March for better spatial coverage, but have values very similar to maps from derived from only January data. In addition, we compare the magnitude of the interannual variability with the magnitude of wintertime seasonal variability. As will be seen later, the wintertime seasonal variability is usually small compared to interannual changes.

### 3.3.3 Climate Data

We derive a relative measure of total summertime meltwater input to glacier beds using PDDs. PDD models are a simple and effective method to derive estimates of surface ablation on glaciers (Hock 2003; Johannessen et al. 2005; Radić and Hock 2011). Thus, it is reasonable to use a PDDs as a proxy proportional for meltwater runoff. Regional estimates of degree day factors (DDFs) for Alaska (Arendt, Walsh, and Harrison 2009) generally agree with DDFs derived on glaciers elsewhere (Radić and Hock 2011). But since we are relating water input to interannual changes in flow velocity, only a relative measure of summertime meltwater input is needed, not absolute volume of water. Thus, this method should be relatively robust as long as our temperature data do not have changing biases from year to year. Liquid precipitation also contributes to meltwater input and is not accounted for here. But except for perhaps the most maritime areas in Alaska, water input to the bed is dominated by melt (Motyka et al. 2003) thus PDDs should still provide a robust proxy for the variability of meltwater input from year to year.

To derive meltwater input, PDDs estimates are needed on all 186 glaciers within our study area. In these areas, meteorological station data are either nonexistent or extremely distant and existing stations are usually subject to frequent malfunctions and local drainage effects etc. Consequently, we derive temperature using ERA-Interim data (Uppala et al., 2005) downscaled to a 1 km grid and validated against station data where possible. ERA-Interim air temperature and geopotential height data are retrieved from 2006 to 2011 at pressure levels from 500 to 1000 mb. ERA-Interim includes an estimate of air temperature to 1000 mb, even when the model terrain is above this level (for purposes of deriving sea level pressure). Temperatures below the model terrain generally increase along an environmental lapse rate of ~6.5 °C $km^{-1}$. Thus without better options, these data can be reasonably used to derive temperature for terrain that is below the coarsely resolved ERA model terrain. All pressure levels are bilinearly interpolated onto a 1 km grid to match a 1 km elevation model obtained from downsampling the ASTER GDEM 2.0 (METI and NASA 2011). Surface air temperature is then extracted at each pixel using elevations from the 1 km DEM and the interpolated temperature and geopotential height fields. A cumulative PDD estimate is then calculated for each 1 km pixel for the summers of 2006 to 2010. Finally, the mean PDD value along each glacier profile is derived and used as our seasonal meltwater input proxy.

We validate our the gridded temperature and PDD datasets by comparing it against measured air temperatures at 12 meteorological stations scattered throughout the study region and shown in Figure 3.1 (Horel et al. 2002). Example, comparisons with four stations of varying climates: PAYA, HRDA2, PAZK and TKLA2 are shown as Figures 3.5-3.5, respectively. Our gridded temperature has difficulty in low elevation coastal

areas such as PAYA (Fig. 3.5), primarily because fall, winter and springtime temperatures are very close to zero. Thus, small differences between the downscaled ERA and station data lead to large differences in PDDs. This problem quickly dissipates however as one moves inland or up in elevation. HRDA2 (Fig. 3.6) is positioned on the Harding Icefield in an extremely maritime location at an elevation of 1311 m. It is the only station available that is immediately adjacent to large glaciers. At HRDA2, we see much better agreement, little seasonal variability in bias, and very well replicated PDDs. PAZK (Fig. 3.7) is at an intermediate continental location, in a low lying area north of the Chugach mountains. Here biases are seasonally dependent. The downscaling method overestimates significantly in winter, likely because of cold air pooling. But in summer, when temperatures are above freezing, biases are minimal and our downscaling method proves effective at estimating PDDs. TKLA2 (Fig. 3.8) is at a much more continental position on the north side of the Central Alaska Range. The downscaling biases are seasonally higher in winter as with PAZK but less so, likely because the station is not positioned in a low-lying basin like PAZK, thus isn't as vulnerable to cold air pooling. Still, summertime temperatures are well simulated and our PDD estimates conform to observed PDDs. Of the 12 stations, 5 have relatively complete records and are not on the immediately proximal to the coast (some are missing months of data). At these sites, we find our gridded PDD dataset has a root mean squared error of 4.9%; thus it does fairly reliable job of estimating PDDs throughout our study area. We also find that our PDD anomalies compare well to GRACE derived summertime glacier mass anomalies (data continued from Luthcke et al., (2008))

## 3.4 Results

### 3.4.1 Spatial Variations in Wintertime Velocity Change

We find that wintertime velocities are highly variable and show coherent spatial variability. Figure 3.9 shows the standard deviation of flow velocities throughout all data available from winters 2006/2007 to 2010/2011 (December – March). Since our data coverage is not temporally comprehensive, low values in Figure 3.8 do not necessarily imply flow is unvarying, rather change is simply not unobserved. It is also important to note that of all of the profiles, there are only three systems with known surge events during the period of study—Bering, South Branch of Lowell, and Ottawa (Fig. 3.9).

As can be seen, wintertime velocities vary significantly on land terminating, lake/tidewater, surging and nonsurging glaciers. Also, there is coherent broad spatial variation in the temporal variability. Variations in the Alaska Range, the Kenai, and Chugach are relatively minor compared to the changes in the Wrangell/St. Elias Mountains (Columbia is one exception). There is also a clear difference between velocities within the Wrangell/St.Elias group. Wintertime velocity change in the Wrangell Mountains is generally confined to isolated areas on a select few glaciers; most areas in the Wrangells, show little to no variation. Such a pattern is expected, as many of these glaciers are surge type, thus we would expect to see little variation on most and large variations on a select few undergoing surges or quiescent phase accelerations (Raymond 1987). However, in the St. Elias Mountains, velocity variability is high on almost all major glacier systems and occurs along the majority of each glaciers' length.

### 3.4.2 Seasonal Change

The mean rates of acceleration for all glaciers are shown over each winter in Fig. 3.10. There is a large amount of variability in wintertime acceleration. The distribution is generally skewed toward acceleration (rather than deceleration) over each winter. A few glaciers show rather large wintertime seasonal changes, which are often related to surging. During our period of interest (January), mean rates of acceleration are almost always positive but generally lie below 1 mm $d^{-2}$; median rates of acceleration generally lie below 0.5 mm $d^{-2}$. Given the limitations within this seasonal analysis and given that our absolute image uncertainty is generally 1-2 mm $d^{-1}$ (Fig. 3.4), we hesitate to associate this mean positive rate of acceleration with an observed widespread increasing trend in wintertime velocity.

Overall, wintertime seasonal changes are far smaller than the interannual changes observed on almost all glaciers. Given that the temporal distribution of data acquired in our period of interest (January) is evenly distributed in all years (Fig. 3.2) we find that our observations of interannual change in winter velocities are robust with respect to seasonal variability.

### 3.4.3 Interannual Changes in Winter Velocity

Figures 3.11 – 3.15 show velocity anomaly maps for hydrologic years of 2007 – 2011 Each figure includes two reference plots showing the temporal evolution of glacier velocity anomalies and PDD anomalies (from PAZK, Fig. 3.1). Anomalies are expressed in meters per day on the maps and as a percentage on the reference figure for clarity.

Maps include data from December – March for better visual coverage but approximate the values in January-only maps closely.

Over our period of study, the summer of 2006 had close to average total PDDs and the following winter (2006/07) had close to average mean velocities (Fig. 3.11), albeit with variations that do show spatial coherency. Almost all of the major coastal glacier systems show large negative anomalies at low elevations; these include tidewater, lake and land terminating surging glaciers. At higher coastal elevations, the Bagley Ice Valley had large positive anomalies on both the Seward and Bering Glaciers. The positive anomaly on the upper Bering is a quiescent phase acceleration event that is related to Bering's full scale surge initiation in mid-2008 (Burgess, Forster, Larsen, and Braun 2012).

The summer of 2007 had relatively higher PDDs than other years and the winter of 2007/08 had anomalously low flow velocities throughout the Chugach and Wrangell/St. Elias Mountains (Fig. 3.12). The small positive anomalies on Bering Glacier are precisely in the trigger zone where the Bering surge began to accelerate rapidly over the following fall (2008). Thus, these anomalies may represent an initial and slow start to the first phase of the Bering surge (Burgess, Forster, Larsen, and Braun 2012). It is thus noteworthy that this initial acceleration in the trigger zone of Bering is not entirely unique; many of the other low elevation coastal locations also show confined positive anomalies occurring at the same time (e.g., Seward, Agassiz, Hubbard, Martin River, Columbia, and the Harding ice field) (Fig. 3.12). These coastal positive anomalies occurred when the rest of the state had overwhelmingly negative anomalies.

The summer of 2008 was an extremely cold summer (Horel et al. 2002) (Fig. 3.13). The following winter we see a switch to large positive anomalies. At this time, the surge on Bering had begun simultaneously with a surge on Lowell, and with large accelerations throughout much of the state on all types of glaciers (land/lake/tidewater, surge/not surge). The few areas that show slight negative anomalies tend to exist in lower ablation zones with positive anomalies upstream (for example, glaciers in the Alaska Range and northern Chugach).

The summer of 2009 was relatively warm and velocity anomalies the following winter (2009/10) were mixed but averaged slightly below average (Fig. 3.14). The first stage of the Bering surge also slowed/ended. Some large positive anomalies did occur however on Seward, Lowell, Logan and Ruth Glaciers. The following summer of 2010 had approximately average PDD values. Though our velocity data are much more limited over the following winter of 2010/2011, velocity anomalies were very positive (Fig. 3.15). During this winter, Bering began the second stage of its surge (Burgess, Forster, Larsen, and Braun 2012) (from aerial visual observations; we have no velocity data on lower Bering then), this occurred in synchrony with positive velocity anomalies on Stellar, Seward and Agassiz Glaciers.

To review, over the periods 2006-2011 we see several patterns emerging. We see broad synchronicity in velocity anomalies throughout the study area, albeit with a large amount of variability. Generally, these velocity anomalies appear inversely related to PDDs from the previous summer. There is also embedded local variability. Anomalies show consistency within mountain ranges and distinct differences between ranges. There is also regional consistency specific to certain climate environments. In particular, low

elevation coastal glaciers have synchronous velocity anomalies that can vary independently from velocity anomalies throughout the rest of the state.

On an individual glacier scale, we also observe some fascinating dynamics. Some glaciers (surge and not surge type) show progressive, multiannual changes in wintertime velocity that do not necessarily have the signature of surging and do not necessarily fit within the regional trends in velocity anomalies. A potential mechanism responsible for these dynamics is discussed in Chapter 3, Section 4.

Finally, the surges of Bering and Lowell, not only occur in synchrony, but occur in synchrony with anomalies throughout the study area on all types of glaciers. Even the two staged surge on Bering fits within the regional velocity anomaly pattern. The minisurge in the accumulation zone in 2007 shows a similar velocity distribution to other coastal glaciers in the St. Elias. In 2008, we see a slight acceleration in the surge trigger zone of Bering, while other coastal glaciers show similar accelerations confined to low elevations close to their termini. Stage I of the surge ramps up during positive anomalies statewide in 2008/2009 and then slows in the winter of 2009/2010 along with slightly negative anomalies on average statewide. Finally, the larger second stage begins in 2011 along with positive anomalies elsewhere.

### 3.4.4 Relationships Between PDDs Anomalies and Velocity Anomalies

We now examine the possibility of a relationship between summertime PDDs and wintertime velocities. The average velocity anomaly for each year, along each glacier profile is plotted against the average PDD anomaly along the same profile in Figure 3.16-3.18. Since we have multiple profiles on some glaciers, we only use only the primary

longitudinal profile on each glacier to maintain independence between observations. We also only consider velocity data with a midpoint date in January to avoid seasonal variations (though determined to be small in Section 3.4.2). We also remove five outlying points (>3-σ). These include the Lowell Glacier prior and during its surge, Ottawa Glacier during its surge and Allen glacier in 2008 (data quality issue). If these values are not removed, all relationships that do not contain Ottawa remain significant with similar slopes. Ottawa began a surge between 2008/10 when velocities increased by 30 times quiescent flow; in regressions Ottawa's studentized residual was > 6-σ.

As can be seen in Figure 3.16 and Table 3.1, there is a large amount of variability. $R^2$ values are generally low, suggesting that variable bed conditions play a large role in wintertime velocities. Nonetheless, we find a highly significant negative relationship between velocity anomalies and PDD anomalies with a slope of -2.5% per 100 PDDs. Separating the data into surging and not surging glaciers (Fig. 3.17) we find more variability in the surge type glaciers, but both surging and not-surging glaciers show similar relationships that are highly significant. Separating the data into land terminating, lake terminating and tidewater glaciers, yields some interesting differences (Fig. 3.18). All of the relationships are negative and significant. The variability is higher on land terminating glaciers likely because most surging glaciers are land terminating. Interestingly, tidewater glaciers show a relationship with a higher $r^2$ and a slope of -1.1% per 100 PDDs that is significantly flatter ($p < 0.005$) than that of all glaciers. In contrast, lake terminating glaciers have a much steeper slope of -3.8% per 100 PDDs, and a relatively high $r^2$ of 0.264. The slope of the lake regression is not significantly different than all glaciers but is significantly different from tidewater glaciers ($p < 0.025$).

In attempt to illuminate the implications of these regressions, we convert the slope coefficients in each regression from units of PDDs to units of meters snow water equivalent using typical degree day factors for ice and snow (Hock, 2003; Arendt et al., 2009) (Table 3.1). From these numbers, we find an increase in summertime ablation of a single meter of water equivalent results in a 4-10% decline in wintertime velocity on average, a 2-5% decline for tidewater glaciers and a 6-15% decline for lake terminating glaciers.

## 3.5 Discussion

### 3.5.1 Mechanisms Responsible for a PDD/Winter Velocity Relationship

These results are the first to confirm that an inverse relationship between wintertime velocity and summertime melt exists on regional scales in mountain glacier environments. We suggest that this relationship exists because additional meltwater from warmer summers results in a more extensive conduit system that is effective at evacuating meltwater from a distributed system prior to cavities sealing off in the fall. As cavities continue to close, water pressure still rises to ice overburden but the lower volume of water results in less bed separation, more ice to bed contact and thus slower sliding velocities. In contrast, less meltwater production during a cool summer would result in smaller conduits that are more sparse and thus less effective at drawing hydraulic gradients towards the conduits. Without strong hydraulic gradients moving towards conduits, there is no mechanism to evacuate water left in the distributed system in the fall. The orifices between cavities close and a relatively large amount of bed separation is maintained throughout the winter.

While we find the relationship between PDDs and winter velocity to be statistically robust on a large regional scale, there is a large amount of variability; our overall model describes only ~9% of the variance (Table 3.1). But this variability also fits within the mechanism proposed. The pervasiveness of the conduit system depends not only on water input but also on the bed topography and the locations of moulins. Large moulins tend to be multiannual features. But during summer, new pathways open up and others close and existing pathways can also expand, drawing more water than previous years (Benn et al. 2009). These dynamics change the distribution of water input to the bed and change the location of the conduit network. The movement of a conduit network alters which areas will be well drained come winter and which areas will still hold water. Given spatially variable bed conditions (changing roughness, hard/soft bed), these dynamics could not only lead to the large variability we see, but could also lead to the progressive multiannual changes in wintertime velocity we observe on individual glaciers.

We also find that the inverse relationship between PDDs and wintertime velocity is significantly flatter in tidewater glacier environments. This finding is in agreement with observations in Greenland that have found less seasonal velocity variability on tidewater outlets than on land terminating ice (Joughin et al. 2008). A weaker relationship between PDDs and wintertime temperatures also makes sense given the mechanism proposed. In tidewater environments, the conduits discharge at depth in fjords, thus are not able to depressurize the bed and draw water out of distributed systems as efficiently as an outlet that is able to exit at atmospheric pressure (or in cases not at all).

It is thus interesting that the relationship between PDDs and wintertime velocity in lake environments is more than three times steeper (sig., $p < 0.025$) than tidewater

glaciers. Lake terminations are in freshwater (less dense) that may be shallower than typical fjords depths. Shallower fresh water, exerts a lower hydraulic head on subglacial system than deep water in fjords, thus would explain the difference between lake and tidewater systems. The observation that lake terminating glaciers have a steeper relationship (not statistically significant) than land terminating is more difficult to explain. Lakes can have a seasonally and annually varying depth dependent on the influx of runoff that fills the lake. This change in depth could affect the hydraulic head exerted upstream on the subglacial system. Assuming lake depth varies seasonally with a low in winter to a peak in mid summer and varies annually (higher in warmer years) we speculate one possible mechanism. The channelized system develops in spring and early summer (Schoof 2010) when lake levels are relatively low (but rising). Water is able to exit the glacier under relatively low pressure thus allowing a conduit system to develop as in a land terminating environment. But as summer continues, the rising lake level exerts a rising hydraulic head back into the channelized system. This, according to steadystate theory (Röthlisberger 1972), would maintain a relatively high pressure in the conduits and reduce the total flux, thus keeping the drainage system open longer as water input subsides. In fall, as lake levels drops due to outflow, the conduit pressure gradient would increase, pressure would drop, and flux would increase. The drainage system, held open during late summer, would be more efficient at evacuating water in fall, which would allow more ice-bed contact by winter. If this cycle is considered interannually, warmer summers would result in temporarily higher lake levels thus magnifying this effect in warmer years and enhancing previously stated mechanisms. Again, the observed difference between PDDs and winter velocity in lake and land terminating glaciers is not

statistically significant and this lake mechanism suggested is purely speculative and requires numerical evaluation.

### 3.5.2 Surge Triggering Related to Summertime PDDs

Our observation that the initiation and evolution of both stages of the Bering Glacier surge (and Lowell surge) occur in synchrony with wintertime velocity anomalies throughout the study area implies that the mechanism controlling regional wintertime velocities modulates surge evolution as well. While it is widely understood that the periodic nature of surging arises from the progressive buildup of driving stress through changing geometry, it has been suggested that external factors could exert a secondary control (Post 1960; Raymond 1987). The primary control on surging, elevated driving stress, limits the expansion of subglacial cavities and conduits through viscous heating (Kamb 1987) and thus promotes distributed systems over channelized systems.

But there is another requirement needed to trigger rapid sliding—the availability of subglacial water. Following steadystate theory of subglacial tunnels (Röthlisberger 1972) and conditions for bed separation (Bindschadler 1983; Lliboutry 1968), Raymond (1987) proposed that surges are triggered through a collapse of the conduit system when the conduit water pressure exceeds the separation pressure in neighboring cavities. Given the inverse relationship between water pressure and discharge, they propose this condition can be met with a low steadystate discharge in conduits. We thus conclude that that lower PDDs in the summer can trigger surge initiation the following winter because lower meltwater inputs lead to conduits with less discharge capacity and are thus under higher pressure in the fall than after a warm summer, thus increasingly the likelihood that

conduit pressures can exceed the separation pressure and induce widespread bed separation and rapid basal sliding.

### 3.5.3 Mechanism Persistence in a Changing Climate

Perhaps the most important issue with regards to these findings is whether this mechanism would be expected to progress in a warming climate. Gradually increasing meltwater input will be accommodated by subglacial systems with expanding capacity due to well known mechanisms (Schoof 2010). Conduits will likely get bigger and thus would be able to exist in steady state under lower pressure (Röthlisberger 1972) and will also likely become more extensive (Schoof 2010). But the extent to which these changes occur will not only depend on climate related increases in meltwater input, they will also depend on moulin locations and bed topography. Thus, furthering our understanding moulin distribution, evolution and connection to conduit systems will help to address to what extent this negative feedback would progress with a warming climate.

Granted, these dynamics are likely very different in Greenland versus in mountain glacier environments due to differences in ice thickness, bed topography, water volume, etc. Nonetheless, in Greenland there are indications that this dynamic will progress and offset springtime acceleration. In Greenland, Van de Wal et al. (2008) found mean annual velocities slowed over a 17-year period, but also found no correlation between ablation rates and mean annual velocities. This indicates that the positive/negative relationships during summer/winter largely offset one another. In fact, our proposed negative feedback mechanism between PDDs and winter velocities was also observed (though not discussed) in the landmark paper by Zwally et al. (2002), which instead focused on the

positive relationship during springtime. Over their 4 years of record, larger melt summers we followed by lower wintertime velocities. Moreover, during warmer years, the reduction in wintertime displacement was larger relative to the increase in summertime displacement. Indicating that, at least in Greenland, more warming could lead to a dominant negative wintertime velocity feedback.

## 3.6 Conclusion

We find that an inverse relationship exists between wintertime velocity and cumulative summertime melt on regional scales on glaciers in Alaska. This relationship likely exists because greater meltwater production results in a more extensive conduit system that facilitates evacuation of subglacial water in the fall and thus allows for less bed separation in winter. We expect this mechanism exists in other mountain glacier environments and in Greenland and thus could have significant implications with regards to long term ice dynamic changes in a warming climate. While this mechanism is observed (to a lesser extent) on tidewater glaciers, the effect is slight and thus will not offset tidewater retreat and other dynamics related to conditions at calving fronts.

On interannual timescales, we observe significant variability in wintertime velocities on land/lake/tidewater, surging and not-surging glaciers. While some of this variability is correlated with summertime temperatures, a lot of the variability is not and may represent unusual changes in bed conditions that are not well understood. These observations call to question the use of the term, "wintertime background velocity," as we find winter velocities vary from year to year.

We also find that the mechanism leading to regional changes in wintertime velocity also exerts a secondary control on surge initiation and evolution. This means that anomalously cold summers will help to instigate surging the following winter if the necessary glacier geometry exists.

Whether this mechanism will act to slow velocities globally and reduce the occurrence (or lengthen the interval) of surge cycles needs must be evaluated more closely. An improved understanding of the spatial distribution and connectivity between supraglacial hydrology, moulins, and the subglacial conduit system is needed to aid the development of numerical models that can appropriately address relationships between climate and ice motion. Until these relationships can be established, the contribution of dynamic mass loss in mountain glacier environments and other land terminating ice cannot be constrained.

## 3.7 Acknowledgements

E. Burgess was funded under the NASA Earth Science Space Fellowship. R. Forster and the velocity work were funded by NASA Grants NNX08AP27G and NNX08AX88G. C. Larsen was supported by NASA's Operation Ice Bridge Grant NNH09ZDA001N. The Alaska Satellite Facility provided ALOS and ERS data.

Table 3.1. Linear models for a PDD winter velocity interaction

| | Linear Coefficients | | | | | | | Melt Slope* | | |
|---|---|---|---|---|---|---|---|---|---|---|
| | | | | | | | | *DDFsnow* | *DDFice* | |
| | | | | | | | | *0.0025* | *0.006* | |
| | **Constant** | *SE - PDD Const* | **PDD Slope** | *SE - PDD Slope* | *DF* | $R^2$ | *p* | | | *Slope Different from ALL* |
| All Glaciers | 1.009 | 5.22E-03 | -2.547E-04 | 4.19E-05 | 357 | 0.09 | <0.0001 | -0.102 | -0.042 | N/A |
| Surging | 1.027 | 1.33E-02 | -2.797E-04 | 1.21E-04 | 103 | 0.05 | 0.0232 | -0.112 | -0.047 | |
| Not Surging | 1.001 | 4.89E-03 | -2.467E-04 | 3.75E-05 | 252 | 0.15 | <0.0001 | -0.099 | -0.041 | |
| Tidewater | 0.999 | 5.92E-03 | -1.134E-04 | 4.25E-05 | 49 | 0.13 | 0.01 | -0.045 | -0.019 | p<0.005 |
| Lake | 1.021 | 1.82E-02 | -3.842E-04 | 1.23E-04 | 27 | 0.26 | 0.0043 | -0.154 | -0.064 | |
| Land | 1.009 | 6.34E-03 | -2.686E-04 | 5.32E-05 | 277 | 0.08 | <0.0001 | -0.107 | -0.045 | |

**DDFs in units of m w. eq. $°C^{-1}$ $d^{-1}$*

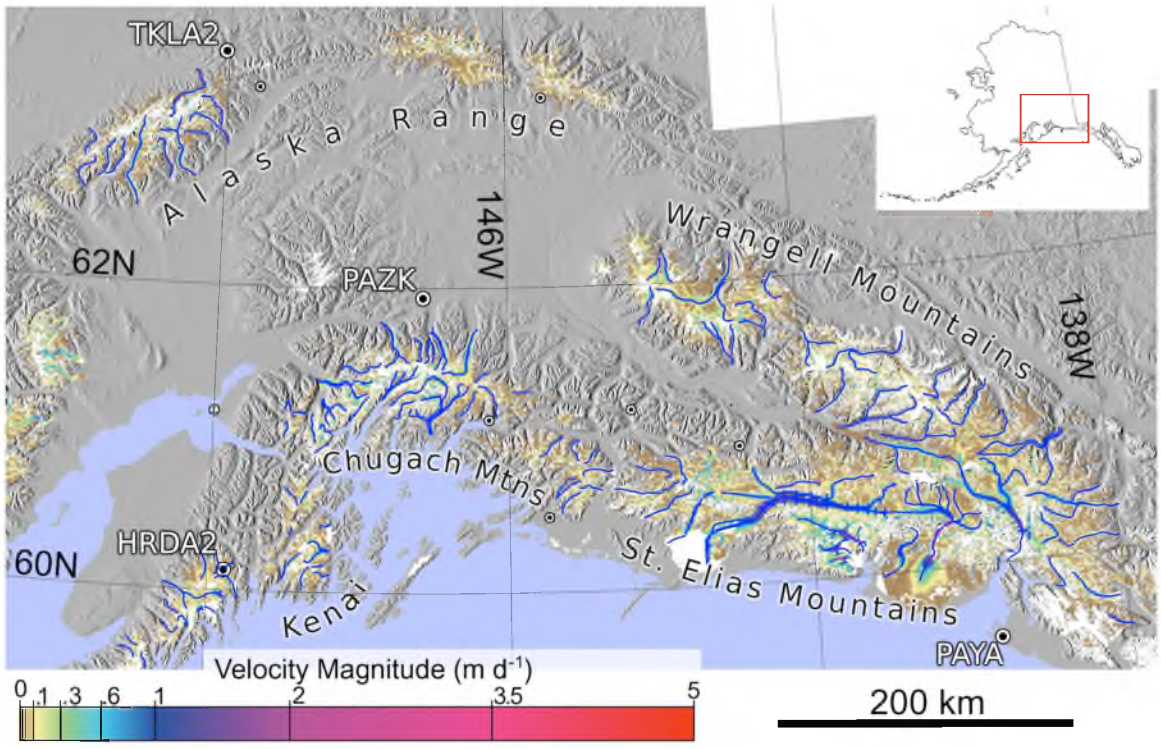


Figure 3.1. Study area including189 glacier profiles shown as blue lines. Velocity map from (Burgess, Forster, and Larsen 2013) uses a small subset of the data used here. Circles indicate meteorological stations used for PDD model evaluation. Named stations denote those discussed specifically in the text.

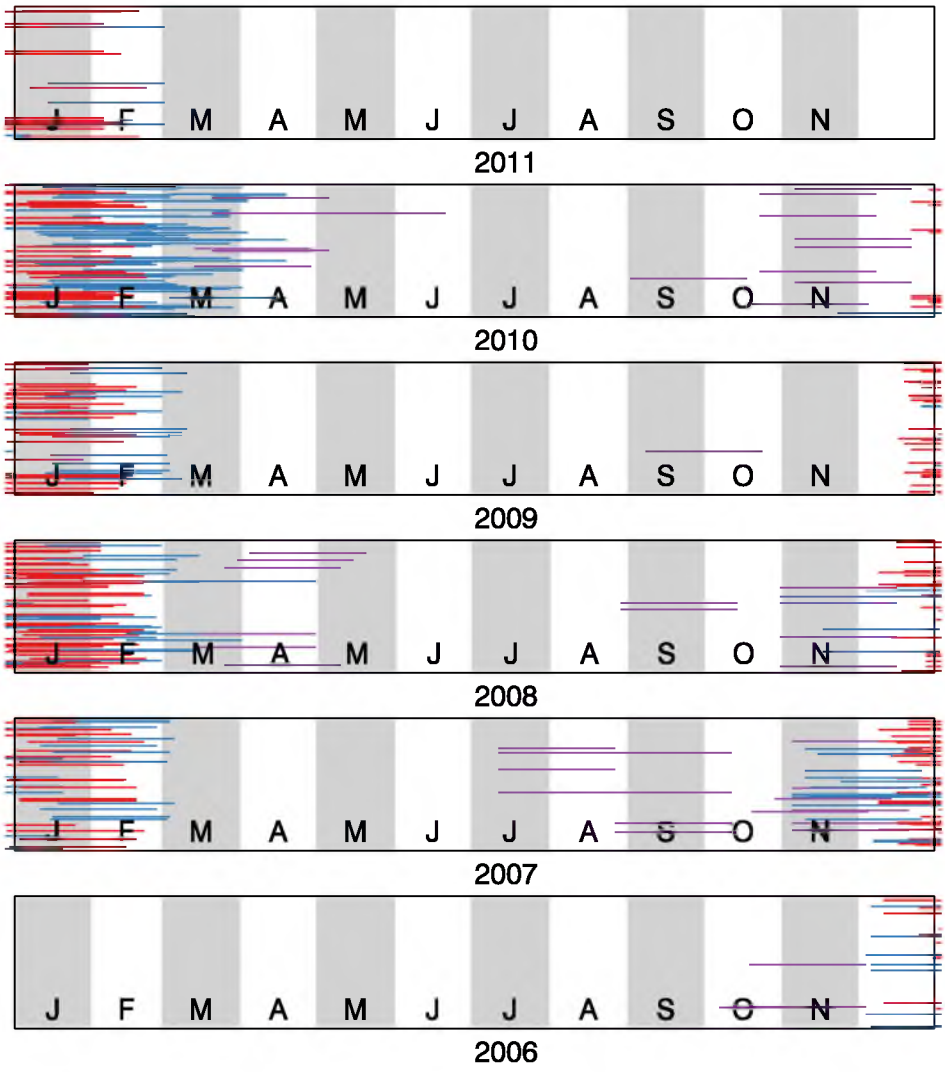


Figure 3.2. Temporal Distribution of ALOS PALSAR pairs used. Length of each line indicates the interval between the first and second acquisitions within each pair. Regressions and significance testing use only January pairs (red). Figures 3.8,3.10 – 3.14 show December – March pairs for added spatial coverage (red and blue). Seasonal evolution (Fig. 3.9) includes data from all colors in this figure. Vertical level within each year is randomized for clarity.

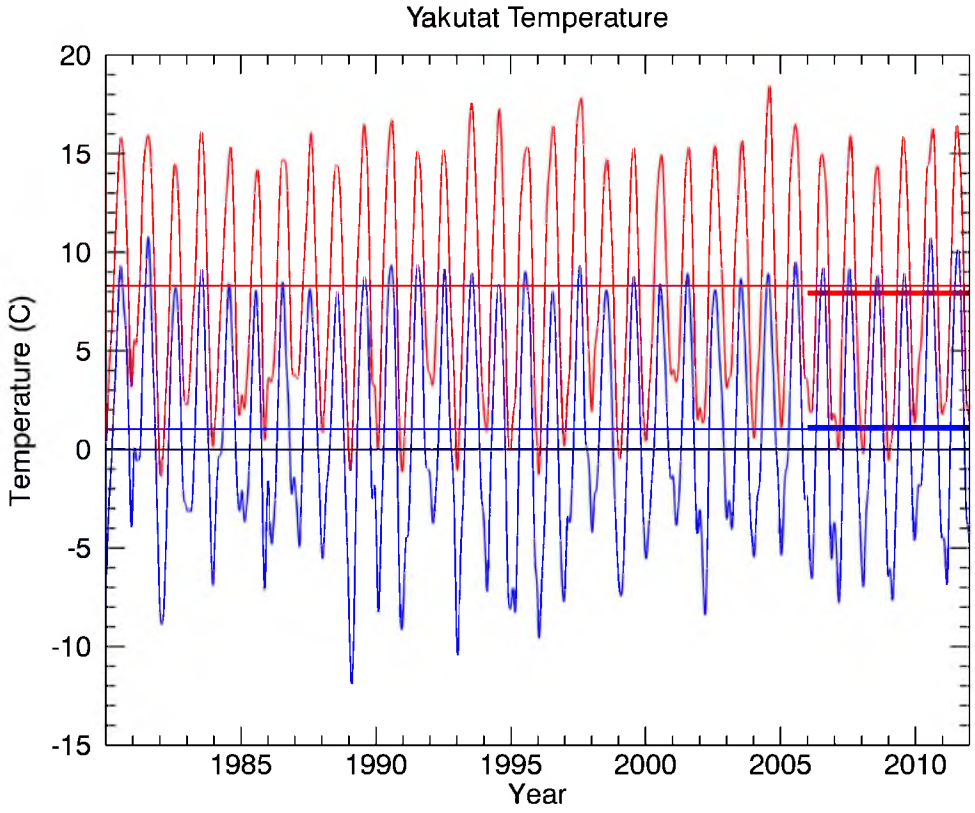


Figure 3.3. Daily minimum (blue) and maximum temperature (red) from Yakutat Station with a 1-month Gaussian smooth applied. 32-year climatic means (1980-2012) shown as thin horizontal lines. Thick horizontal lines show temperature means during the period of study. Z-scores (means and standard deviation derived from 1980-2012 data) of cumulative positive degree days for each year are shown as green circles.

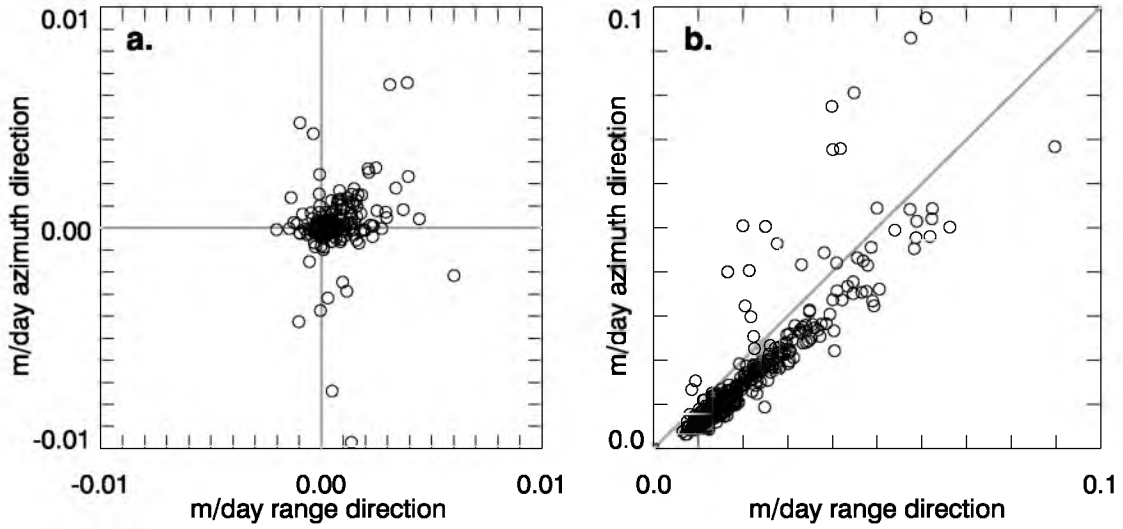


Figure 3.4. Estimated uncertainty in range (x) and azimuth (y) directions for each of 315 image pairs used. Image wide average bias vector (a) and MADn (robust equivalent to standard deviation) (b) of stable ground offsets.

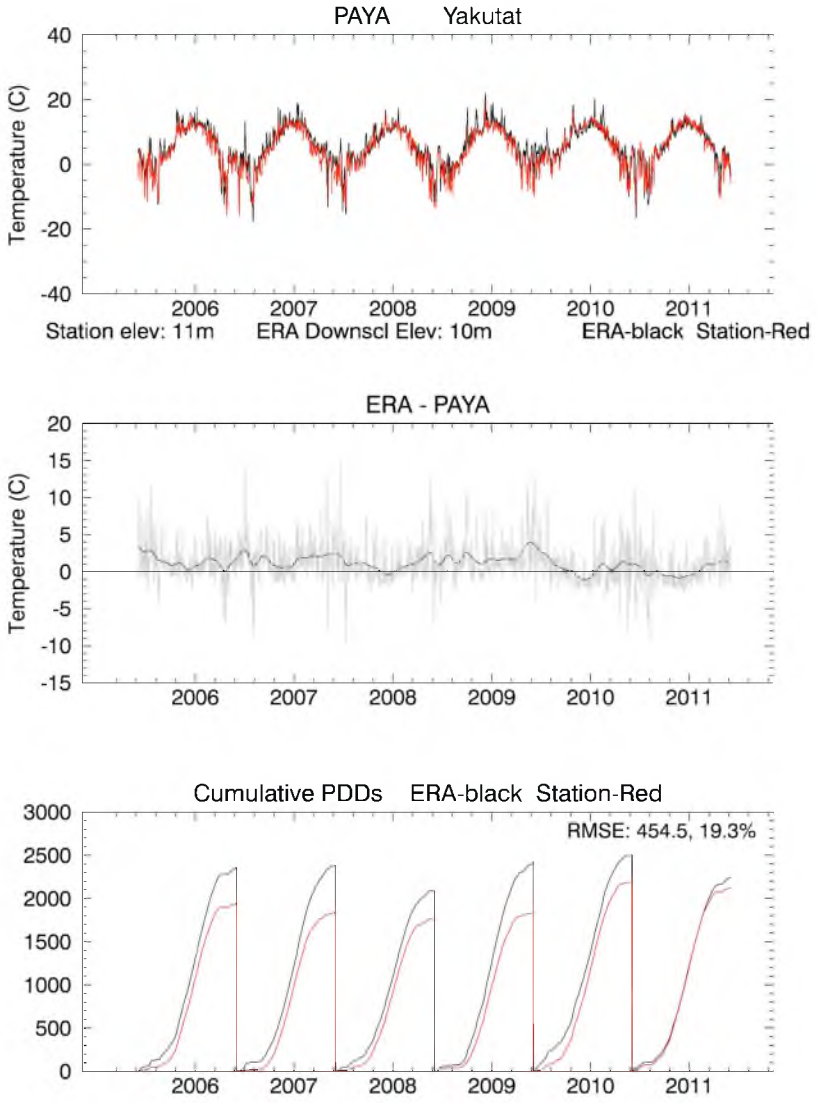


Figure 3.5. Comparison of PDD model with in situ observations from meteorological station data at PAYA (Fig. 3.1). Displayed are a timeseries of downscaled ERA-Interim temperature and observed temperature (top), the difference between ERA and observed temperatures (middle, grey) with a 15-day Gaussian smooth (middle, black), and cumulative PDDs from downscaled ERA-Interim and met station temperatures. Root mean squared error for PDD estimate is derived from all years.

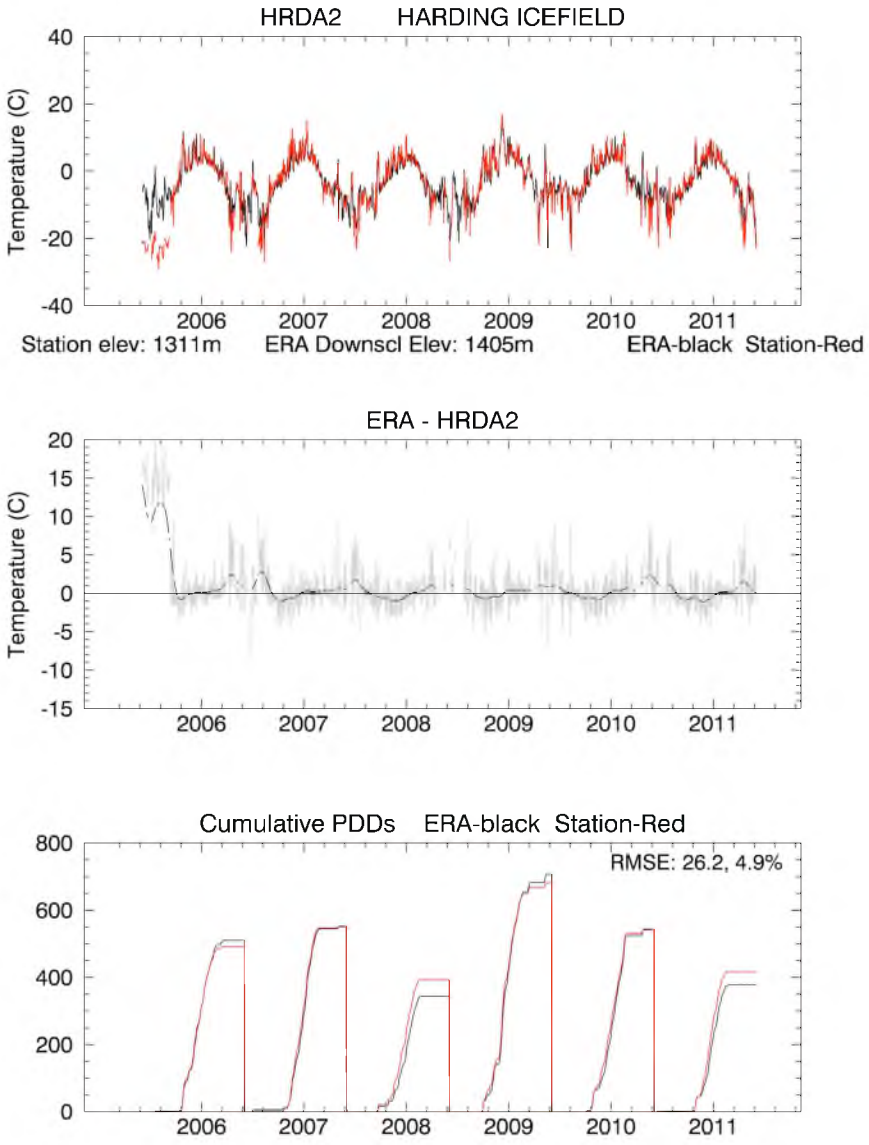


Figure 3.6. Comparison of PDD model with in situ observations from meteorological station data at HDRA2 (Fig. 3.1). Displayed are a timeseries of downscaled ERA-Interim temperature and observed temperature (top), the difference between ERA and observed temperatures (middle, grey) with a 15-day Gaussian smooth (middle, black), and cumulative PDDs from downscaled ERA-Interim and met station temperatures. Root mean squared error for PDD estimate is derived from all years.

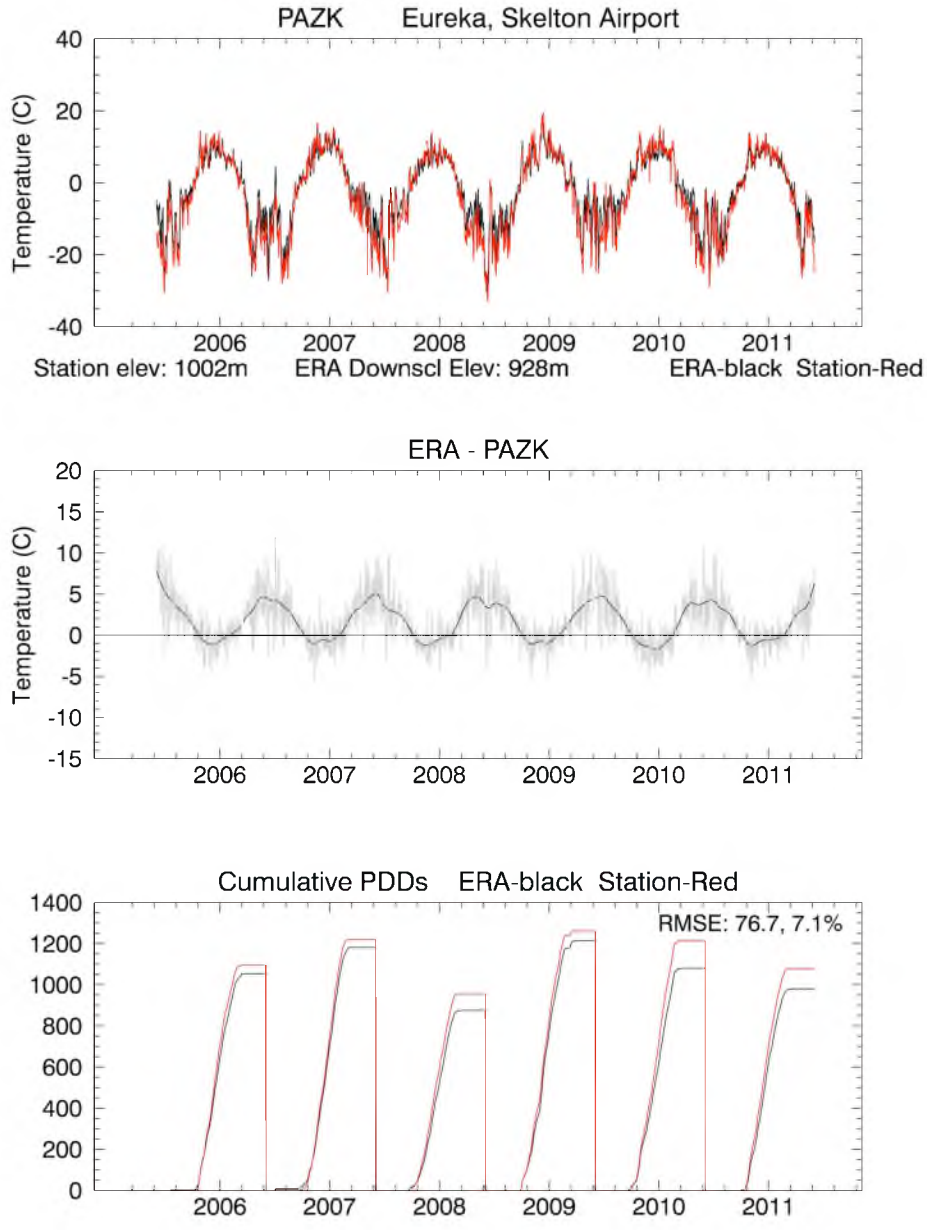


Figure 3.7. Comparison of PDD model with in situ observations from meteorological station data at PAZK (Fig. 3.1). Displayed are a timeseries of downscaled ERA-Interim temperature and observed temperature (top), the difference between ERA and observed temperatures (middle, grey) with a 15-day Gaussian smooth (middle, black), and cumulative PDDs from downscaled ERA-Interim and met station temperatures. Root mean squared error for PDD estimate is derived from all years.

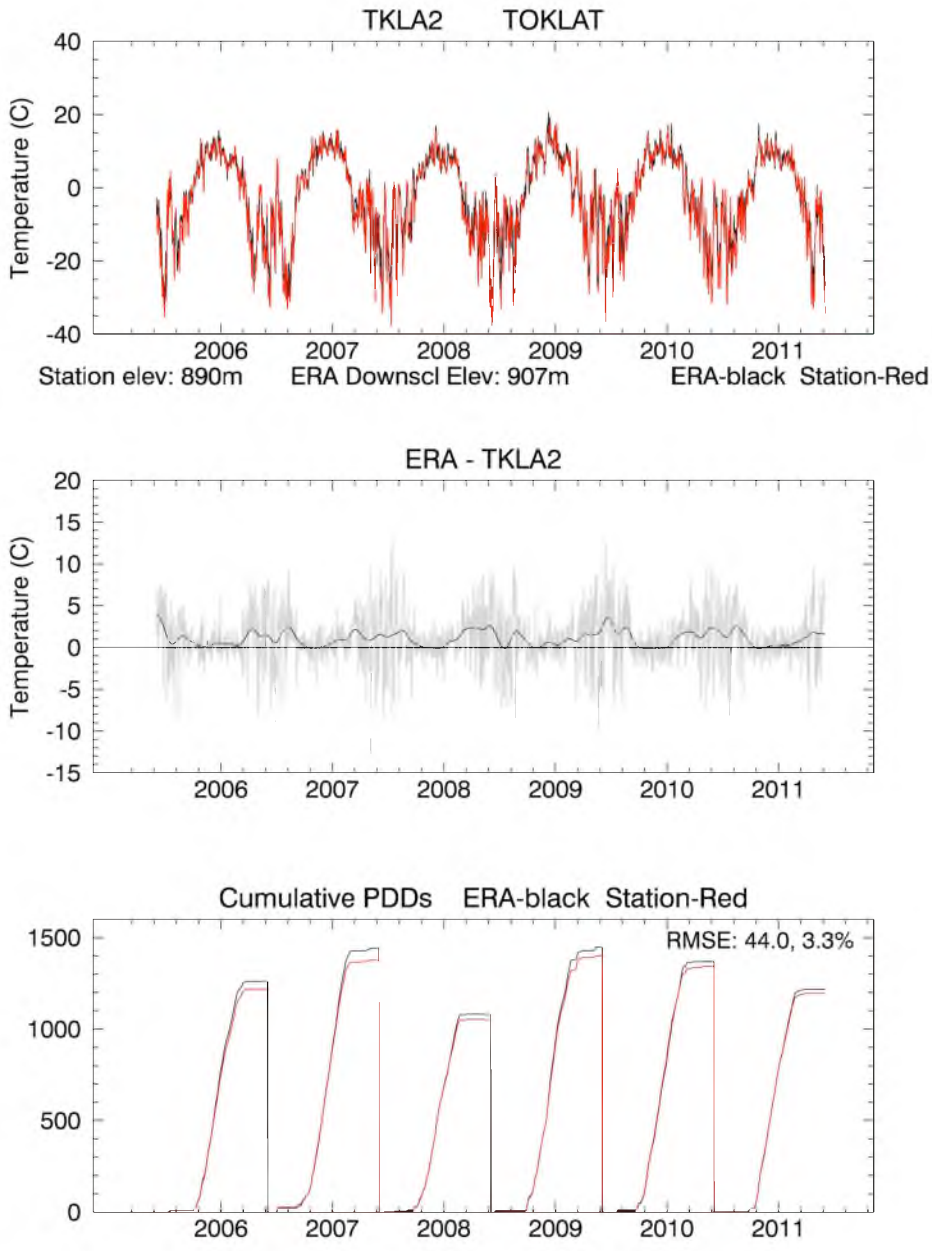


Figure 3.8. Comparison of PDD model with in situ observations from meteorological station data at TKLA2 (Fig. 3.1). Displayed are a timeseries of downscaled ERA-Interim temperature and observed temperature (top), the difference between ERA and observed temperatures (middle, grey) with a 15-day Gaussian smooth (middle, black), and cumulative PDDs from downscaled ERA-Interim and met station temperatures. Root mean squared error for PDD estimate is derived from all years.

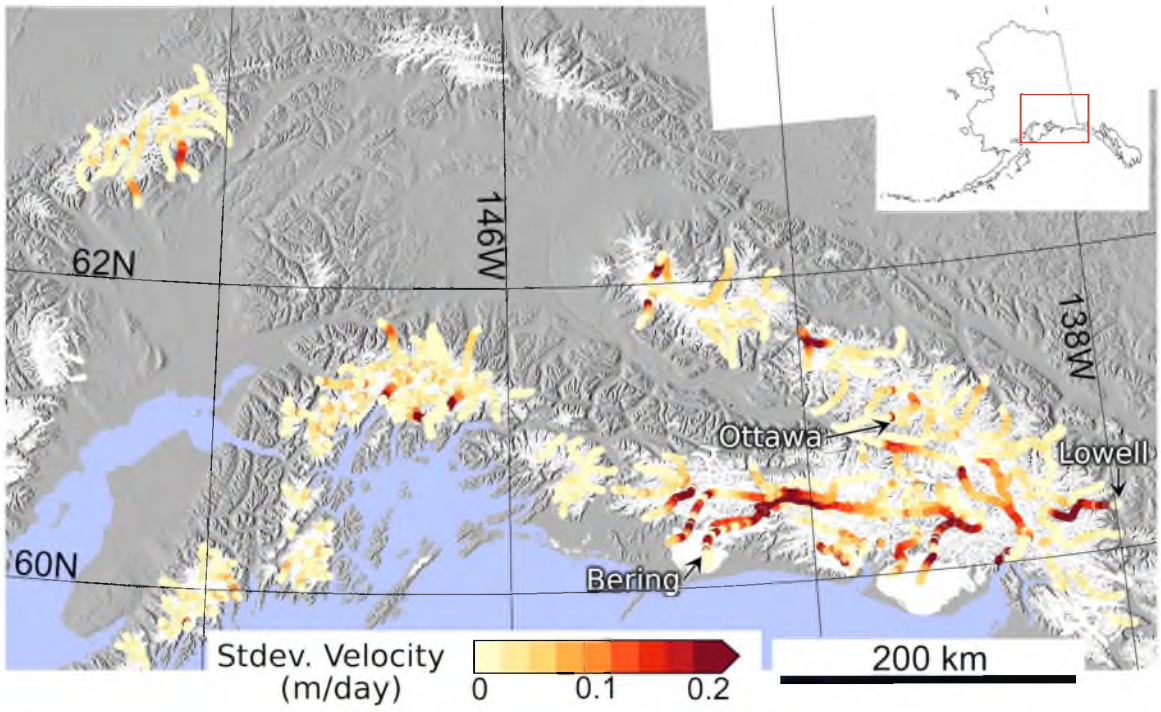


Figure 3.9. The standard deviation of velocity from all available winter data. Glaciers with known surges are labeled.

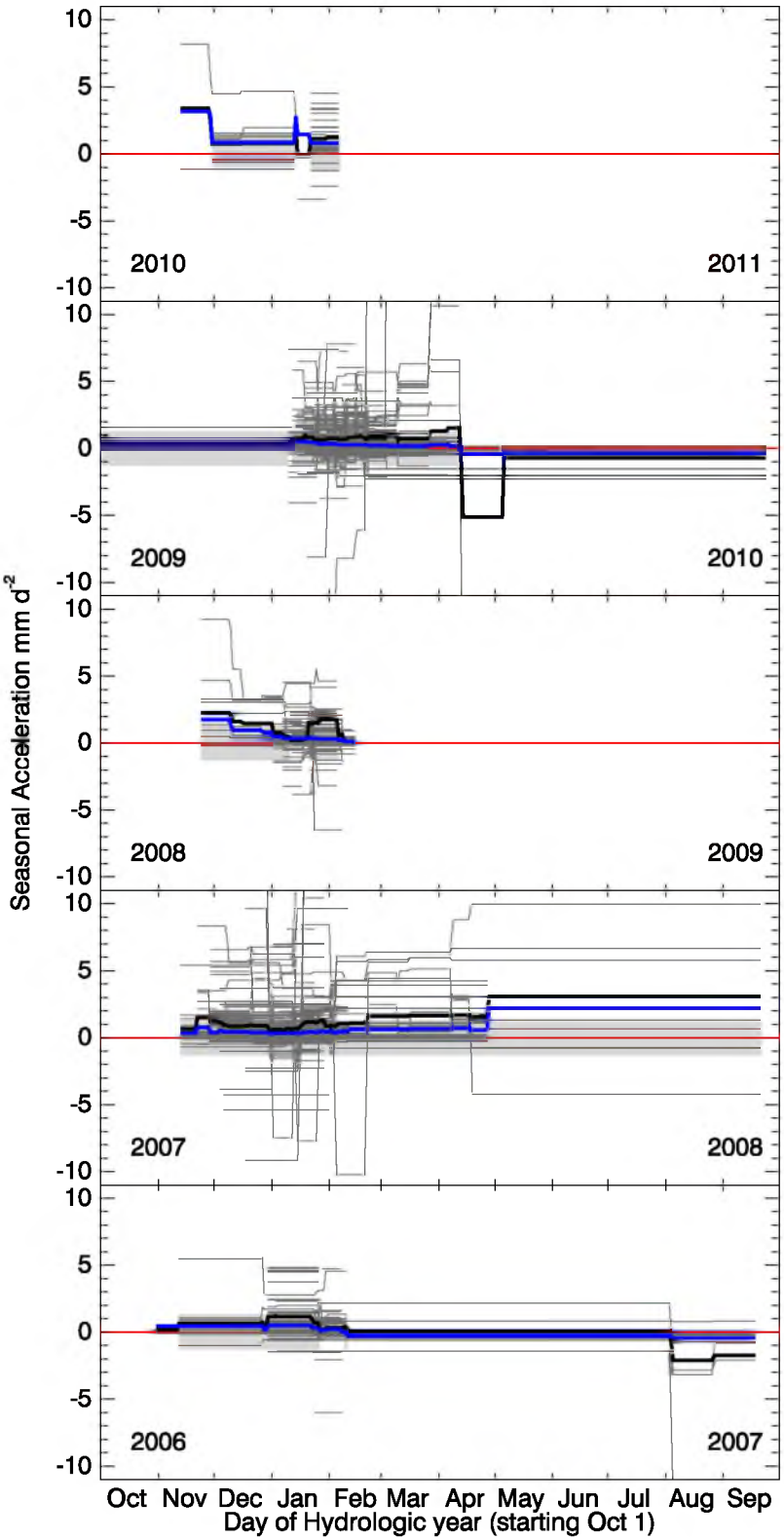


Figure 3.10. Rate of change in velocity between observations for hydrologic years. Grey lines represent along-profile mean rates of acceleration on individual glaciers. The mean (black) and median (blue) rate of acceleration for all glaciers is overlaid.

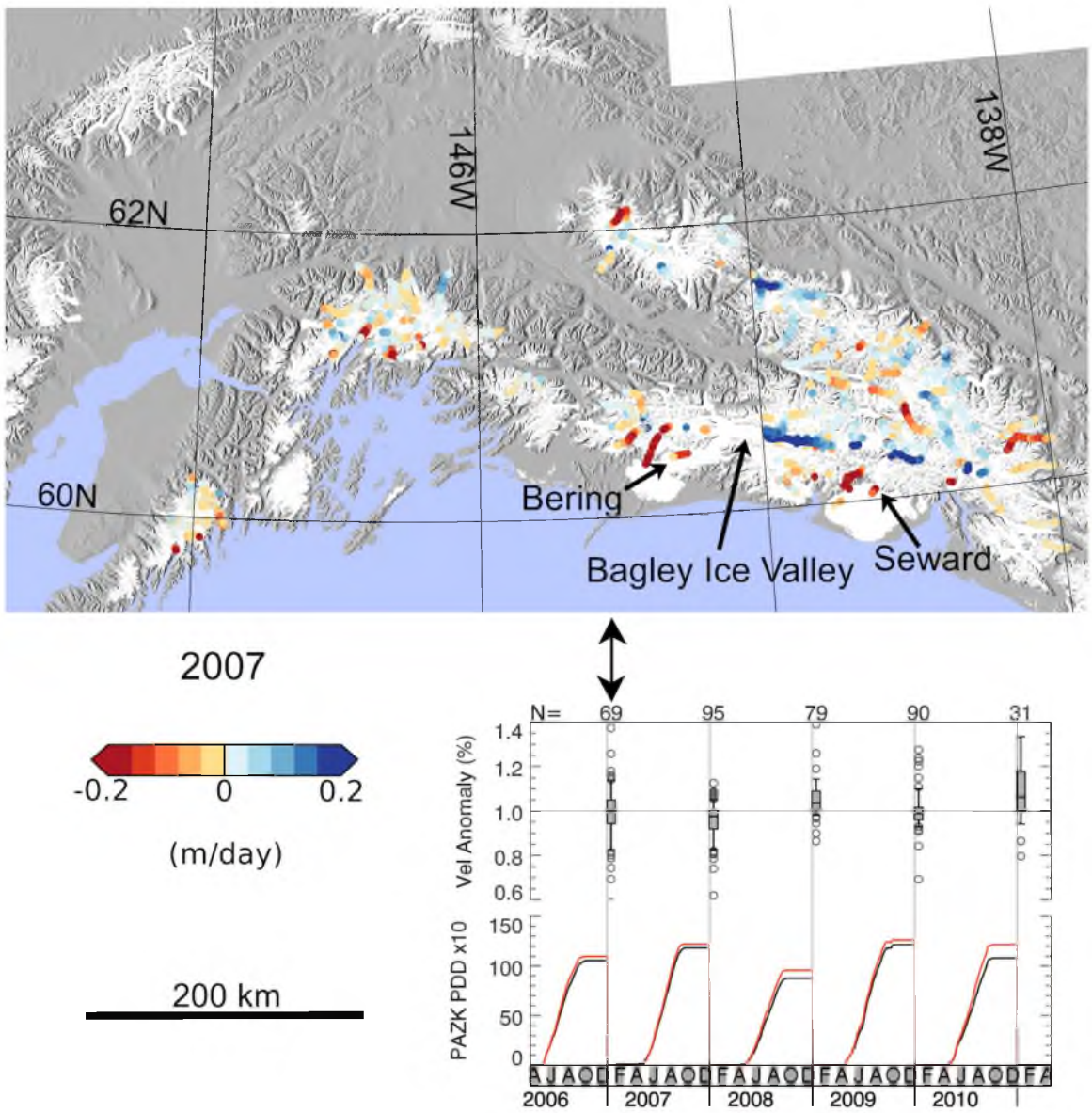


Figure 3.11. Velocity anomaly map for the 2007 hydrologic year (2006/07 winter) December - March. Blue/red indicates anomalously fast/slow moving ice. Plot on lower right and connecting arrow provides a temporal reference for the 2007 year within the period of study. Plot shows the distribution of January velocity anomalies (as a % for clarity) for all years and cumulative PDDs (red/black represents station/modeled PDDs) at PAZK on a consistent timescale.

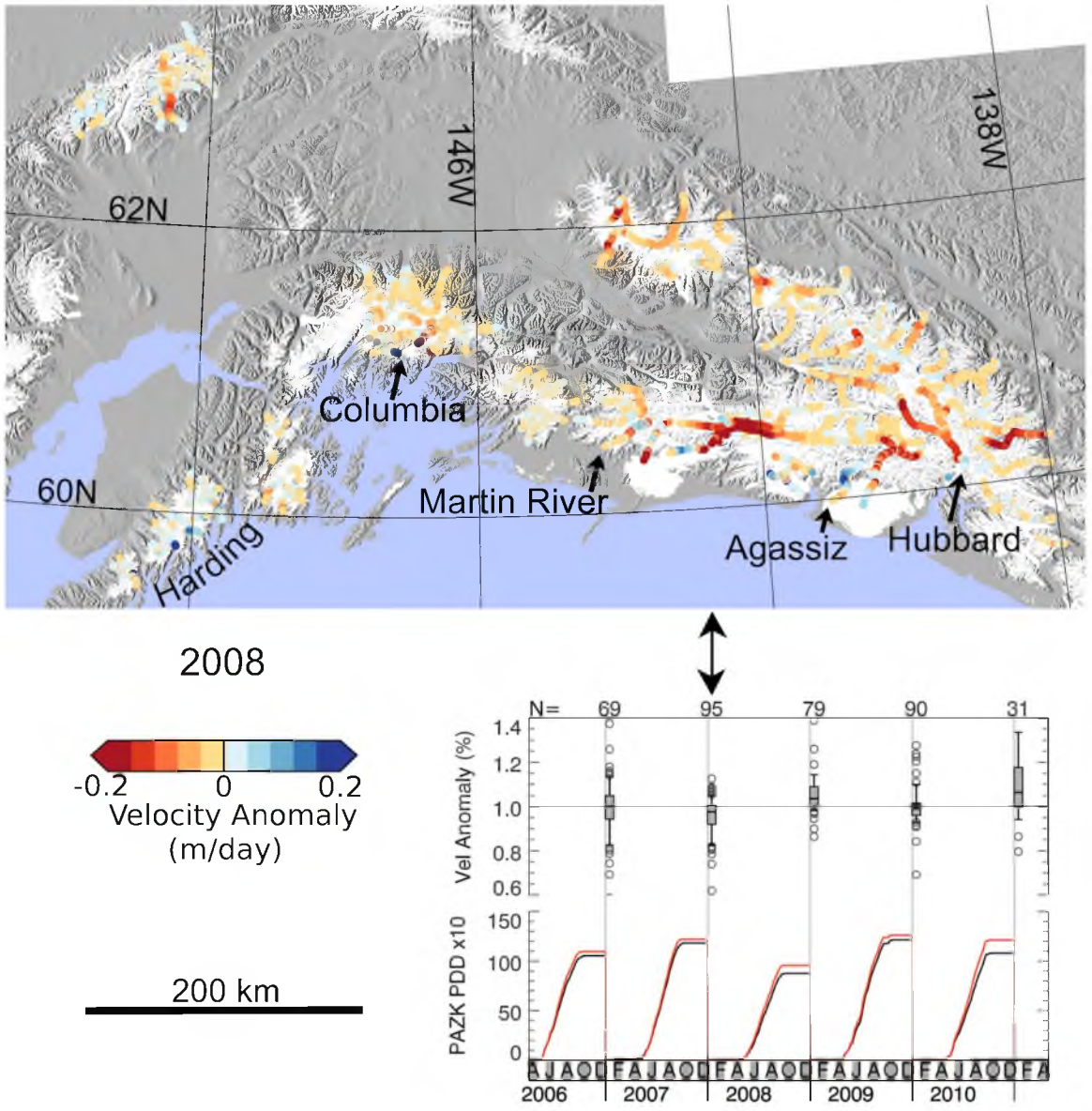


Figure 3.12. Velocity anomaly map for the 2008 hydrologic year (2007/08 winter) December - March. Blue/red indicates anomalously fast/slow moving ice. Plot on lower right and connecting arrow provides a temporal reference for the 2007 year within the period of study. Plot shows the distribution of January velocity anomalies (as a % for clarity) for all years and cumulative PDDs (red/black represents station/modeled PDDs) at PAZK on a consistent timescale.

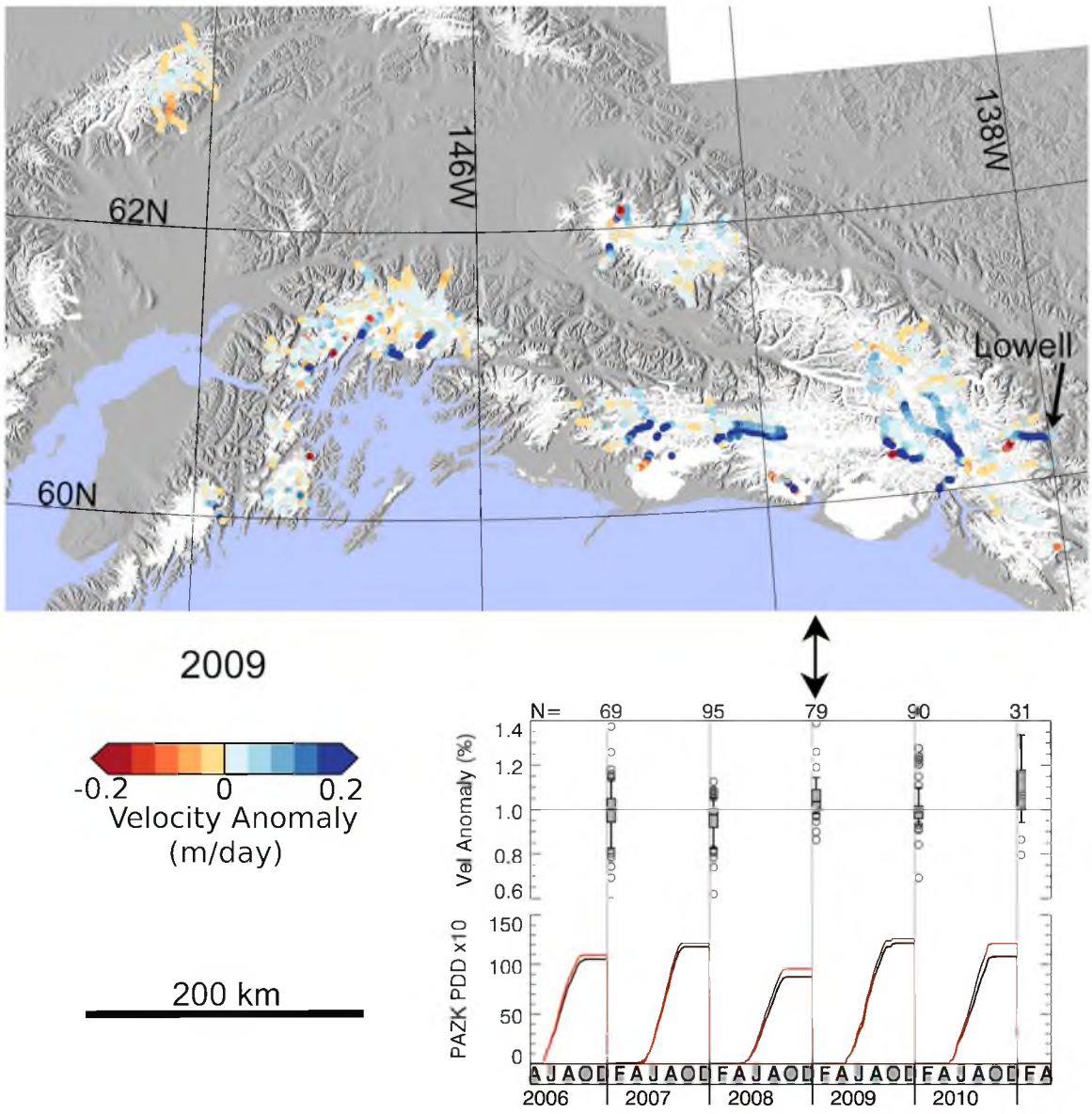


Figure 3.13. Velocity anomaly map for the 2009 hydrologic year (2008/09 winter) December - March. Blue/red indicates anomalously fast/slow moving ice. Plot on lower right and connecting arrow provides a temporal reference for the 2007 year within the period of study. Plot shows the distribution of January velocity anomalies (as a % for clarity) for all years and cumulative PDDs (red/black represents station/modeled PDDs) at PAZK on a consistent timescale.

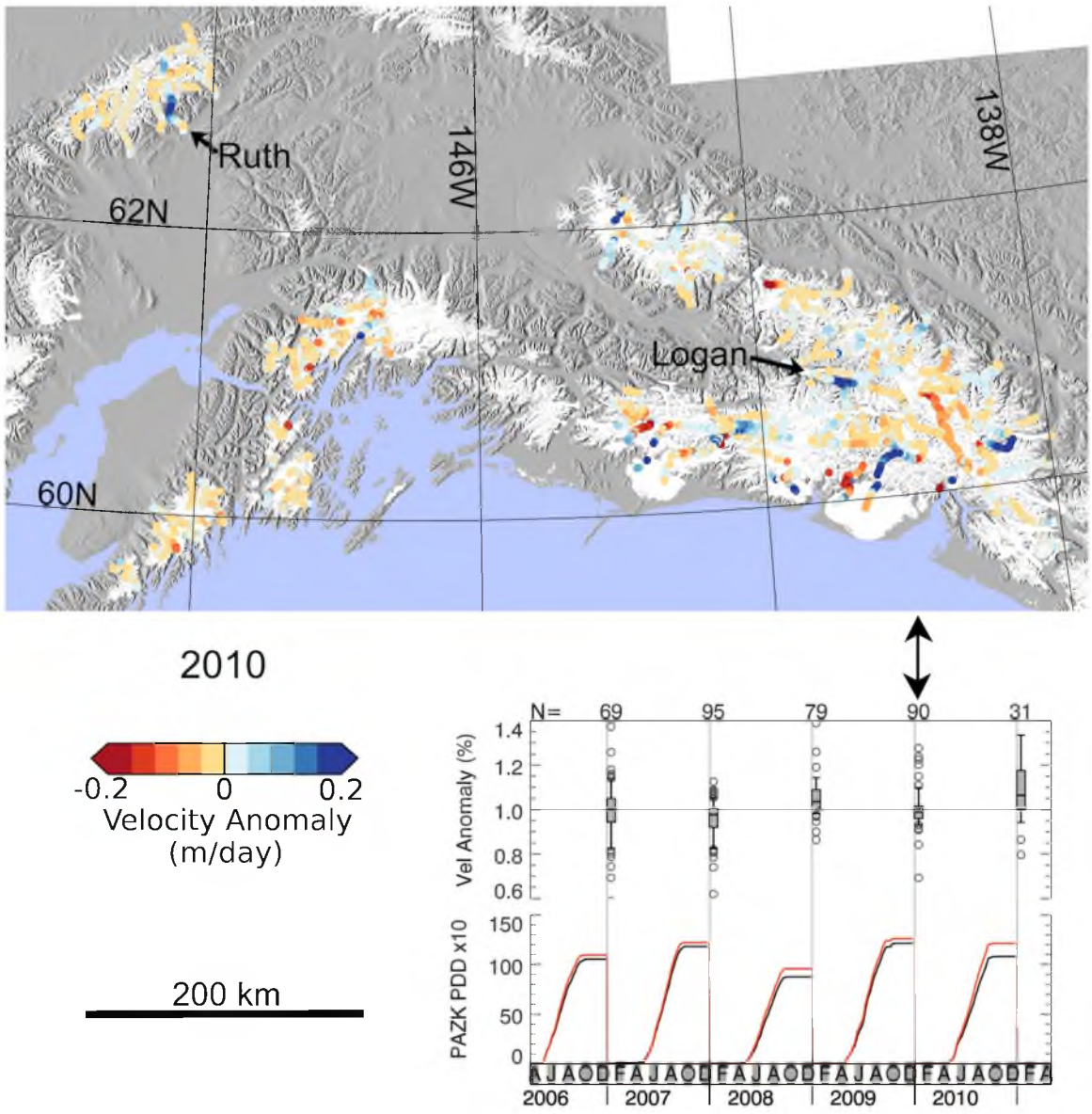


Figure 3.14. Velocity anomaly map for the 2010 hydrologic year (2009/10 winter) December - March. Blue/red indicates anomalously fast/slow moving ice. Plot on lower right and connecting arrow provides a temporal reference for the 2007 year within the period of study. Plot shows the distribution of January velocity anomalies (as a % for clarity) for all years and cumulative PDDs (red/black represents station/modeled PDDs) at PAZK on a consistent timescale.

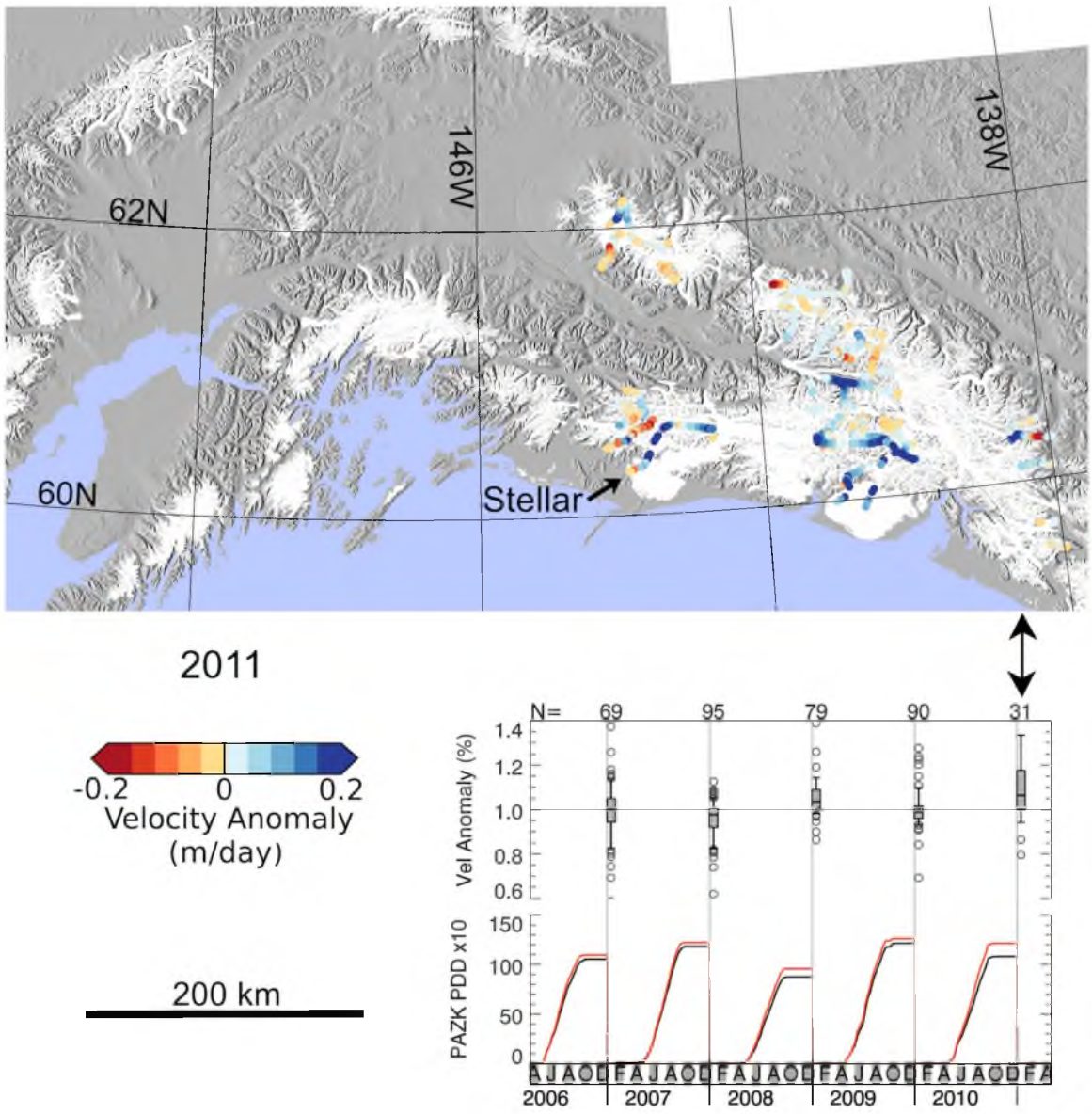


Figure 3.15. Velocity anomaly map for the 2011 hydrologic year (200/11 winter) December - March. Blue/red indicates anomalously fast/slow moving ice. Plot on lower right and connecting arrow provides a temporal reference for the 2007 year within the period of study. Plot shows the distribution of January velocity anomalies (as a % for clarity) for all years and cumulative PDDs (red/black represents station/modeled PDDs) at PAZK on a consistent timescale.

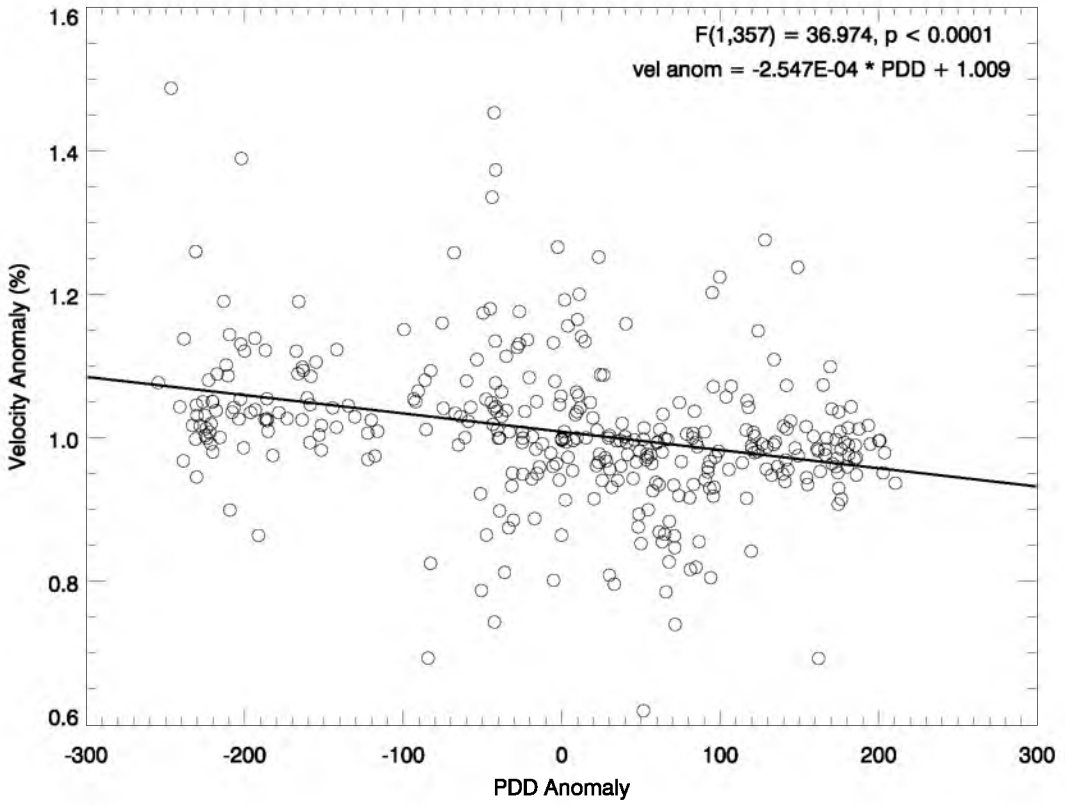


Figure 3.16. Scatterplot and regression of mean velocity anomalies and mean cumulative PDD anomalies for each glacier.

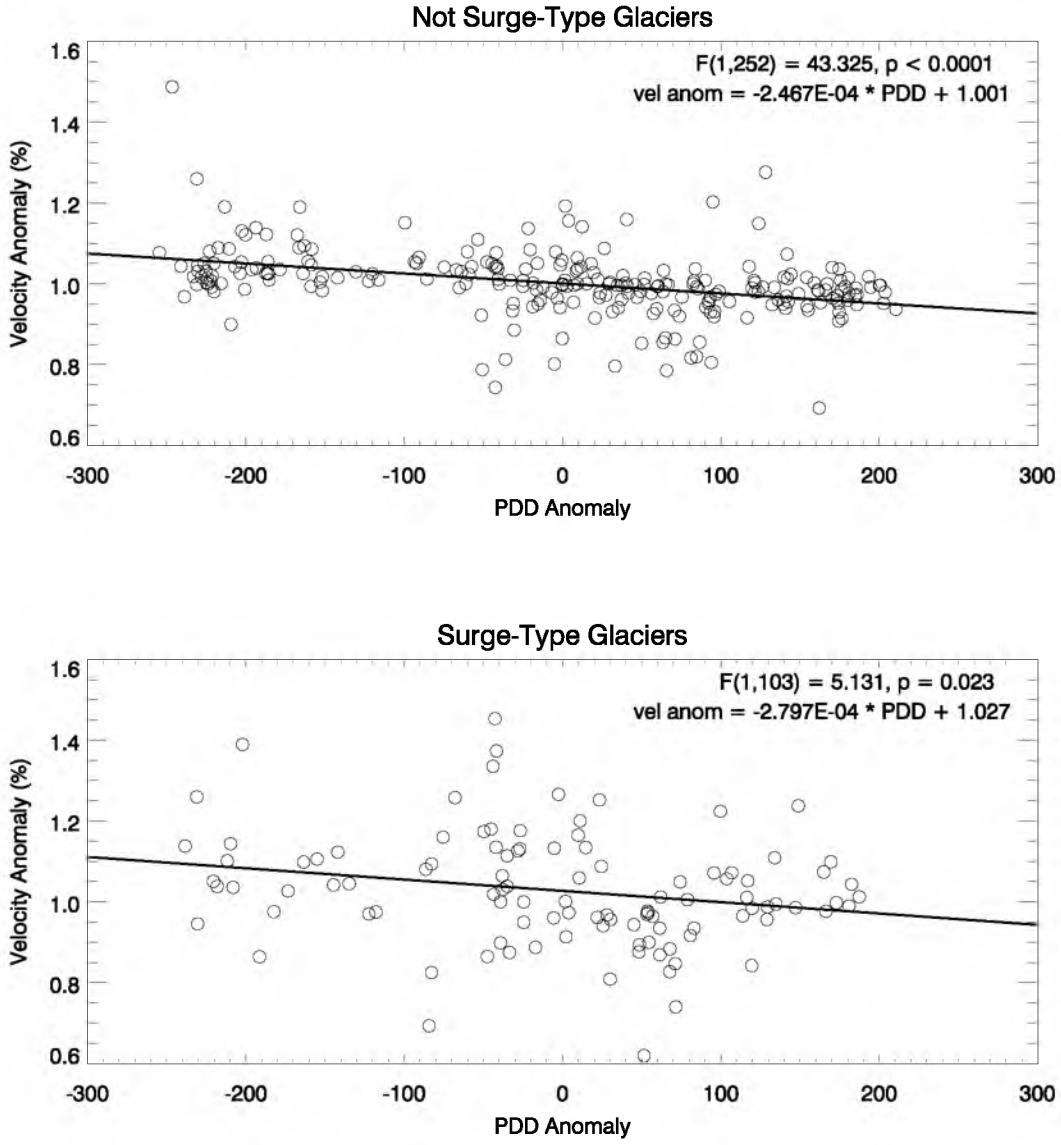


Figure 3.17. Scatterplots and regressions of mean velocity anomalies and mean cumulative PDD anomalies for each glacier. Panels separate data into surge type and not surge type as defined by (A. Post 1969)

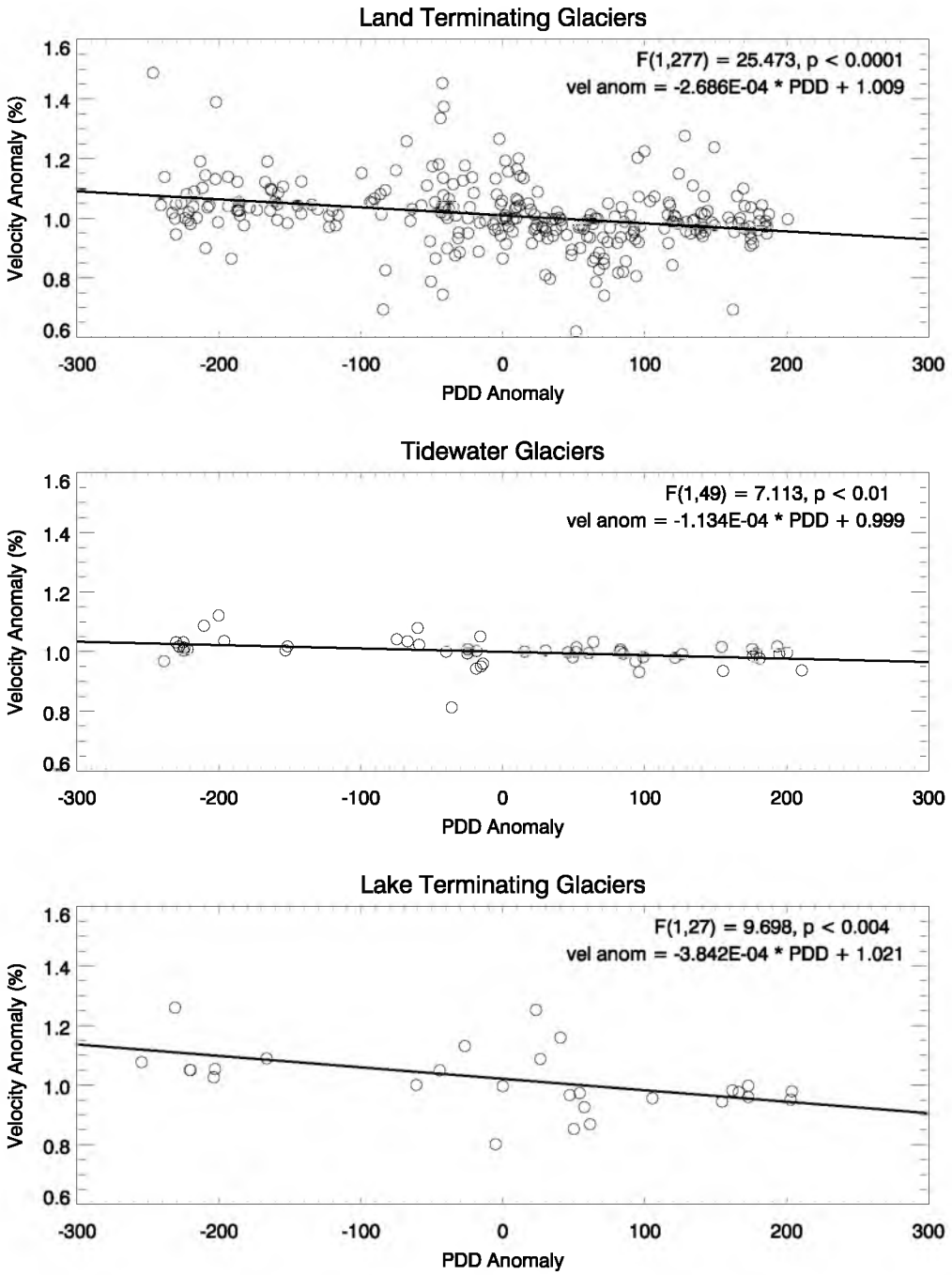


Figure 3.18. Scatterplots and regressions of mean velocity anomalies and mean cumulative PDD anomalies for each glacier. Panels separate glaciers into type of termination: land terminating, tidewater, and lake terminating.

## 3.8 References

Arendt, A., J. Walsh, and W. Harrison. 2009. Changes of glaciers and climate in Northwestern North America during the late twentieth century. *Journal of Climate* 22 (15):4117–4134.

Arendt, Anthony A., T. Bolch, J. G. Cogley, A. S. Gardner, J. O. Hagen, Regine Hock, G. Kaser, W. Tad Pfeffer, and and others. 2012. Randolph Glacier Inventory [v2.0]: A Dataset of Global Glacier Outlines.

Bartholomaus, T. C., R. S. Anderson, and S. P. Anderson. 2011. Growth and collapse of the distributed subglacial hydrologic system of Kennicott Glacier, Alaska, USA, and its effects on basal motion. *Journal of Glaciology* 57 (206):985–1002.

Bartholomaus, T. C., R.S. Anderson, and S.P. Anderson. 2008. Response of glacier basal motion to transient water storage. *Nature Geoscience* 1 (1):33–37.

Benn, D., J. Gulley, A. Luckman, A. Adamek, and P. S. Glowacki. 2009. Englacial drainage systems formed by hydrologically driven crevasse propagation. *Journal of Glaciology* 55 (191):513–523.

Bindschadler, Robert. 1983. The importance of pressurized subglacial water in separation and sliding at the glacier bed. *Annals of Glaciology* 29 (1983):349–349.

Boulton, G. S. 1979. Processes of glacier erosion on different substrata. *J. Glacio.* 23 (89):15–38.

Boulton, G. S., and A. S. Jones. 1979. Stability of temperate ice caps and ice sheets resting on deformable sediment. *J. Glacio.* 24 (90):29–43.

Burgess, E. W., R. R. Forster, and C. F. Larsen. 2013. Flow velocities of Alaska glaciers. *Nature Communications*.

Burgess, E. W., R. R. Forster, C. F. Larsen, and M. Braun. 2012. Surge dynamics on Bering Glacier, Alaska, in 2008–2011. *The Cryosphere* 6 (6):1251–1262.

Cohen, D., N. R. Iverson, T. S. Hooyer, U. H. Fischer, M. Jackson, and P. L. Moore. 2005. Debris-bed friction of hard-bedded glaciers. *Journal of Geophysical Research: Earth Surface* 110 (F2):n/a–n/a.

Cuffey, K. M., and W. S. B. Paterson. 2010. *The physics of glaciers, fourth edition* 4th ed. Academic Press.

Fatland, D. R., and C. S. Lingle. 2002. InSAR observations of the 1993-95 Bering Glacier (Alaska, U. S. A.) surge and a surge hypothesis. *Journal of Glaciology* 48:439–451.

Fudge, T. J., J. T. Harper, N. F. Humphrey, and W. Tad Pfeffer. 2005. Diurnal water-pressure fluctuations: timing and pattern of termination below Bench Glacier, Alaska, USA. *Annals of Glaciology* 40 (1):102–106.

Gray, A. L., K. E. Mattar, P. W. Vachon, R. Bindschadler, K. C. Jezek, R. Forster, and J. P. Crawford. 1998. InSAR results from the RADARSAT Antarctic mapping mission data: estimation of glacier motion using a simple registration procedure. In *International Geoscience and Remote Sensing Symposium (IGARSS)*, 1638–1640.

Hallet, B., L. Hunter, and J. Bogen. 1996. Rates of erosion and sediment evacuation by glaciers: A review of field data and their implications. *Global and Planetary Change* 12 (1-4):213–235.

Hallet, Bernard. 1979. A theoretical model of glacial abrasion. *Journal of Glaciology* 23 (89):39–50.

Harper, J. T., N. F. Humphrey, W. Tad Pfeffer, T. Fudge, and Shad O'Neel. 2005. Evolution of subglacial water pressure along a glacier's length. *Annals of Glaciology* 40 (1):31–36.

Heid, T., and A. Kääb. 2011. Worldwide widespread decadal-scale decrease of glacier speed revealed using repeat optical satellite images. *The Cryosphere Discussions* 5 (5):3025–3051.

Heinrichs, T. A., L. R. Mayo, K. A. Echelmeyer, and W. D. Harrison. 1996. Quiescent-phase evolution of a surge-type glacier: Black Rapids Glacier, Alaska, U.S.A. *Journal of Glaciology* 42:110–122.

Hock, Regine. 2003. Temperature index melt modelling in mountain areas. *Journal of Hydrology* 282 (1–4):104–115.

Horel, J., M. Splitt, L. Dunn, J. Pechmann, B. White, C. Ciliberti, S. Lazarus, J. Slemmer, D. Zaff, and J. Burks. 2002. Mesowest: Cooperative Mesonets in the Western United States. *Bulletin of the American Meteorological Society* 83 (2):211–225.

Iken, A., and R. Bindschadler. 1986. Combined measurements of subglacial water pressure and surface velocity of Findelengletscher, Switzerland: Conclusions about drainage system and sliding mechanism. *Journal of Glaciology* (32):101–119.

Iken, A., and M. Truffer. 1997. The relationship between subglacial water pressure and velocity of Findelengletscher, Switzerland, during its advance and retreat. *Journal of Glaciology* 43 (144):328–338.

Iverson, Neal R., Denis Cohen, Thomas S. Hooyer, Urs H. Fischer, Miriam Jackson, Peter L. Moore, G. Lappegard, and J. Kohler. 2003. Effects of basal debris on glacier flow. *Science* 301 (5629):81–84.

Johannessen, O. M., K. Khvorostovsky, M. W. Miles, and L. P. Bobylev. 2005. Recent ice-sheet growth in the interior of Greenland. *Science* 310 (5750):1013–1016.

Joughin, I., S. B. Das, M. A. King, B. E. Smith, I. M. Howat, and T. Moon. 2008. Seasonal speedup along the western flank of the Greenland Ice Sheet. *Science* 320 (5877):781–783.

Kamb, B., C. F. Raymond, W. D. Harrison, H. Engelhardt, K. A. Echelmeyer, N. Humphrey, M. M. Brugman, and T. Pfeffer. 1985. Glacier surge mechanism: 1982-1983 surge of Variegated Glacier, Alaska. *Science* 227 (4686):469–479.

Kamb, Barclay. 1987. Glacier surge mechanism based on linked cavity configuration of the basal water conduit system. *Journal of Geophysical Research* 92 (B9):9083–9100.

Krimmel, R. M. 2001. *Photogrammetric data set, 1957-2000, and bathymetric measurements for Columbia Glacier, Alaska*. Tacoma, Wash.: U.S. Geological Survey ;

Larsen, Christopher F., R. J. Motyka, Anthony A. Arendt, Keith A. Echelmeyer, and P. E. Geissler. 2007. Glacier changes in southeast Alaska and northwest British Columbia and contribution to sea level rise.

Lliboutry, L. 1968. General theory of subglacial cavitation and sliding of temperate glaciers. *Journal of Glaciology* 7 (49):21–58.

Luthcke, S. B., A.A. Arendt, D. D. Rowlands, J. J. McCarthy, and C.F. Larsen. 2008. Recent glacier mass changes in the Gulf of Alaska region from GRACE mascon solutions. *Journal of Glaciology* 54 (188):767–777.

Meier, M. F., M. B. Dyurgerov, U. K. Rick, Shad O'Neel, W. Tad Pfeffer, Robert S. Anderson, Suzanne P. Anderson, and A. F. Glazovsky. 2007. Glaciers Dominate Eustatic Sea-Level Rise in the 21st Century. *Science* 317 (5841):1064–1067.

METI and NASA. 2011. ASTER GDEM 2.0.

Michel, R., and E. Rignot. 1999. Flow of Glaciar Moreno, Argentina, from repeat-pass Shuttle Imaging Radar images: Comparison of the phase correlation method with radar interferometry. *Journal of Glaciology* 45 (149):93–100.

Motyka R.J., O'Neel S., Connor C.L., and Echelmeyer K.A. 2003. Twentieth century thinning of Mendenhall Glacier, Alaska, and its relationship to climate, lake calving, and glacier run-off. *Global and Planetary Change* 35 (1):93–112.

O'Neel, S., W.T. Pfeffer, R. Krimmel, and M. Meier. 2005. Evolving force balance at Columbia Glacier, Alaska, during its rapid retreat. *Journal of Geophysical Research F: Earth Surface* 110 (3).

Parizek, B. R., and R. B. Alley. 2004. Implications of increased Greenland surface melt under global-warming scenarios: ice-sheet simulations. *Quaternary Science Reviews* 23 (9-10):1013–1027.

Pelto, M. S., S. R. McGee, G. W. Adema, M. J. Beedle, M. M. Miller, K. F. Sprenke, and M. Lang. 2008. The equilibrium flow and mass balance of the Taku Glacier, Alaska 1950-2006. *The Cryosphere Discussions* 2 (3):275–298.

Porter, S. C. 1989. Late Holocene fluctuations of the fiord glacier system in Icy Bay, Alaska, USA. *Arctic & Alpine Research* 21 (4):364–379.

Post, A. 1969. Distribution of surging glaciers in western North America. *J. Glacio.* 5 (53):229–240.

Post, A. S. 1960. The exceptional advances of the Muldrow, Black Rapids, and Susitna glaciers. *Journal of Geophysical Research* 65 (11):3703–3712.

Radić, V., and R. Hock. 2011. Regionally differentiated contribution of mountain glaciers and ice caps to future sea-level rise. *Nature Geoscience* 4 (2):91–94.

Raymond, C. F. 1987. How do glaciers surge? A review. *Journal of Geophysical Research* 92 (B9):9121–9134.

Raymond, C. F., and W. D. Harrison. 1988. Evolution of Variegated Glacier, Alaska, U.S.A prior to its surge. *Journal of Glaciology* 34 (117):154–169.

Röthlisberger, H. 1972. Water pressure in intra- and subglacial channels. *Journal of Glaciology* 11:177–203.

Schoof, C. 2010. Ice-sheet acceleration driven by melt supply variability. *Nature* 468 (7325):803–806.

Sundal, A. V., A. Shepherd, P. Nienow, E. Hanna, S. Palmer, and P. Huybrechts. 2011. Melt-induced speed-up of Greenland ice sheet offset by efficient subglacial drainage. *Nature* 469 (7331):521–524.

Truffer, Martin, W. D. Harrison, and R. S. March. 2005. Correspondence: Record negative glacier balances and low velocities during the 2004 heat wave in Alaska, USA: Implications for the interpretation of observations by Zwally and others in Greenland. *Journal of Glaciology* 51:663–664.

Van de Wal, R. S. W., W. Boot, M. R. Van den Broeke, C. J. P. P. Smeets, C. H. Reijmer, J. J. A. Donker, and J. Oerlemans. 2008. Large and rapid melt-induced velocity changes in the ablation zone of the Greenland Ice Sheet. *Science* 321 (5885):111–113.

Weertman, J. 1957. On the sliding of glaciers. *Journal of Glaciology* 3:33–38.

Zwally, H. J., W. Abdalati, T. Herring, K. Larson, J. Saba, and K. Steffen. 2002. Surface melt-induced acceleration of Greenland ice-sheet flow. *Science* 297 (5579):218–222.

# CONCLUSION

The results presented represent the first regional examination of mountain glacier flow speeds in Alaska, covering 28,022 $km^2$ of ice. The velocity maps provide baseline wintertime flow speeds prior to spring speedup on almost every major glacier system in the Wrangell/St. Elias, Chugach, Kenai Peninsula, Alaska Range and Tordrillo Ranges. In addition, these data have revealed much about the importance of ice dynamics for current and future mass loss in Alaska and elsewhere. These findings include:

1) Throughout our study region, wintertime glacier velocities are highly variable but the amount of variability is spatially dependent; thus geology likely impacts the magnitude of interannual winter variability.
2) Use of the term, "wintertime background velocity," we find to be of questionable validity.
3) The majority of the regionwide downstream flux is confined to a few high-elevation, coastal glaciers with anomalously high balance velocities. These rapid-flow glaciers systems may operate differently than other glaciers as they are able to maintain higher flow speeds and higher driving stresses without losing mass. Understanding these unique dynamics is critical for future projections of ice dynamic mass loss in Alaska.

4) Currently, south central Alaska looses ~16 $km^3$ $a^{-1}$ to tidewater calving. This rate is equivalent to 76% of the regional net mass lost annually. Consequently, ice dynamic mass loss must be considered in models aimed at projecting mountain glacier mass loss.

5) On regional scales, wintertime velocity is inversely correlated to cumulative summertime melt from the previous summer. This likely occurs because greater meltwater production results in a more extensive conduit system that facilitates evacuation of subglacial water in the fall and thus allows for less bed separation in winter. This mechanism may well exist outside of Alaska and thus could have significant implications with regards to long-term ice dynamic changes in a warming climate.

6) Cumulative summertime melt also exerts a secondary control on surge initiation and evolution. This implies that given appropriate geometry, anomalously cold/warm summers could help to instigate/delay surge onset.

7) With respect to the surge of Bering Glacier, areas capable of rapid acceleration are confined to areas of relatively high driving stresses. But as the driving stress evolves during each stage of the surge, the basal drag does not dynamically adjust to the evolving driving stress. Rather, the rapid flow must shut down and reset for another stage before the dynamic balance line can move downstream.

These conclusions have several implications for constraining sea level rise projections. Globally, changes in calving fluxes from tidewater dynamics potentially have the capacity to overwhelm all other new-water sea level rise contributors, including surging, a wintertime velocity/summertime temperature feedback, and even surface mass

balance losses. So ascertaining the range of potential rates of mass loss from calving is of the utmost importance. Our calving estimates provide a baseline/lowball rate of calving mass loss in Alaska and are thus a critical first step to this goal. In addition, future work will also help to estimate the maximum possible contribution to SLR from ice dynamics in Alaska. In mountain glacier environments, the maximum potential calving mass loss is far less than the total ice volume and could be lost relatively rapidly compared to the ice sheets. Thus maximum potential calving losses have weight in century long projections. Globally, these results show that mountain glacier mass loss projections cannot ignore calving loss and thus we need to reconsider our uncertainties as we begin to constrain potential dynamic mass loss.

The feedback between wintertime flow velocity and summertime melt may have an impact on sea level rise over the coming century but much more understanding is needed to ascertain whether this is the case. The precise mechanism causing this relationship needs to be understood and the global spatial extent of the dynamic must be understood as well. How much mass could be preserved through this mechanism is not yet known; it is likely small, though perhaps not insignificantly so.

Another obvious important result presented is the velocity dataset itself and the many opportunities it provides for future work. The velocity map can be used along with continuity modeling to derive bed topography (Mcnabb et al. 2012), thus providing robust estimates of total ice volume, volumetric flux, and basal sliding velocity throughout Alaska. These advancements will help in several ways. First, we will be able to estimate the total potential SLR contribution and maximum calving potential SLR contribution from Alaska. We will also be able to derive robust volumetric flux estimates

that will lead to better estimates of tidewater mass losses than presented in Chapter 1. We will also be able to estimate basal sliding velocity (our observations are of surface velocity) which, will help understanding of ice dynamics and improve understanding of glacier erosion rates and tectonic uplift in Alaska (Headley, Roe, and Hallet 2012; Ward, Anderson, and Haeussler 2012; Bruhn et al. 2012). Bed topography will also enable full three-dimensional flow modeling of glaciers that could assist in evaluating the stability of tidewater systems in Alaska over the long-term.

Perhaps the most important implication of this work is a highlighted need for further study of mountain glacier tidewater/lake calving mass loss. It is well understood that ice dynamics and calving processes are leading to large uncertainties in ice sheet SLR contributions. While the same dynamics occur in mountain environments, much less attention has been given to dynamics because the glaciers are small compared to the ice sheets. But this work highlights that the ice dynamic uncertainties – which, are of critical focus on the ice sheets – are of comparable importance in mountain glacier environments during the coming century.

## References

Bruhn, R. L., J. Sauber, M. M. Cotton, T. L. Pavlis, Evan Burgess, N. Ruppert, and Richard R. Forster. 2012. Plate margin deformation and active tectonics along the northern edge of the Yakutat Terrane in the Saint Elias Orogen, Alaska, and Yukon, Canada. *Geosphere* 8 (6):1384–1407.

Headley, R. M., G. Roe, and B. Hallet. 2012. Glacier longitudinal profiles in regions of active uplift. *Earth and Planetary Science Letters* 317-318:354–362.

Mcnabb, R. W., R. Hock, S. O'Neel, L. A. Rasmussen, Y. Ahn, M. Braun, H. Conway, S. Herreid, I. Joughin, W.T. Pfeffer, B. E. Smith, and M. Truffer. 2012. Using surface velocities to calculate ice thickness and bed topography: a case study at Columbia Glacier, Alaska, USA. *Journal of Glaciology* 58 (212):1151–1164.

Ward, D. J., R. S. Anderson, and P. J. Haeussler. 2012. Scaling the Teflon Peaks: Rock type and the generation of extreme relief in the glaciated western Alaska Range. *Journal of Geophysical Research* 117 (F1).